Sub-seasonal physical dynamics of temperature, light, turbidity, and water motion in eelgrass (*Zostera marina*) beds on the Atlantic coast of Nova Scotia, Canada

Melisa C. Wong and Michael Dowd

Science Branch, Coastal Ecosystem Sciences Division
Maritimes Region, Fisheries and Oceans Canada
Bedford Institute of Oceanography
1 Challenger Drive
Dartmouth, NS B2Y 4A2

2021

Canadian Technical Report of
Fisheries and Aquatic Sciences 3447

Fisheries and Oceans Canada | Pêches et Océans Canada

Canada

Canadian Technical Report of Fisheries and Aquatic Sciences

Technical reports contain scientific and technical information that contributes to existing knowledge but which is not normally appropriate for primary literature. Technical reports are directed primarily toward a worldwide audience and have an international distribution. No restriction is placed on subject matter and the series reflects the broad interests and policies of Fisheries and Oceans Canada, namely, fisheries and aquatic sciences.

Technical reports may be cited as full publications. The correct citation appears above the abstract of each report. Each report is abstracted in the data base *Aquatic Sciences and Fisheries Abstracts*.

Technical reports are produced regionally but are numbered nationally. Requests for individual reports will be filled by the issuing establishment listed on the front cover and title page.

Numbers 1-456 in this series were issued as Technical Reports of the Fisheries Research Board of Canada. Numbers 457-714 were issued as Department of the Environment, Fisheries and Marine Service, Research and Development Directorate Technical Reports. Numbers 715-924 were issued as Department of Fisheries and Environment, Fisheries and Marine Service Technical Reports. The current series name was changed with report number 925.

Rapport technique canadien des sciences halieutiques et aquatiques

Les rapports techniques contiennent des renseignements scientifiques et techniques qui constituent une contribution aux connaissances actuelles, mais qui ne sont pas normalement appropriés pour la publication dans un journal scientifique. Les rapports techniques sont destinés essentiellement à un public international et ils sont distribués à cet échelon. II n'y a aucune restriction quant au sujet; de fait, la série reflète la vaste gamme des intérêts et des politiques de Pêches et Océans Canada, c'est-à-dire les sciences halieutiques et aquatiques.

Les rapports techniques peuvent être cités comme des publications à part entière. Le titre exact figure au-dessus du résumé de chaque rapport. Les rapports techniques sont résumés dans la base de données *Résumés des sciences aquatiques et halieutiques.*

Les rapports techniques sont produits à l'échelon régional, mais numérotés à l'échelon national. Les demandes de rapports seront satisfaites par l'établissement auteur dont le nom figure sur la couverture et la page du titre.

Les numéros 1 à 456 de cette série ont été publiés à titre de Rapports techniques de l'Office des recherches sur les pêcheries du Canada. Les numéros 457 à 714 sont parus à titre de Rapports techniques de la Direction générale de la recherche et du développement, Service des pêches et de la mer, ministère de l'Environnement. Les numéros 715 à 924 ont été publiés à titre de Rapports techniques du Service des pêches et de la mer, ministère des Pêches et de l'Environnement. Le nom actuel de la série a été établi lors de la parution du numéro 925.

Canadian Technical Report of
Fisheries and Aquatic Sciences 3447

2021

Sub-seasonal physical dynamics of temperature, light, turbidity, and water motion in eelgrass (*Zostera marina*) beds on the Atlantic coast of Nova Scotia, Canada

By

Melisa C. Wong and Michael Dowd[1]

Science Branch
Maritimes Region
Coastal Ecosystem Sciences Division
Fisheries and Oceans Canada
1 Challenger Drive
Dartmouth, NS B2Y 4A2

[1]Department of Mathematics and Statistics, Dalhousie University, Halifax, NS B3H 4R2

Cat. No. Fs97-6/3447E-PDF ISBN 978-0-660-40620-6 ISSN 1488-5379

Correct citation for this publication:

Wong, M.C., Dowd, M. 2021. Sub-seasonal physical dynamics of temperature, light, turbidity, and water motion in eelgrass (*Zostera marina*) beds on the Atlantic coast of Nova Scotia, Canada. Can. Tech. Rep. Fish. Aquat. Sci. 3447: v + 74 p.

TABLE OF CONTENTS

ABSTRACT

Wong, M.C., Dowd, M. 2021. Sub-seasonal physical dynamics of temperature, light, turbidity, and water motion in eelgrass (*Zostera marina*) beds on the Atlantic coast of Nova Scotia, Canada. Can. Tech. Rep. Fish. Aquat. Sci. 3447: v + 74 p.

Eelgrass growth and productivity are strongly influenced by the surrounding physical environment, particularly water temperature and light. Short-term physical processes (i.e., sub-seasonal processes), such as solar heating or sediment resuspension, are important drivers of eelgrass condition. Here, we characterize physical processes relevant for eelgrass across varying time scales. Time series of temperature, light, turbidity, and water current were obtained for six eelgrass beds in Nova Scotia. Various metrics, including mean seasonal and daily values, variability, and range were computed. Temperature data were further processed to isolate signals related to seasonal, meteorological, and tidal processes, and to identify thermal stress events. Our analyses showed that some eelgrass beds were located in shallow water, with muddy/silty sediments, low current speed, and low wave exposure. Sub-seasonal physical processes such as solar heating, tidal exchange, and wind events were important, resulting in thermal stress and light reduction. Other beds were located in deeper water, with sandy sediments, and moderate currents and wave exposure. Short-term processes were less evident, and water was cooler and less turbid. At all sites, temperature changes on meteorological time scales (48 hrs to 60 days) were coherent, suggesting the importance of coast-wide processes. Clear relationships among light attenuation, wind stress, and turbidity were not evident, but might emerge with improved wind data and sensor deployment. Our study suggests that eelgrass growth and productivity will differ according to the physical environment and the statistical character of sub-seasonal processes. Our results serve to strengthen conservation decisions related to eelgrass protection, and can be used to predict eelgrass response to future change.

RÉSUMÉ

Wong, M.C., Dowd, M. 2021. Sub-seasonal physical dynamics of temperature, light, turbidity, and water motion in eelgrass (*Zostera marina*) beds on the Atlantic coast of Nova Scotia, Canada. Can. Tech. Rep. Fish. Aquat. Sci. 3447: v + 74 p.

La croissance et la productivité de la zostère sont fortement influencées par le milieu physique environnant, en particulier par la température de l'eau et la lumière. Les processus physiques de courte durée (c.-à-d. les processus infrasaisonniers), comme le réchauffement solaire ou la remise en suspension des sédiments, sont des facteurs importants de l'état de la zostère. Ici, nous caractérisons les processus physiques pertinents pour la zostère à différentes échelles de temps. Des séries chronologiques de température, de lumière, de turbidité, et de courant d'eau ont été obtenues pour six herbiers de zostères en Nouvelle-Écosse. Divers paramètres, dont les valeurs moyennes saisonnières et quotidiennes, la variabilité et l'étendue, ont été calculées. Les données de température ont été traitées de manière à isoler les signaux liés aux processus saisonniers, météorologiques et de marée, ainsi qu'à identifierr les événements de contrainte thermique. Nos analyses ont montré que certains herbiers de zostère marine étaient situés dans des eaux peu profondes, avec des sédiments boueux/limoneux, une faible vitesse du courant et une faible exposition aux vagues. Les processus physiques infrasaisonniers tels que le réchauffement solaire, la distance d'échange de marée et les forts vents étaient importants, entraînant une contrainte thermique et une réduction de la lumière. D'autres herbiers se trouvent en eaux profondes, où l'on trouve des sédiments sableux, ainsi qu'un courant et une exposition aux vagues modérés. Les processus à court terme étaient moins évidents et l'eau était plus froide et moins turbide. Dans tous les sites, les changements de température sur des échelles de temps météorologiques (de 48 heures à 60 jours) étaient cohérents, ce qui suggère l'importance des processus à l'échelle de la côte. Des relations claires entre l'atténuation de la lumière, la force du vent et la turbidité n'étaient pas évidentes, mais pourraient émerger avec l'amélioration des données sur le vent et le déploiement des capteurs. Notre étude suggère que la croissance et la productivité des zostères diffèrent selon l'environnement physique et le caractère statistique des processus infrasaisonniers. Nos résultats servent à étayer les décisions de conservation liées à la protection des zostères, et peuvent être utilisés pour prédire la réponse de la zostère aux changements futurs.

INTRODUCTION

Seagrass beds are important nearshore habitats, providing numerous valuable ecosystem services such as fisheries maintenance, carbon sequestration, water filtration, and shoreline protection (Barbier et al. 2011, Cullen-Unsworth and Unsworth 2013). Despite their well-recognized role in maintaining ecosystem integrity, seagrass beds have experienced worldwide declines over the last several decades (Waycott et al. 2009, Dunic et al. 2021). While both environmental factors and human disturbances can negatively impact seagrasses, changing environmental conditions are considered key drivers of seagrass growth and productivity (Lee et al. 2007). Characterizing the physical conditions inhabited by seagrass beds is thus a critical step towards understanding seagrass resilience to change, and can ultimately provide a mechanistic basis to inform seagrass management and conservation.

Water temperature and light availability are key environmental factors that regulate seagrass growth and productivity (Lee et al. 2007). In temperate seagrasses, seasonal changes in temperature and light supports higher growth and productivity in the spring and summer, with declines through the fall and winter. Seagrasses also respond to shorter-term variations in temperature and light that occur on time scales with periods shorter than the seasonal scale, or sub-seasonal variations (Krumhansl et al. 2021). Short-term variability in underwater light results from turbidity events related to storms, wind events, runoff, and anthropogenic activities (e.g., dredging). In response, seagrasses will change their physiology and morphology to improve light capture, decrease shoot density and biomass to reduce their respiratory burden, and mobilize stored carbohydrates as a carbon source (Wong et al. 2020, Wong et al. 2021). These responses allow carbon balance to be maintained for continued growth and survival. While chronic long-term light reduction has typically been assumed most relevant for seagrass decline, short-term variability in available light is also a key stressor for seagrasses (Wong et al. 2020, Wong et al. 2021).

Temperature variability that occurs on short time-scales superimposed on the seasonal signal are also important determinants of seagrass growth and productivity (Strydom et al. 2020, Krumhansl et al. 2021). Localized warm water events that last for several days or weeks can result from solar heating, and are particularly prevalent in shallow protected areas that have reduced flushing and water motion, which are often important habitats for seagrass. While seagrass photosynthetic performance tends to increase with temperature, an optimum exists above which respiration outpaces photosynthesis (Marsh et al. 1986). Negative carbon balance will result if the respiratory burden cannot be reduced through morphological and biomass changes, or if carbohydrate stores are insufficient to meet carbon demands. In addition to localized warm water events, larger-scale marine heat waves can influence entire regions and have been linked to large-scale seagrass die-offs (Marbà and Duarte 2010, Strydom et al. 2020).

In Atlantic Canada, the dominant seagrass (eelgrass, *Zostera marina*) is found across a wide range of environmental conditions, including in shallow, warm, protected waters with muddy/silty sediments as well as in deep, cool, exposed waters with sandy sediments (Wong 2018, Krumhansl et al. 2020). Previous work indicates that eelgrass condition (i.e., productivity and resilience to disturbance) is strongly shaped by the surrounding environment (Wong et al.

2013, Wong et al. 2020, Krumhansl et al. 2020). In particular, aspects of light and temperature that occur on short-time scales were identified as important determinants of eelgrass condition. However, the dynamics of these prominent short-term physical processes have yet to be fully characterized across the main growing season. Furthermore, additional metrics of light availability commonly used within management frameworks, namely water turbidity, have not been examined or linked to more biologically relevant measures. Here we address these limitations by characterizing water temperature, light availability, and water turbidity across eelgrass sites on the Atlantic coast of Nova Scotia. We also characterize water depth, current speed, and wave exposure given their strong influence on both temperature and light dynamics. This study provides a comprehensive baseline of physical conditions and characterizes physical processes important for seagrass condition across different time-scales. We examine relationships between various physical measures, present different data interpretations, and evaluate their usefulness for management decisions and for advancing understanding of seagrass ecology. The results can be used to further refine predictive relationships between physical processes and seagrass condition, inform management decisions surrounding seagrass conservation, and evaluate current thresholds used within management frameworks.

MATERIALS AND METHODS

Field sites

Sub-seasonal physical processes were evaluated at 6 seagrass beds on the Atlantic coast of Nova Scotia from May to October 2020 (Figure 1). The field sites spanned varying environmental conditions that differed in temperature, water depth, light availability, wave exposure, sediment type, and currents (Wong 2018, Krumhansl et al. 2020). As such, these sites represent the range of environmental conditions that seagrass beds inhabit in coastal Nova Scotia. Various aspects of seagrass ecology (e.g., phenology, reproductive ecology, faunal biodiversity and production, plant condition; Wong et al. 2013, Wong 2018, Wong and Dowd 2016, Wong and Kay 2019, Krumhansl et al. 2021, Vercaemer et al. 2021) have been studied at these sites. This work builds on those past studies, providing insight into the physical processes that influence bed characteristics and properties.

Characterizing physical processes

Water temperature, depth, light availability, turbidity, and currents were measured using continuously recording instruments anchored to the seabed on concrete blocks or large chain. Data acquired were comprised of times series recorded at high sampling rates, typically every 10 minutes for several months. Instruments were deployed within the seagrass beds, at least 10m away from deeper tidal channels and the bed edge. Measurements were intended to represent the conditions that seagrass experience at each site, and as a result, instruments at some shallow sites were exposed at low tide. Most instruments were deployed for the duration of the main growing season (May to October 2020), although some logistical challenges resulted in shorter

deployments at some sites. Sediment type, sediment organic content, and bottom slope were measured in previous studies (Krumhansl et al. 2021) and are reported here. Below we provide further details into the collection and analyses of the field data.

Water temperature

Water temperatures were recorded at 15-mins intervals using HOBO temperature tidbits (Onset Corp.). The time series data were summarized across the main growing season (June 1 to October 31 2020) by calculating the mean, standard deviation (SD), coefficient of variation (SD/mean), maximum, minimum, 95th percentile of the data, total time between 5 and 23 °C degrees (outside of which growth and photosynthesis are compromised), and mean daily temperature range. The exception was at Sambro, where data were summarized between August 14 to December 12 2020 due to a delayed deployment. Temperature loggers at Port l'Hebert and Port Joli were sometimes exposed to the air during low tide. We retained these data because they represent conditions to which seagrass were exposed. Seagrass physiology and growth can be affected by desiccation and heat stress during air exposure (Leuschner et al. 1998, Kim et al. 2016).

The temperature time series were further processed to isolate signals in different frequency bands related to seasonal, meteorological, and tidal processes. The seasonal temperature signal at each site was isolated using a smoothing spline. The de-seasonalized time series (i.e., the temperature anomaly) were then obtained by subtracting the spline-fitted seasonal cycle from the original temperature time series. The meteorological frequency band was obtained by applying a low pass digital filter to the temperature anomaly time series to remove high frequency features shorter than 48 hours (Priestley 2004). The meteorological frequency band thus includes processes between 48 hours to ~60 days, such as wind-driven upwelling. The tidal frequency band was isolated by subtracting the meteorological band from the temperature anomaly, and includes tidal and daily heating and cooling processes operating on time scales shorter than 48 hours. The R package 'signal' (Signal developers 2014) was used for signal processing of the data to partition it into the different frequency bands.

Temperature data from the different frequency bands were then analysed to characterize processes occurring over those different time scales. Temperature variation in the meteorological and tidal bands was calculated as the standard deviation within each band. The importance of short-time scale processes such as tides and solar heating in influencing water temperature relative to medium-time scale processes such as wind-driven upwelling was calculated as the ratio of the SD tidal band to SD meteorological band. Spectral analysis was used to identify the most dominant frequencies and periods of variation within each temperature time series (Priestley 2004). Spectral analyses were conducted using the function spec.pgram in the R package 'stats' (R Core Team).

Warm water events were also characterized using the raw temperature records, because water temperatures can negatively impact seagrass growth and photosynthesis. The mean photosynthetic temperature optimum for *Z. marina* determined by a literature review is 23 °C,

above which photosynthetic to respiration (P:R) ratios can become negative causing reduced growth and survival (Lee et al. 2007). We used this as our temperature threshold and identified warm water events as those occurring above this threshold for a minimum of 2 hours, with distinct events separated by 3 days or more (Oliver et al. 2018, Krumhansl et al. 2020). For each event, the duration, start and end date, and maximum and minimum temperatures were determined. The thermal integral was also calculated as the area under the temperature curve for each event, as an indication of the additional heat entering the system above the physiologically relevant thresholds.

Photosynthetic Active Radiation (PAR)

Underwater PAR (400-700 nm) was measured at 1-minute intervals using DEFI2-L sensors (JFE Advantech). Two sensors were deployed concurrently at the same location within the seagrass bed, with one at the bottom and the other higher up in the water column. The distance between the two sensors remained fixed, and was 0.5m at shallow sites (PH, PJ) and 1m at the remaining deeper sites. At the shallow sites, the sensors were oriented to measure downwelling irradiance with the sensor facing the water surface. Prior to analyses, data were low-pass filtered (using the R package 'signal') to remove high frequency aspects less than 20 minute periods that were unrelated to light availability for seagrass plants, such as focused light through surface ripples (caustics) and temporary blockage of the sensor by leaves and detritus. Low light values (20 µmol m^{-2} sec^{-1}) that typically occurred at night were also removed, as well as when any values from the top sensor were less than the bottom sensor (likely due to measurement error).

These quality controlled data were used to calculate the mean, SD, maximum, and minimum bottom PAR at each site. The light attenuation coefficient (K_d) was also calculated for each 1min reading as:

$$I_{z_2} = I_{z_1} e^{-K_d \Delta z}$$

where I_z is the value of PAR at depth z, with z_1 and z_2 being the depth of the sensor closer to the surface and the bottom sensor, respectively, and $\Delta z = z_2 - z_1$. Daily median, mean, and SD of K_d, as well as overall maximum K_d, were then calculated from these data. Note that because the bottom light sensors were deployed within the eelgrass beds, light attenuation coefficients represent the absorption properties of both the water column and seagrass canopy.

Turbidity

Turbidity was measured every 5 minutes using RBR virtuoso instruments with Seapoint sensors (RBR Ltd.). Turbidity records typically contained many spikes which far exceeded the median values of the records (typically 1 to 10 NTU, nephlometric turbidity units) and were usually of very short duration (e.g., single time steps). These spikes were likely instrument or environmental artifacts and not representative of the general underwater turbidity. Hence, the time series were first de-spiked to remove all values less than one and greater than 500 NTU.

The time series were then detrended by removing a linear trend from log turbidity, to reduce the effect of large positive spikes and to account for drift due to, for example, fouling. The data were then returned to the original units (exponentiated) and a two stage de-spiking procedure was applied, where all values below 1 and above 100 NTU were removed. This was followed by a running median de-spiking procedure to remove remaining anomalies. Note that detrending was done prior to this final de-spiking because the presence of a strong trend can complicate the detrending procedure. The detrended and de-spiked time series were then low-pass filtered to remove frequencies higher than 2 hours, associated with instrument and environmental artifacts. The final quality controlled data were used to calculate daily median, mean, and SD turbidity, as well as overall maximum turbidity. Laboratory calibrations to relate NTU to particle concentration (mg L^{-1}) were conducted using bottom sediments for each site. Turbidity records were processed the R packages 'signal' (Signal developers 2014) and 'oce' (Kelley et al. 2021).

Current speed

Current speed was measured using electromagnetic current meters (Infinity-EM AEM, JFE Advantech) at Port l'Hebert, Port Joli, Mason's Island, Sacrifice Island, and an upward-looking Acoustic Doppler Current Profiler (ADCP) (2MHz, Nortek Aquadopp) at Sambro and Taylor's Head. Electromagnetic current meters were deployed perpendicular to the sea bottom, with current speed and direction measured every 15 minutes using burst sample averaging (1 recording obtained by averaging 1 second measurements over 10 seconds). The ADCP was deployed at 0.10 m above the sea bottom and data recorded in burst mode at 8 Hz and 4800 samples. This enabled measurement of both current velocities and orbital velocities due to waves. Current speeds $\geq$ 10 cm sec^{-1} were removed at Port Joli and Port l'Hebert, as these were associated with exposure at low tide. Current data were used to calculate mean, median, SD, maximum, and minimum current speed at each field site.

The current speed time series were then filtered (using the R package 'signal') to isolate signals into different frequency bands corresponding to meteorological and tidal processes (seasonal variations are not relevant here). The meteorological band was isolated using low-pass filtering to remove frequencies shorter than 48 hours. The tidal band was then isolated by subtracting the meteorological band from the raw current data. Note that further analysis of tidal constituents of the current data was beyond the scope of this work.

Depth

Water pressure was measured at 10-minute intervals using HOBO pressure sensors (Onset Corp). The data were used to calculate water depth (d, in meters) at each time interval via Onset software as:

$$d = \frac{P_{total} - P_{atmos}}{\rho \times g}$$

where P_{total} is the pressure recording, P_{atmos} is standard atmospheric pressure (1.01 x 10^5 N m^{-2}), ρ is the density of seawater (1.03 x 10^3 kg m^{-3}), and g is the acceleration of gravity (9.80 m s^{-1}). The depth time series was summarized by first isolating the highest and lowest water depth for each tidal cycle (using package 'VulnToolkit' in R, Troy and Anisfeld 2021), and then calculating mean depth at high tide and mean depth range. The tidal portion of the time series was isolated by first fitting a smoothing spline to the original time series, to capture the fluctuations associated with changes in atmospheric pressure. The tidal series was then obtained by subtracting the spline fit form the original series.

Wind

Wind speed data were obtained for the Shearwater RCS weather station (44.63, -63.51) from Environment Canada. Data were recorded hourly (as 2-min averages of wind speed and direction for each hour) for 2020. Wind stress (τ, in Pa) were calculated from these data as:

$$\tau = C_D \times \rho_a \times U^2$$

where C_D is a dimensionless drag coefficient (0.0014), ρ_a is the density of air (1.22 kg m^{-3}), and U is the hourly wind speed (m s^{-1}). Low pass digital filtering was applied to the wind stress time series to isolate the meteorological frequency band, by removing high frequency features shorter than 48 hours, which in practice means removal of the diurnal signature.

Wave exposure

A relative wave exposure index (REI) was calculated for each site, modified from Keddy (1982) and as used in Fonseca et al. (2002) and Wong (2018):

$$REI = \sum_{i}^{8} (V_i \times P_i \times F_i)$$

where i is the compass heading in 45°increments (i.e., centred on north, northeast, east, etc.), V is the average annual wind speed (km h^{-1}), P is the wind frequency, and F is the effective fetch (km). Wind data were obtained for the Shearwater weather station as described above. Fetch was defined as the distance from the site to land along a given compass heading (Shore Protection Manual 1975), with a maximum distance of 300 km. Fetch was calculated using the R package 'fetchR' (Seers 2018). Effective fetch was computed by first measuring fetch at 11.25° increments from a given compass heading. Then, effective fetch for each compass heading i was determined as:

$$F_{i=} \frac{\sum_{j=1}^{9} X_j \times cos\alpha_j}{\sum_{j=1}^{9} cos\alpha_j}$$

where j is the 11.25 increments on either side of and including the compass heading i, X is fetch (km), and α is the angle of the j^{th} departure from the i^{th} compass heading (Shore Protection Manual 1975).

RESULTS

General site properties

The seagrass beds studied ranged in mean depth at high tide from 1.47 to 8.44m (Table 1). Port l'Hebert and Port Joli had the shallowest mean depths at high tide and Sambro the deepest. The mean depth range (resulting from tidal and atmospheric conditions combined) across all sites was 1.30 to 1.44m, with the smallest range at Taylor's Head and the largest at Port l'Hebert. Seagrass beds differed greatly in their slope angle from shore, with Port Joli having negligible slope (0.14°), Port l'Hebert, Mason's Island, and Sacrifice Island having intermediate slopes (1.82 to 3.54°), and Taylor's Head and Sambro having large slopes (4.55 and 6.01°, respectively). Previous measurements of percent sand in sediments indicated that some sites were very muddy/silty (20.3, 22.4, 28.8% sand at Port l'Hebert, Port Joli, and Mason's Island, respectively, with remaining percentage being mud/silt), while the remaining sites had more sandy sediments (59.5, 81.6, 84% sand at Sacrifice Island, Taylor's Head, and Sambro, respectively). Sites with high sand content (Taylor's Head, Sambro) were more wave exposed than muddy/silty sites.

Temperature

Mean summer water temperatures ranged from 13.7 to 18.4°C across the seagrass beds examined (Table 2). The warmest sites were Port l'Hebert and Port Joli (~18°C) and coolest sites were Sambro and Taylor's Head (13.7°C and 14.1°C, respectively) (Table 2, Figures 2, 6a – 11a, top panels). Observation of the SD and CV indicate that the warmest sites also had the highest temperature variation. Maximum temperatures at Port l'Hebert and Port Joli were 28.4 and 29.6°C. These sites also had the lowest recorded temperatures (~0°C), which resulted when the beds were exposed at low tide in the early summer (Figure 2).

Warm water events where temperatures exceeded the 23°C threshold (i.e., temperature optimum for photosynthesis for *Z. marina*) were only observed at Port l'Hebert and Port Joli (Table 3, Figures 2, 6a – 11a top panels), where four and six events were observed across the summer, respectively. Mean temperatures of each event were between 23.5 and 24.5°C, with maximum temperatures reaching 29.6°C. Duration of events ranged from 5.25 to 258.5 hours, with water temperatures exceeding the 23°C threshold for a total of 412 and 403 hours at Port l'Hebert and Port Joli, respectively. These sites thus had lower total time between 5 and 23°C and higher daily temperature ranges compared to all other sites (Table 2).

All sites showed a general seasonal trend of increasing water temperature during the spring to reach a maximum in August before declining throughout the fall (Figures 2, 6a-11a, top

panels). Temperature changes within the meteorological band were generally coherent across sites, suggesting the strong influence of coast-wide processes in determining water temperatures. However, some sites exhibited higher amplitude changes than others (i.e., Sambro, Taylor's Head; Figure 2, middle panel). The meteorological band for Port Joli and Port l'Hebert temperatures were strongly coherent, and almost overlapped (Figure 2, middle panel). Temperature changes in the meteorological band sometimes reflected preceding changes in wind stress, suggesting the role of wind-driven coastal upwelling in large temperature changes (Petrie et al. 1987) (Figures 6a-11a, bottom panel). However, this relationship did not persist consistently across the temperature records at any of the sites, suggesting the importance of other coastal processes. Processes within the meteorological band appear to dominant temperature dynamics at most sites, as the ratios of SD tidal to meteorological band were almost always less than 1 (Table 2). The exception was at Mason's Island, where the ratio was 1.20.

Temperature variations within the tidal band were greatest at Port Joli and Port l'Hebert (Figure 2, bottom panel). At most sites, heating and cooling periods related to solar heating and daily tides, as well as the M2 tidal exchange, were evident (Figures 6b – 9b, 11b). The exception was at Sambro, where heating and cooling occurred primarily on the longer seasonal time scales (Figure 10b). Observation of the power spectra indicate that solar heating and daily tides dominated temperature changes at Port l'Hebert, Port Joli, and Sacrifice Island (Figures 7c – 9c). This is due to the presence of a strong temperature gradient and strong advection. The largest influence of solar heating and daily tides was observed at Port l'Hebert, one of the warmest sites. At Port Joli, also a warm site, M2 tidal variations in temperature were more important relative to Port l'Hebert. Temperature variations at Mason's Island were equally influenced by both solar heating and daily tides, as well as M2 tides (Figure 6c). At Sambro, where daily heating and cooling was not evident, the temperature spectrum is dominated by slow variation in offshore processes (Figure 10c). This is also observed at Taylor's Head, although there is more influence of the shorter frequency processes relative to Sambro (Figure 11c).

Photosynthetic Active Radiation (PAR)

Mean bottom PAR ranged from 23.3 to 173.5 µmol m^{-2} s^{-1} across the seagrass beds, with highest values at the shallowest sites (Port Joli, Port l'Hebert) and lowest values at the deeper sites (Sambro, Taylor's Head) (Table 4). Highest variation in bottom PAR was observed at the shallowest sites. Upper sensors consistently recorded higher PAR than bottom sensors, as expected (Figures 12a – 17a, top panels), and a general trend in decreasing seasonal light after the summer solstice was evident. Daily median light attenuation coefficients (K_d) ranged from 0.45 to 1.39 m^{-1}, and were highest at sites with muddy/silty sediments that are easily resuspended during wind events (i.e., Port l'Hebert, Port Joli, Mason's Island) and lowest at sites with sandy sediments (Taylor's Head, Sacrifice Island) (Table 4, Figure 3). Note that the high K_d at Sambro (1.39 m^{-1}) is likely an artifact of the sensor being fouled or covered, as previous work indicates this is typically a clear water site (Krumhansl et al. 2020). Median daily K_d was relatively stable across the growing season, particularly at Port l'Hebert which had the lowest SD despite having some of the highest K_d values (Figures 12a – 17a, bottom panel). K_d increased in the fall at

Mason's Island, Port Joli, and Sacrifice Island, either from increased resuspension from wind events or increased detritus covering the sensors. Strong relationships between daily median K_d and daily median wind stress were not evident (Figure 12b – 17b) except at Port Joli, where a positive relationship was observed ($R^2 = 0.204$).

Turbidity

Mean daily turbidity ranged from 1.95 to 11.51 NTU (Table 5). High variability in turbidity was evident across all sites, with SD being either equal to the mean or higher (Table 5). Turbidity records exhibited numerous spikes in values despite the extensive quality control of the initial data, which may be related to particle packaging, plant matter covering the sensors, or bursts of high concentrations of sediment(Figures 18 – 23, top panel), perhaps exacerbated by the near bottom deployments. Muddy/silty sites (Port l'Hebert, Port Joli, Mason's Island) had higher turbidity than sandy sites (Sacrifice Island, Sambro) (Figure 4). The exception was Taylor's Head, where turbidity was the highest of all sites, despite having sandy sediments. Unfortunately, it is not possible to disentangle if this estimate is artificially inflated from the tall, dense seagrass plants and/or high macrophyte detritus covering the sensor, or if turbidity readings represent natural turbidity. Turbidity time series were overlaid with wind stress and current anomaly (not shown), but no strong relationships were evident. Relationships between turbidity and K_d were also not evident at any site (Figures 18 – 23, bottom panel). Calibration of NTU units to the more biologically meaningful units mg L^{-1} indicated that median daily turbidity ranged from 8.3 – 42.9 mg L^{-1} (Table 5; Figure S1).

Currents

Mean current speed was relatively low across all field sites, ranging from 1.30 to 9.25 cm s^{-1} (Table 6, Figure 5, top panel). Slowest currents were observed at Mason's Island, Sacrifice Island, and Sambro (1.30, 2.12, 2.41 cm s^{-1}, respectively), intermediate currents at Port l'Hebert and Port Joli (4.68, 5.09 cm s^{-1}, respectively), and highest current at Taylor's Head (9.25 cm s^{-1}). Maximum current speed observed was highest at Sacrifice Island (21.2 cm s^{-1}), with lowest speed observed at Mason's Island (0.13 cm s^{-1}).

Current speed variation within the meteorological band differed greatly across the field sites, increasing as mean current speed increased (Figure 5, middle panel). There was little coherency in current speed in the meteorological band among the field sites. Current speed and wind stress anomaly were only strongly related at Sacrifice Island and Sambro, although some coherency was evident on short time scales across all sites (Figures 24a – 29a, bottom panels).

Current speed anomalies within the tidal band also differed across the field sites, being highest at Mason's Island and Taylor's head, intermediate at Port Joli and Port l'Hebert, and lowest at Sacrifice Island and Sambro (Figure 5, bottom panel). Current speed anomalies tended to peak at mid-depth on the flood tide at Mason's Island, Sacrifice Island, and Sambro (Figures 24b – 29b), while phasing was more offset at Port l'Hebert, Port Joli, and Taylor's Head.

DISCUSSION

Our study shows that *Zostera marina* on the Atlantic coast of Nova Scotia inhabits a wide range of physical conditions, from beds in shallow, warm, protected sites with muddy/silty sediments to beds in deeper, cooler, exposed sites with sandy sediments. Mean summer water temperatures differed by almost 5°C across the seagrass beds examined, with several extreme warm water events observed at two shallow sites. Light attenuation (by the water column and seagrass canopy combined) was highest at shallow sites, likely as the muddy sediments were easily resuspended, while bottom PAR also remained highest at these sites because of the shallow depths. Water turbidity was highly variable within each site, but tended to be highest at sites with high light attenuation. Previous studies have suggested that sub-seasonal physical processes (i.e., warming events, wind events, upwelling) are important for eelgrass growth and productivity (Wong et al. 2013, Wong et al. 2020, Krumhansl et al. 2021, Wong et al. 2021), and so we further evaluated variability in temperature and light across differing time scales. We focused on dynamics during the main growing season (June to October), as this is the critical growth period. Below, we highlight important outcomes of these analyses and discuss the implications for eelgrass growth and productivity.

Water temperature is well recognized as an important driver of seasonal growth in temperate seagrasses (Lee et al. 2007, Staehr and Borum 2011). At all sites, seasonal patterns in water temperature were evident, where cooler temperatures in the spring warmed to maximum temperatures in the summer before cooling in the fall. However, despite similarities in overall seasonal temperature trends, temperature variability on sub-seasonal scales substantially differed across sites. Processes that occurred on temporal scales <48 hours dominated at shallow sites (i.e., Port l'Hebert, Port Joli, Mason's Island), as evidenced by larger daily temperature range, higher temperature variability in the tidal band, and larger importance of solar heating and the daily tide relative to the M2 tide compared to other sites. Solar heating of the shallow water, particularly when low tide coincided with solar noon, played a key role in short-term temperature dynamics at shallow sites. Warm water events that exceeded the optimum temperature for photosynthesis (23°C) were evident at Port l'Hebert and Port Joli, likely resulting from extended periods of solar heating over the extensive shallow flats combined with a partial restriction in tidal flushing (Wong et al. 2013). Individual warm water events lasted from 2.25 to 258 hours. Previous studies have shown that physiological impacts on eelgrass occur within 1 to 7 days when temperatures exceed 19 to 28°C (Evans et al. 1986, Gao et al. 2017) or even as quickly as 15 minutes when temperatures exceed 30°C. During warm water events at our sites, mean temperatures were ~24°C while maximum temperatures approached 30°C, and so it is very likely that eelgrass experienced negative physiological responses. Furthermore, warming events can also cause persistent changes in eelgrass bed characteristics across multiple clonal generations and years (DuBois et al. 2020), with these beds typically having higher density, aboveground to belowground biomass ratio, and shoot length. Previous studies suggest these responses are evident at our sites where warm water events are prevalent (Wong et al. 2013, Wong 2018,

Krumhansl et al. 2021). However, similar to other seagrass species, eelgrass can thermally adapt to varying temperature regimes (Staehr and Borum, Marin-Guirao et al. 2016). While we used a literature value of 23°C for the temperature optimum for photosynthesis, this value needs to be further refined for plants from both warm and cool sites, in order to fully understand eelgrass vulnerability to warming events in Atlantic Canada.

Temperature variations within the meteorological band (i.e., 48 hours to ~60 days) dominated the temperature signal at almost all sites, including those where warm water events occurred. This indicates the overall importance of coast-wide processes such as storms and wind-driven upwelling. Some coherence between the meteorological temperature bands and wind stress was evident, although strong relationships did not persistent across the entire time series at any site. This is not surprising, given that temperature depends strongly on wind stress history and its direction, and not its instantaneous values. Calculation of wind stress based on the dominant direction that causes coastal upwelling in Nova Scotia (winds to the northeast; Petrie et al. 1987) would also likely result in stronger relationships. In fact, a coastal upwelling index based on Ekman transport and NE winds showed strong coherence with the meteorological temperature band for the same eelgrass sites in previous years (Krumhansl et al. 2021). Coastal upwelling brings cool nutrient rich water to the surface, promoting seagrass growth and photosynthesis when nutrients are limited (Sandoval-Gil et al. 2019). Further temperature variations within the meteorological band are likely related to local wind-effects, which were not captured by the wind data available, as well as other coastal processes. Refinement of these local scale winds might explain the strong coherence observed in the meteorological temperature bands between certain geographically close sites (i.e., Port Joli and Port l'Hebert, Mason's Island and Sacrifice Island).

In addition to temperature, light is also considered a key driver of seagrass growth and productivity. Our study provides the first *in-situ* extensive time series measurements of underwater PAR for eelgrass beds in Atlantic Canada, and furthermore includes two sensors separated by a known distance, allowing calculation of light attenuation coefficients (K_d). Because the bottom sensors were deployed inside the eelgrass beds, K_d here represents light attenuation by both the water column and seagrass canopy. Median light attenuation (K_d) ranged from 0.34 to 1.39 m^{-1}, being highest at muddy/silty sites (i.e., Mason's Island, Port Joli, Port l'Hebert), where wind events could easily resuspend bottom sediments. Elevated K_d also likely resulted from high concentrations of coloured dissolved organic matter (CDOM), originating from the extensive wetlands surrounding these sites (Aitkenhead-Peterson et al. 2005, M. Wong, pers. obs.). Although relationships of K_d with wind stress were relatively weak, these would likely improve with more refined local wind data and/or by placing sensors outside the eelgrass beds to remove the canopy effect. Prolonged seasonal winds during the early growing season (March to May) also cause long periods of high water turbidity (M. Wong, pers. obs.), but our instruments were not deployed early enough to capture these events. The median K_d values observed in our study are within the range that *Z. marina* can tolerate (0.16 to 1.5m^{-1}; Dennison et al. 1993), although our maximum values often exceeded this range. Despite periodic low light conditions, eelgrass has persisted at our field sites for many years, suggesting the plants receive the minimal light required for carbon balance (~15% surface incidence light; Lee et al. 2007).

Plants likely achieve this by a combination of direct light harvesting when conditions are ideal, and by employing various strategies to improve light capture or reduce respiratory burden when conditions are sub-optimal. A previous study at our field sites found that eelgrass acclimated to low light conditions by growing longer sheaths and leaves, reducing the number of leaves per shoot, and reducing belowground biomass (Wong et al. 2020, Krumhansl et al. 2021).

Our study also provides the first *in-situ* continuous time series of water turbidity in eelgrass beds in Atlantic Canada. Turbidity is a measure of water clarity, based on the amount of light scattered by material in the water. As such, it influences light availability, rather than measuring light itself. The mechanism by which turbidity impacts seagrass is through light reduction, and so turbidity measurements are most relevant for seagrass when related to some measure of light availability. We included turbidity in our study because it is extensively relied on by managers in DFO Fish and Fish Habitat Protection Program (DFO-FFHPP) to measure potential habitat impacts during works and activities. Turbidity records across all our field sites were highly variable with many large single spikes, despite extensive quality control of the raw data. Most median daily turbidity estimates were highest at muddy sites (i.e., Mason's Island, Port l'Hebert, Port Joli), similar to patterns in K_d and as would be expected. However, highest values were recorded at Taylor's Head. On potential issue is that instruments were deployed within the seagrass beds, in an effort to characterize turbidity within the beds themselves. Given their location, it is possible that plant material repeatedly blocked the sensor and contributed to the spiky nature of the time series. However, these spikes could also have resulted from the natural sediment dynamics in these systems, with particle packaging (i.e., flocs vs single grains), particle dynamics (i.e., aggregation vs breakup, deposition vs. resuspension), and sediment composition and particle size distributions all influencing optical measures and spikes in turbidity. Deployment of turbidity sensors further up in the water column, rather than on the sea bottom within the eelgrass beds, would allow us to determine if spikes resulted from plant interference or represent the natural turbidity dynamics of these systems.

Contrary to expectations, no relationships were evident between turbidity and K_d at any of the field sites. This is likely related to differences in what the turbidity and light sensors measure. Turbidity sensors measure scattering properties of the water mass in front of the sensor (within 5cm), while light sensors measure the available light at the sensor. The light attenuation coefficient K_d is calculated from light readings at two different depths, and represents light absorption in the water column and by the seagrass canopy. Because our bottom light sensors were placed directly on the bottom inside the eelgrass bed, measurements include not only light transmission through the water column but also the effects of canopy shading. This contrasts with the turbidity sensor which measure only the scattering properties of the water, and is related to water column light attenuation due to suspended particulates. To fully resolve the relationship between turbidity and K_d, instrument deployments should be changed to provide more comparable data. Light sensors should be deployed outside of the seagrass beds or within bare patches, to remove the effect of canopy shading, while turbidity sensors should deployed in the water column to reduce interference from plant matter. Different recording time steps of the turbidity sensors should also be considered to reduce the dominance of data spikes. Without this refined relationship, it is difficult to convert turbidity measured in NTU units to representations

more biologically meaningful for eelgrass, such as light attenuation or optical depth ($1/K_d$). This is a major challenge for DFO-FFHPP who use a threshold of 8 NTU above background levels to identify impacts on eelgrass (Canadian Water Quality Guidelines for the Protection of Aquatic Life). This threshold is derived from fish response to sediment loading, and its relevance for eelgrass is unknown. It is critical that future research elucidate the relationship between turbidity (in NTU) and light availability in eelgrass beds. Only then can relevant thresholds be applied to the background estimates of turbidity identified in this study to evaluate impacts on eelgrass.

Further insight into the impacts of water turbidity on eelgrass can be gained by converting turbidity to total suspended solids (TSS). Site-specific calibrations must be conducted, as sediment type can highly influence turbidity and TSS values. Our calibrations indicate that median daily TSS ranged from 8.30 to 42.9 mg L^{-1}, within the range of previous measurements (Wong et al. 2013). DFO-FFHPP uses a TSS threshold of 20 mg L^{-1} to identify harmful alteration, disruption, or destruction (HADD) of eelgrass. The biological basis of this threshold is unclear, although it is similar to those used in other areas, such as Chesapeake Bay where <15 mg L^{-1} is suggested to maintain optimal eelgrass conditions in polyhaline areas (>18 psu) (Moore and Short, 2006). Our study suggests that background TSS may actually be higher than these thresholds, although the role of observed turbidity spikes requires further investigation. The current use of these TSS thresholds thus provides a cautionary approach to the management of eelgrass.

In addition to temperature, light, and turbidity, we also evaluated water currents at our seagrass sites. Although current speed is not typically considered a primary driver of eelgrass productivity and growth, it can strongly impact the overall bed structure. In a previous study where eelgrass beds were exposed to currents from 5 to 37 cm s^{-1}, plant cover decreased with increasing current while bed fragmentation became more pronounced (Fonseca and Bell 1998). Higher current speeds can also decrease silt/clay and organic content of sediments when the clay fraction is <10%, likely supporting plant health through increased redox potential and reduced sulphide concentrations (van der Heide et al. 2009). Based on this, eelgrass beds are thought to thrive at intermediate current speeds. In our study, mean current speeds were all relatively low ($\leq$5 cm s^{-1}) at all sites except for Taylor's Head, where it was 9.25 cm s^{-1} and ranged from 1.67 to 17.13 cm s^{-1}. Our current speeds are on the low end or below the range marine angiosperms are thought to tolerate (5 – 180 cm s^{-1}, Koch 2001), but are also below current speeds that cause high reduction in cover and increase bed fragmentation (~20 cm s^{-1}, Fonseca and Bell 1998). The low current speeds at our sites, combined with maximum speeds between 10 to 20 cm s^{-1}, likely support eelgrass health through nutrient delivery, sediment ventilation, and water flushing.

In summary, our study provides a comprehensive characterization of the physical conditions inhabited by eelgrass on the Atlantic coast of Nova Scotia. We highlight the sub-seasonal (short-term) dynamics of water temperature, underwater light, turbidity, and water motion, identifying processes that may impact eelgrass growth and productivity. These include solar heating and resultant warm water events, tidal and meteorological temperature variation, variations in light attenuation and water turbidity, and patterns in winds and currents. Water temperatures that exceeded published physiological thresholds were evident at some sites,

suggesting negative impacts on eelgrass. However, temperature thresholds (i.e., temperature optima for photosynthesis) need to be further refined for our region, as eelgrass can adapt to different thermal regimes. Improvements to deployment strategies for PAR and turbidity sensors will allow better characterization of light and turbidity relationships, with local wind data providing insight into the role of wind-driven sediment resuspension. Baseline conditions in underwater light would also be improved by data from the early growth period (i.e., March-May), when wind events are frequent. Regardless, our study provides useful insight into the sub-seasonal processes important for eelgrass. Previous relationships of eelgrass condition and physical processes can be further improved, allowing better prediction of eelgrass response to future environmental change. Ultimately, our study provides the basis for guiding conservation of eelgrass beds, allowing targeted protection of resilient beds and maintenance of overall ecosystem functioning.

ACKNOWLEDGEMENTS

We thank B. Law for providing the ADCP and turbidity instruments, and for discussions on water turbidity. We also thank S. Roach for providing field support to deploy instruments at Sambro. B. Law and E. Horne provided useful comments that improved the manuscript. Funding was provided by DFO Fish and Fish Habitat Protection Program (FFHPP).

REFERENCES

Aitkenhead-Peterson, J. A., Alexander, J. E., and Clair, T. A. 2005. Dissolved organic carbon and dissolved organic nitrogen export from forested watersheds in Nova Scotia: Identifying controlling factors. Glob. Biogeochem. Cycles 19: 1-18.

Barbier, E. B., Hacker, S. D., Kennedy, C., Koch, E. W., Stier, A. C., and Silliman, B. R. 2011. The value of estuarine and coastal ecosystem services. Ecol. Mono. 81: 169–193.

Cullen-Unsworth, L., and Unsworth, R. 2013. Seagrass meadows, ecosystem services, and sustainability. Environment: Science and policy for sustainable development, 55: 14-28.

Dennison, W. C., Orth, R. J., Moore, K. A., Stevenson, J. C., Carter, V., Kollar, S., Bergstrom, P. W., Batiuk, R. A. 1993. Assessing water quality with submersed aquatic vegetation. BioScience 43: 86- 94.

DuBois, K., Williams, S. L., and Stachowicz, J. J. 2020. Previous exposure mediates the response of eelgrass to future warming via clonal transgenerational plasticity. Ecology 101: 1-12.

Dunic, J. C., Brown, C. J., Connolly, R. M., Turschwell, M. P., & Côté, I. M. (2021). Long-term declines and recovery of meadow area across the world's seagrass bioregions. *Global Change Biology*.

Evans, A. S., Webb, K. L., and Penhale, P. A. 1986. Photosynthetic temperature acclimation in two coexisting seagrasses, *Zostera marina* L. and *Ruppia maritima*. Aquat. Bot. 24:185-197.

Fonseca, M., & Bell, S. (1998). Influence of physical setting on seagrass landscapes near Beaufort, North Carolina, USA. *Marine Ecology Progress Series*, *171*, 109–121.

Fonseca, M., Whitfield, P. E., Kelly, N. M., and Bell, S. S. 2002. Modelling seagrass landscape patterns and associated ecological attributes. Ecol. Applic. 12: 218–237.

Gao, Y., Fang, J., Du, M., Fang, J., Jiang, W., Jiang, Z. 2017. Response of the eelgrass (*Zostera marina*) to the combined effects of high temperatures and the herbicide, atrazine. Aquat. Bot. 142:41- 47.

Kelley D., Clark R., and Layton, C. 2021. *Oce: Analysis of oceanographic data*. https://cloud.r-project.org/package=oce

Kim, J-H., Kim, S. H., Kim Y. K., Park J-I, and Lee K-S. 2016. Growth dynamics of the seagrass *Zostera japonica* at its upper and lower distributional limits in the intertidal zone. Estuar. Coast. Shelf Sc. 175: 1-9.

Koch, E. W. 2001. Beyond light: Physical, geological, and geochemical parameters as possible submersed aquatic vegetation habitat requirements. Estuaries 24: 1-17.

Krumhansl, K. A., Dowd, M., and Wong, M. C. 2020. A characterization of the physical environment at eelgrass (*Zostera marina*) sites along the Atlantic coast of Nova Scotia Maritimes Region. Tech. Rep. Fish. Aquat. Sci. 3361: v + 213p.

Krumhansl, K. A., Dowd, M., and Wong, M. C. 2021. Multiple metrics of temperature, light, and water motion drive gradients in eelgrass productivity and resilience. Front. Mar. Sci. 8: 1-20.

Lee, K. S., Park, S. R., and Kim, Y. K. 2007. Effects of irradiance, temperature, and nutrients on growth dynamics of seagrasses: A review. J. Exp. Mar. Biol. Ecol. 350: 144-175.

Leuschner, C., Landwehr, S., and Mehlig, U. 1998. Limitation of carbon assimilation of intertidal *Zostera noltii* and *Z. marina* by desiccation at low tide. Aqua. Bot. 62: 171-176.

Marbà, N., and Duarte, C. M. 2010. Mediterranean warming triggers seagrass (*Posidonia oceanica*) shoot mortality. Glob. Change. Biol. 16: 2366–2375.

Marin-Guirao, L., Ruiz, J. M., Dattolo, E., Garcia-Munoz, E., and Procaccini, G. 2016. Physiological and molecular evidence of differential short-term heat tolerance in Mediterranean seagrasses. Nat. Sci. Rep. 6: 28615.

Marsh, J. A., Dennison, W. C., and Alberte, R. S. 1986. Effects of temperature on photosynthesis and respiration in eelgrass (*Zostera marina*). J. Exp. Mar. Biol. Ecol. 101: 257–267.

Moore, K.A., and Short F.T. 2006. Zostera: Biology, Ecology, and Management. In Larkum A. W. D, Orth R. J., and Duarte C (Eds) Seagrasses: Biology, Ecology, and Conservation. Springer p. 361-386.

Oliver, E. C., Donat, M. G., Burrows, M. T., Moore, P. J., Smale, D. A., Alexander, L. V., et al. 2018. Longer and more frequent marine heatwaves over the past century. Nat. Comm. 9: 1324.

Petrie, B., Topliss, B. J., and Wright, D. G. 1987. Coastal upwelling and eddy development off Nova Scotia. J. Geophy. Res. Oceans 92: 12979-12991.

Priestley, M.B. 2004. Spectral analysis and time series. Academic Press, London. pp. 877.

Sandoval-Gil, J. M., del Carmen Ávila-López, M., Camacho-Ibar, V. F., Hernández-Ayón, J. M., Zertuche-González, J. A., and Cabello-Pasini, A. 2019. Regulation of nitrate uptake by the seagrass *Zostera marina* during upwelling. Est. Coasts 42: 731-742.

Seers, B. 2018. *fetchR: Calculate Wind Fetch*. https://CRAN.R-project.org/src/contrib/Archive/fetchR/

Shore Protection Manual vol. 1. 1975. Fort Belvoir: US Army Coastal Engineering Research Center.

Signal developers (2014). *signal: Signal processing.* http://r-forge.r-project.org/projects/signal/.

Staehr, P. A., and Borum, J. 2011. Seasonal acclimation in metabolism reduces light requirements of eelgrass (*Zostera marina*). J. Exp. Mar. Biol. Ecol. 407: 139–146.

Strydom, S., Murray, K., Wilson, S., Huntley, B., Rule, M., Heithaus, M., et al. 2020. Too hot to handle: unprecedented seagrass death driven by marine heatwave in a World Heritage Area. Glob. Change. Biol. 26: 3525–3538.

Hill, T. D., and Anisfeld, S. C. 2021. *VulnToolkit: Analysis of tidal datasets*. https://CRAN.R-project.org/package=VulnToolkit.

Van der Heide, T., Peeters, E. T. H. M., Hermus, D. C. R., Katwijk, M. M. Van, Roelofs, J. G. M., and Smolders, J. P. 2009. Predicting habitat suitability in temperate seagrass ecosystems. Limnol. Oceanogr. 54: 2018–2024.

Vercaemer, B. M., Scarrow, M. A., Roethlisberger, B., Krumhansl, K. A., and Wong, M. C. 2021. Reproductive ecology of *Zostera marina* L.(eelgrass) across varying environmental conditions. Aquat. Bot. 175: 103444.

Waycott, M., Duarte, C. M., Carruthers, T. J., Orth, R. J., Dennison, W. C., Olyarnik, S., … and Williams, S. L. 2009. Accelerating loss of seagrasses across the globe threatens coastal ecosystems. Proc. Nat. Acad. Sci. 106: 12377-12381.

Wong, M. C. 2018. Secondary production of macrobenthic communities in seagrass (*Zostera marina*, Eelgrass) beds and bare soft sediments across differing environmental conditions in Atlantic Canada. Est. Coasts 41: 536–548.

Wong, M. C., and Kay, L. M. 2019. Partial congruence in habitat patterns for taxonomic and functional diversity of fish assemblages in seagrass ecosystems. Mar. Biol. 166: 1-16.

Wong, M. C., Bravo, M. A., and Dowd, M. 2013. Ecological dynamics of *Zostera marina* (eelgrass) in three adjacent bays in Atlantic Canada. Bot. Mar 56: 413–424.

Wong, M., and Dowd, M. 2016. A model framework to determine the production potential of fish derived from coastal habitats for use in habitat restoration. Est. Coasts 39: 1785–1800.

Wong, M. C., Griffiths, G., and Vercaemer, B. 2020. Seasonal response and recovery of eelgrass (*Zostera marina*) to short-term reductions in light availability. Est. Coasts 43: 120-134.

Wong, M. C., Vercaemer, B. M., and Griffiths, G. 2021. Response and recovery of eelgrass (*Zostera marina*) to chronic and episodic light disturbance. Est. Coasts 44: 312-324.

TABLES

Table 1. Location and selected physical characteristics of field sites. REI = relative wave exposure index (Keddy 1982), % sand = percent sand in sediments, % OM = percent organic matter in sediments.

Site	Latitude	Longitude	Mean depth at high tide (m)	Mean depth range (m)	Mean slope angle (°)	REI	% sand	%OM
Port l'Hebert	43.8681	-64.9633	1.62	1.44	1.82	126	20.3	19.7
Port Joli	43.8754	-64.9009	1.47	1.37	0.14	15.4	22.4	11.3
Mason's Island	44.3899	-64.2788	1.79	1.37	3.24	5.06	28.8	15.4
Sacrifice Island	44.3967	-64.2360	3.04	1.36	3.54	11.6	59.5	4.50
Taylor's Head	44.8205	-62.5719	3.71	1.30	4.55	483	81.6	1.97
Sambro	44.4554	-63.5879	8.44	1.32	6.01	173	84.0	1.77

Table 2. Temperature summary statistics for the summer period (June 1 to October 31 2020) at each site. Note that Sambro data are limited from August 14 to Dec 12 2020, and so time between 5 and 23°C is not calculated for this site. Temp = temperature, SD = standard deviation, CV = coefficient of variation.

Site	Mean Temp (°C)	SD Temp (°C)	CV	Max Temp (°C)	Min Temp (°C)	95th percentile Temp (°C)	SD Tidal Band (°C)	SD Meteoro-logical band (°C)	Ratio SD Tidal: Meteor	Time between 5 and 23°C (hrs)	Mean daily temp range (°C)
Mason's Island	15.28	2.67	0.17	22.13	7.57	18.79	0.86	0.72	1.20	3648.00	3.02
Port l'Hebert	18.46	4.14	0.22	28.39	-1.58	24.29	1.54	2.02	0.76	3191.75	5.90
Port Joli	18.40	4.16	0.23	29.59	0.93	24.27	1.66	1.98	0.84	3187.00	6.51
Sacrifice Island	14.64	2.81	0.19	21.39	6.26	18.37	0.63	1.09	0.58	3648.00	1.96
Sambro	13.68	3.15	0.23	18.68	4.84	17.63	0.53	2.68	0.20	NA	1.72
Taylor's Head	14.15	3.82	0.27	20.98	3.88	19.32	0.84	2.06	0.41	3611.00	2.27

Table 3. Summary of warm water events above 23°C at Port l'Hebert and Port Joli. Heating events were not observed at other sites. Unique events are separated by at least 3 days and are of a 2h minimum duration.

Site	Event	Start date	End date	Max Temp (°C)	Mean Temp (°C)	Thermal integral of events	Duration (hrs)
Port l'Hebert	1	2020-06-17 13:00	2020-06-27 21:50	27.974	24.55	3.3×10^7	75.17
Port l'Hebert	2	2020-07-01 13:10	2020-07-04 15:50	25.113	23.83	5.7×10^6	12.33
Port l'Hebert	3	2020-07-09 17:10	2020-07-15 0:00	26.5	24.21	3.4×10^7	79.33
Port l'Hebert	4	2020-07-19 16:10	2020-08-24 20:30	28.568	24.23	1.1×10^8	245.17
Port Joli	1	2020-06-16 12:30	2020-06-27 21:15	28.32	24.41	1.9×10^7	53.5
Port Joli	2	2020-07-01 12:15	2020-07-04 16:45	25.258	24.13	2.9×10^6	7.25
Port Joli	3	2020-07-09 18:00	2020-07-14 22:00	27.186	24.08	2.7×10^7	76.75
Port Joli	4	2020-07-18 15:30	2020-08-24 20:00	29.59	24.47	9.6×10^7	258.5
Port Joli	5	2020-08-30 13:30	2020-09-01 16:30	23.857	23.49	2.1×10^6	5.25
Port Joli	6	2020-09-16 15:15	2020-09-17 17:00	26.158	23.99	9.6×10^5	2.25

Table 4. Underwater light conditions within seagrass beds at each field site. K_d = light attenuation coefficient (from both the water column and seagrass canopy), SD = standard deviation. PAR = µmol m^{-2} s^{-1}.

Site	Mean bottom PAR	SD bottom PAR	Max bottom PAR	Mean daily K_d (m^{-1})	SD daily K_d (m^{-1})	Median daily K_d (m^{-1})	Max K_d (m^{-1})
Mason's Island	92.35	160.83	1066.97	0.83	0.65	0.61	3.52
Port l'Hebert	173.53	292.05	2533.10	0.94	0.23	0.89	1.73
Port Joli	162.05	265.09	1747.46	1.37	0.52	1.22	4.07
Sacrifice Island	122.91	207.48	1227.02	0.56	0.54	0.34	2.87
Sambro	23.28	32.09	224.85	1.37	0.30	1.39	1.94
Taylor's Head	89.20	154.80	1116.67	0.48	0.12	0.45	0.91

Table 5. Turbidity within seagrass beds at each field site. Tu = turbidity, SD = standard deviation.

Site	Mean daily Tu (NTU)	SD daily Tu (NTU)	Max Tu (NTU)	Median daily Tu (NTU)	Median daily Tu (mg L^{-1})*
Mason's Island	4.21	5.31	40.09	2.97	8.30
Port l'Hebert	9.14	15.61	86.37	3.45	11.4
Port Joli	9.60	9.17	47.17	6.41	25.6
Sacrifice Island	2.99	2.23	13.32	2.25	9.09
Sambro	1.95	1.06	6.23	1.48	14.9
Taylor's Head	11.51	13.78	76.55	6.25	42.9

*from calibration relationships.

Table 6. Current speed within seagrass beds at each field site. SD = standard deviation.

Site	Mean current speed (cm s^{-1})	SD current speed (cm s^{-1})	Max current speed (cm s^{-1})	Min current speed (cm s^{-1})	Median current speed (cm s^{-1})
Mason's Island	1.30	1.86	19.73	0.13	0.69
Port l'Hebert	4.68	2.42	9.98	0.20	4.71
Port Joli	5.09	2.29	10.00	0.30	5.07
Sacrifice Island	2.12	1.64	21.20	0.31	1.67
Sambro	2.41	1.53	9.74	0.67	1.87
Taylor's Head	9.25	3.60	17.13	1.67	9.41

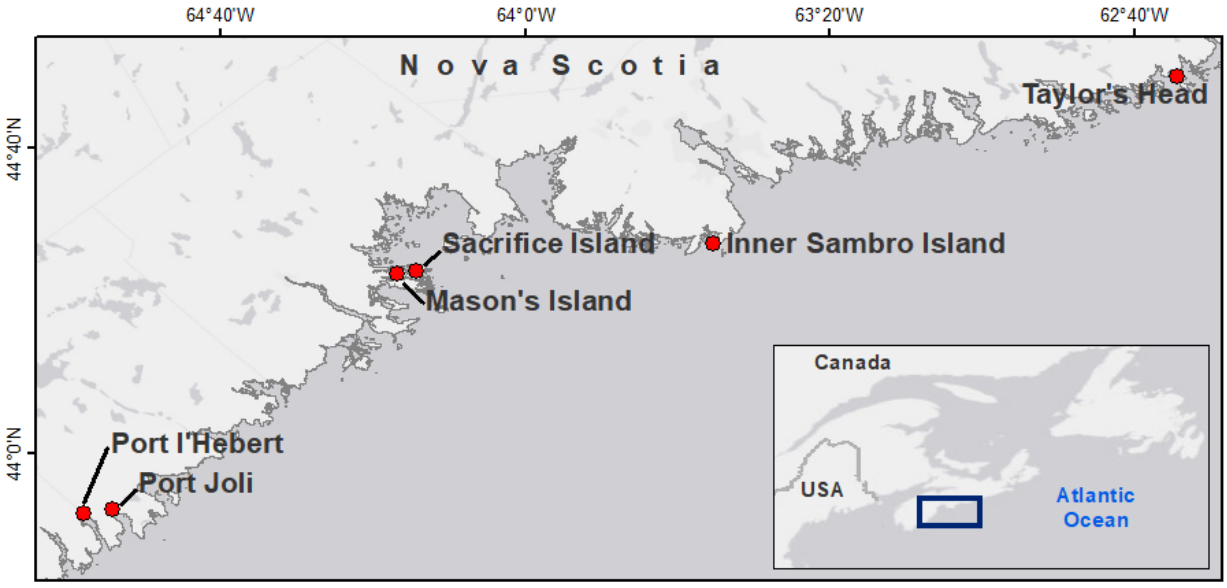

Figure 1. Map of field sites on the Atlantic coast of Nova Scotia where physical processes were measured in seagrass beds.

FIGURES

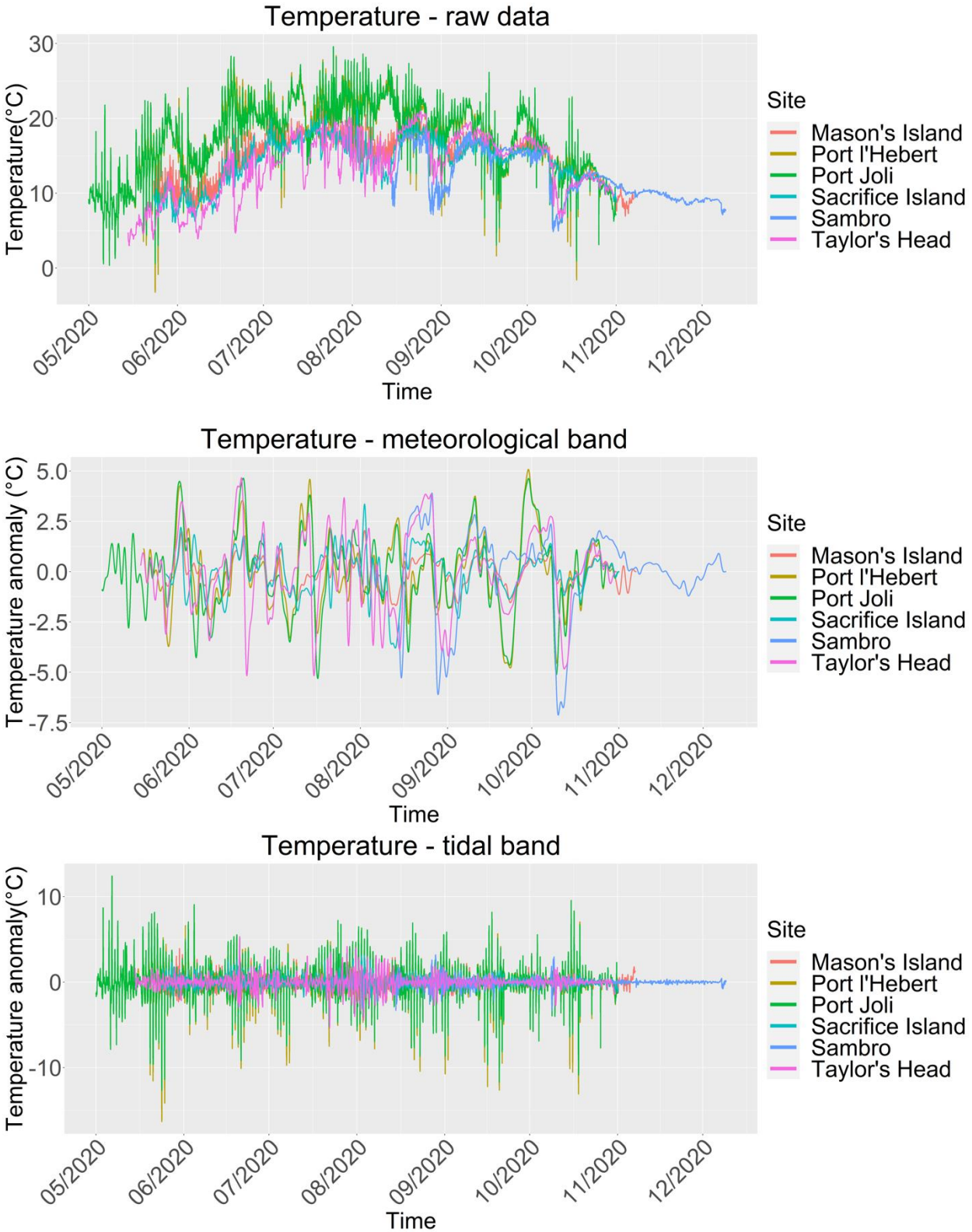

Figure 2. Temperature frequencies across all field sites. Raw data (top panel), meteorological band (48h to ~60 days; middle panel), and tidal band (<48h; bottom panel).

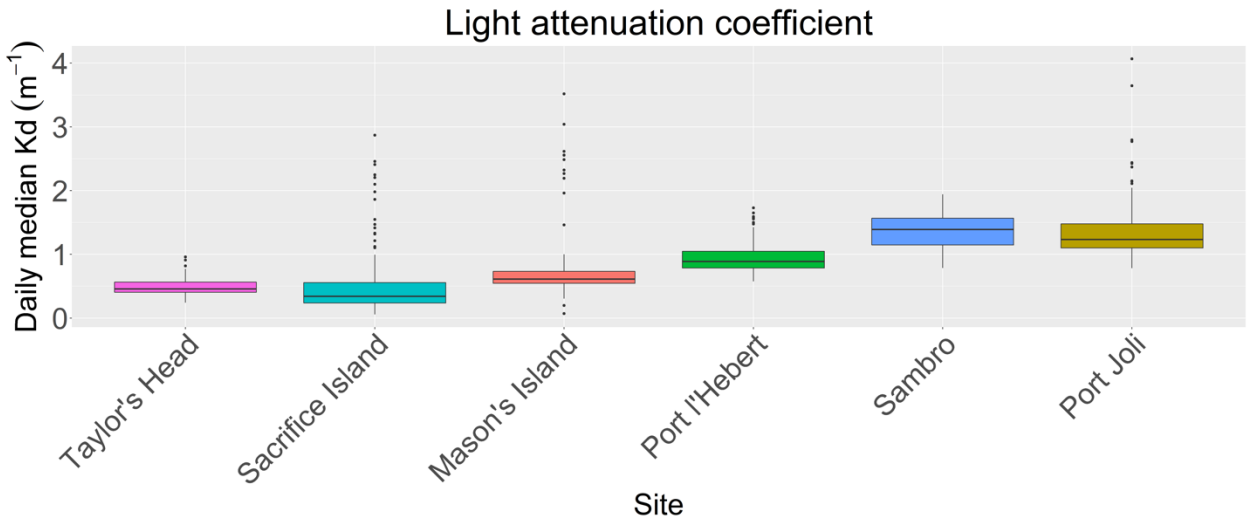

Figure 3. Boxplots of daily median light attenuation coefficient (K_d) within seagrass beds at the field sites. Note that the sensors for Sambro were likely fouled or buried for much of the record.

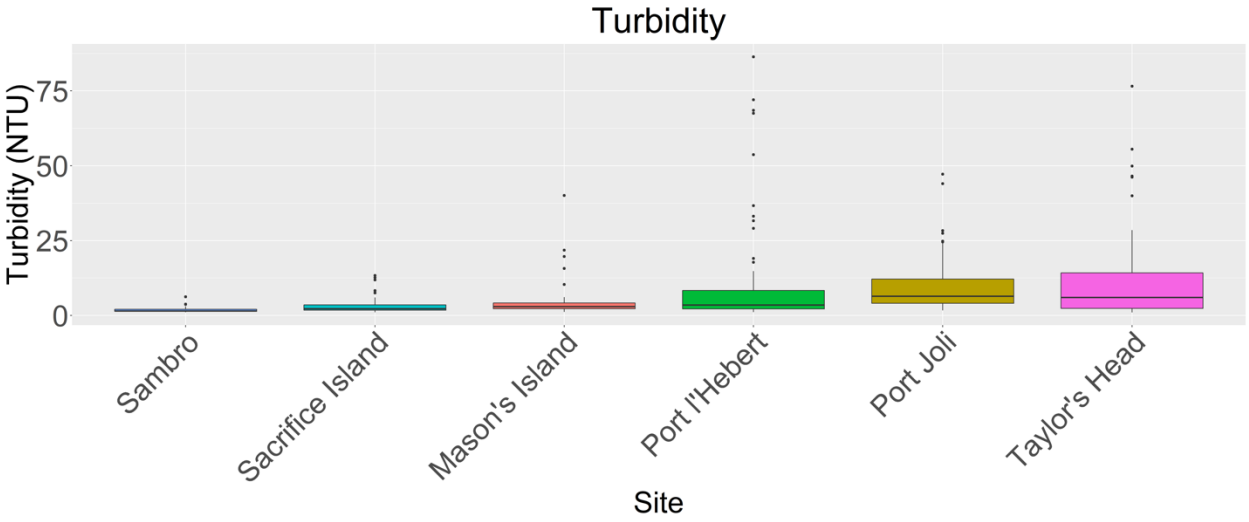

Figure 4. Boxplots of daily median turbidity within seagrass beds at the field sites. Note that the sensors for Sambro were likely fouled or buried for much of the record.

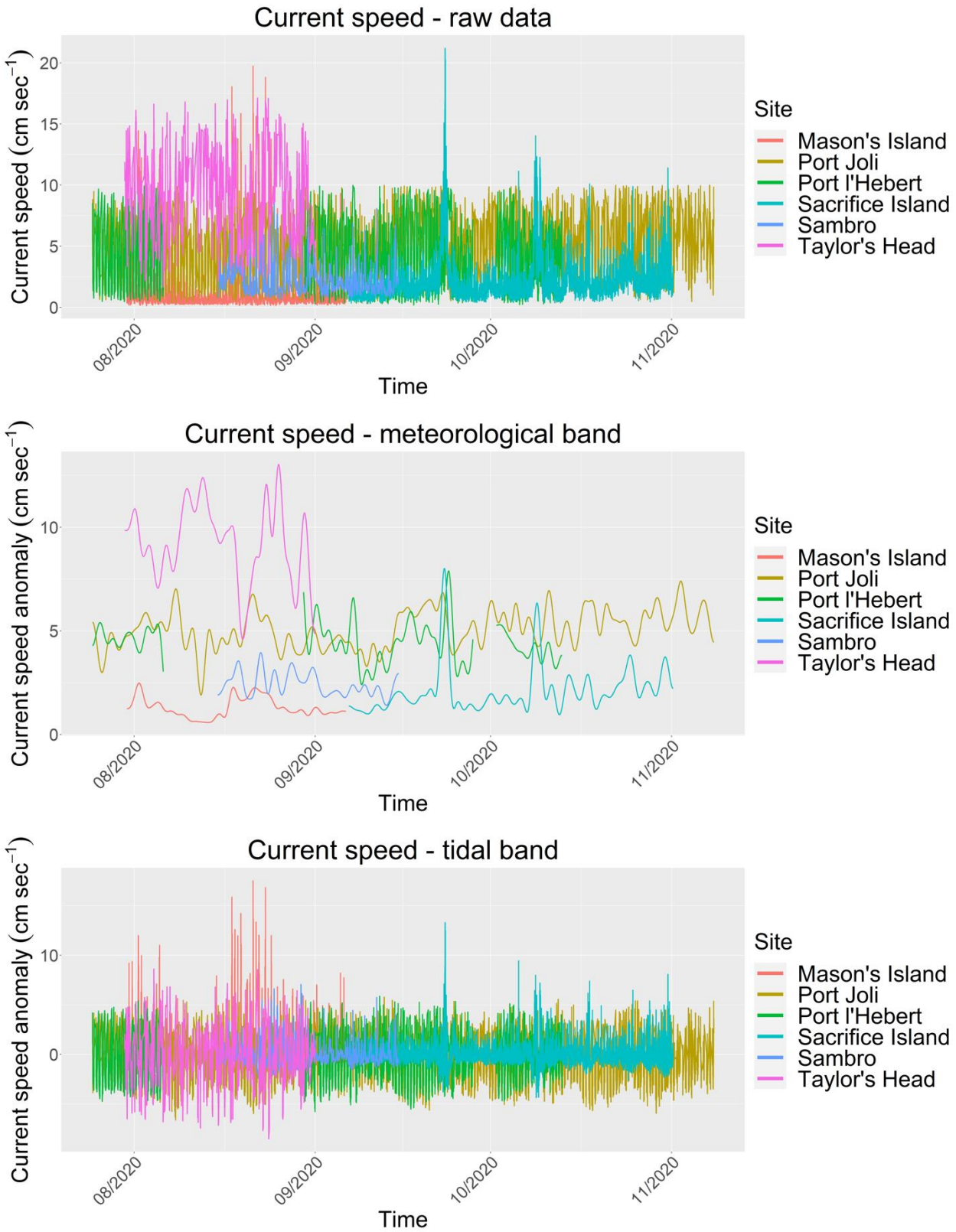

Figure 5. Current speed frequencies across all field sites. Raw data (top panel), meteorological band (48h to ~60 days; middle panel), and tidal band (<48h; bottom panel).

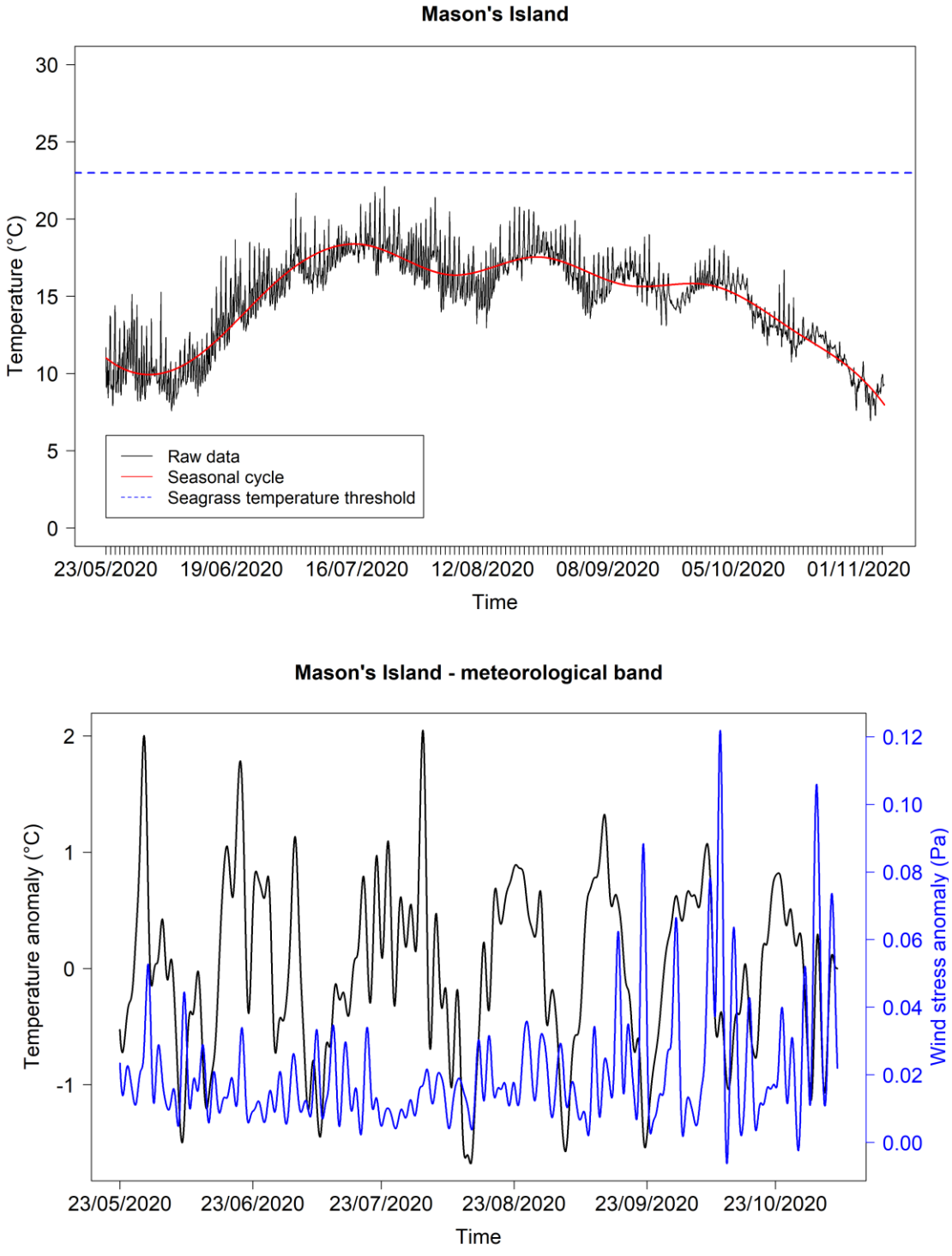

Figure 6a. Temperature record from Mason's Island. Raw temperature (top panel) with overlaid seasonal signal and dotted line indicating 23°C (optimal photosynthetic temperature for *Z. marina*). The meteorological band (bottom panel) is overlaid with the same band of wind stress.

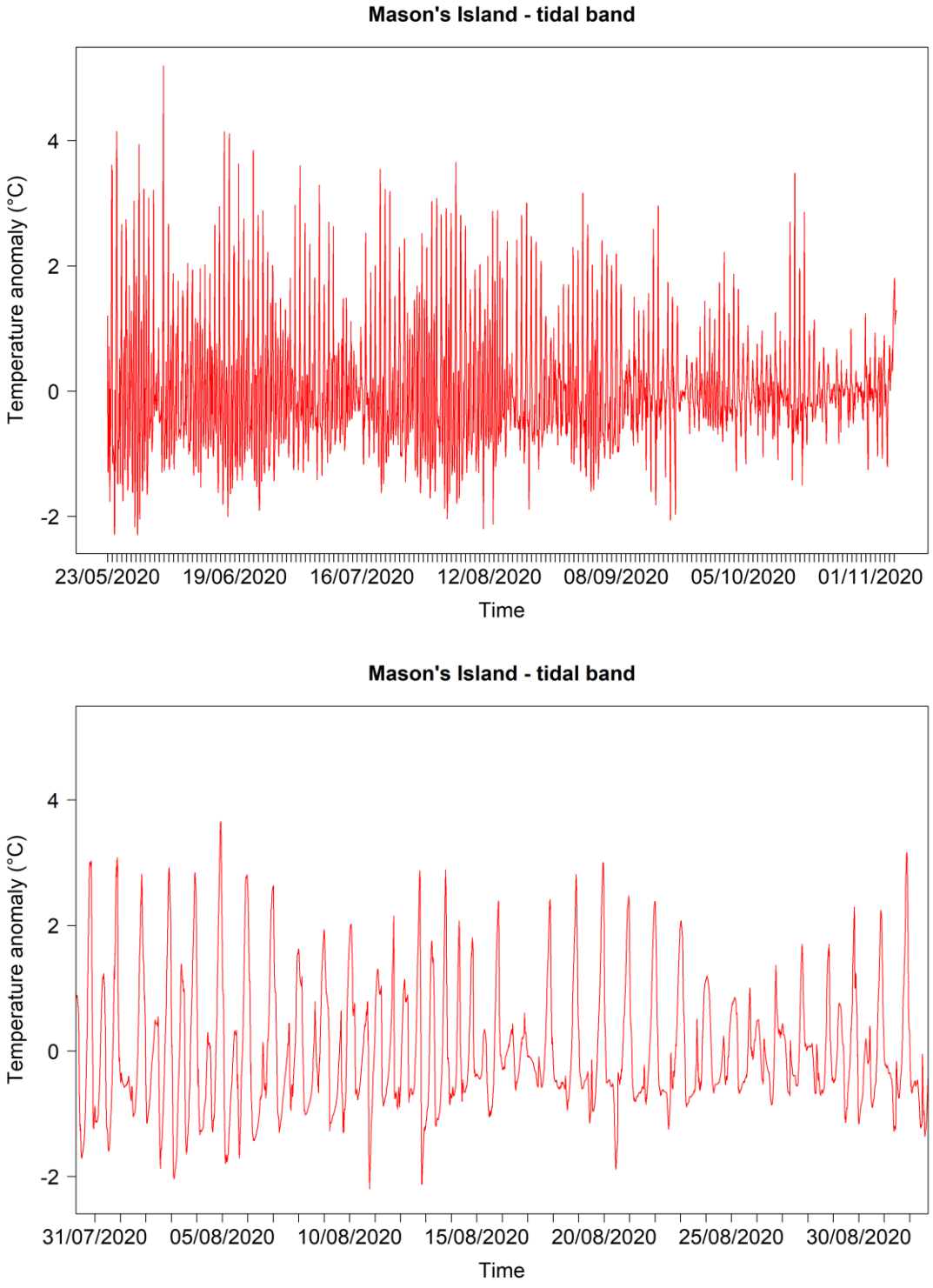

Figure 6b. Tidal band of the full temperature record (top) and an isolated period (bottom) at Mason's Island.

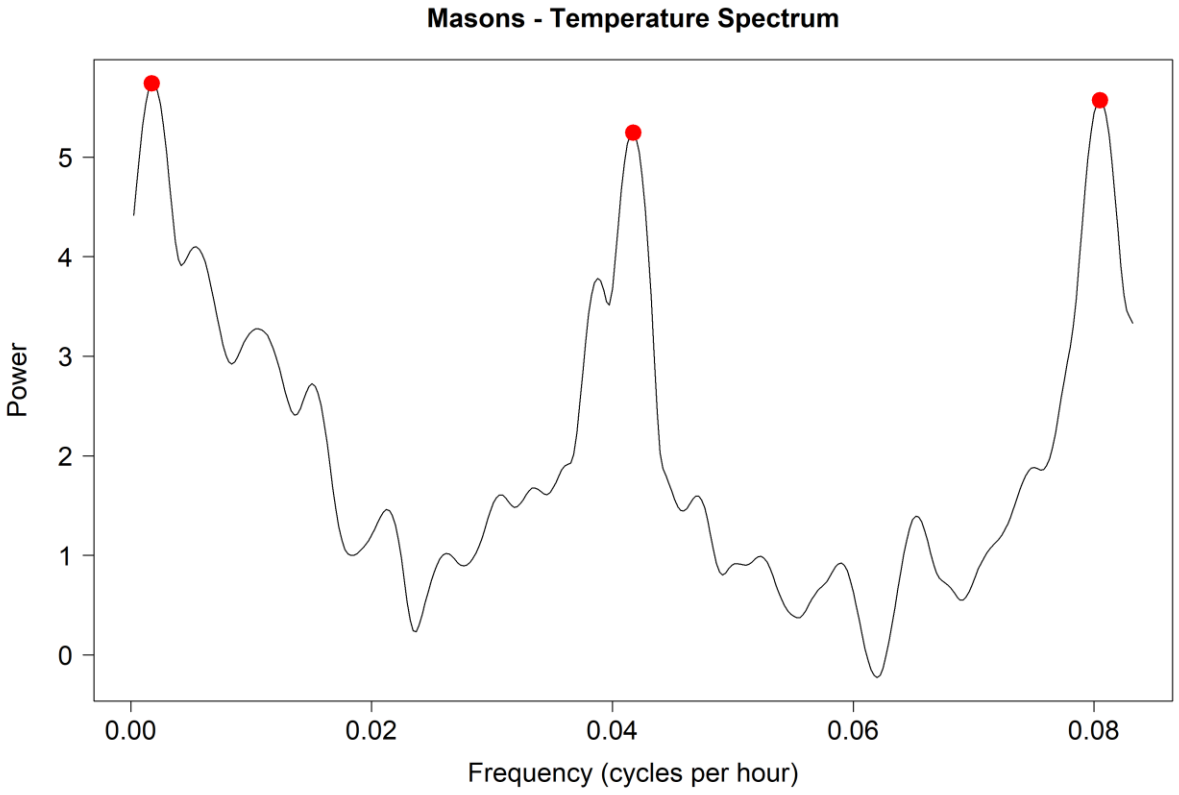

Figure 6c. Power spectrum (log) showing dominant frequencies at 24 days, 0.998 days (23.96h), and 0.517 days (12.42h), representing temperature variability related to coastal upwelling, daily/solar tides, and M2 twice daily tides, respectively.

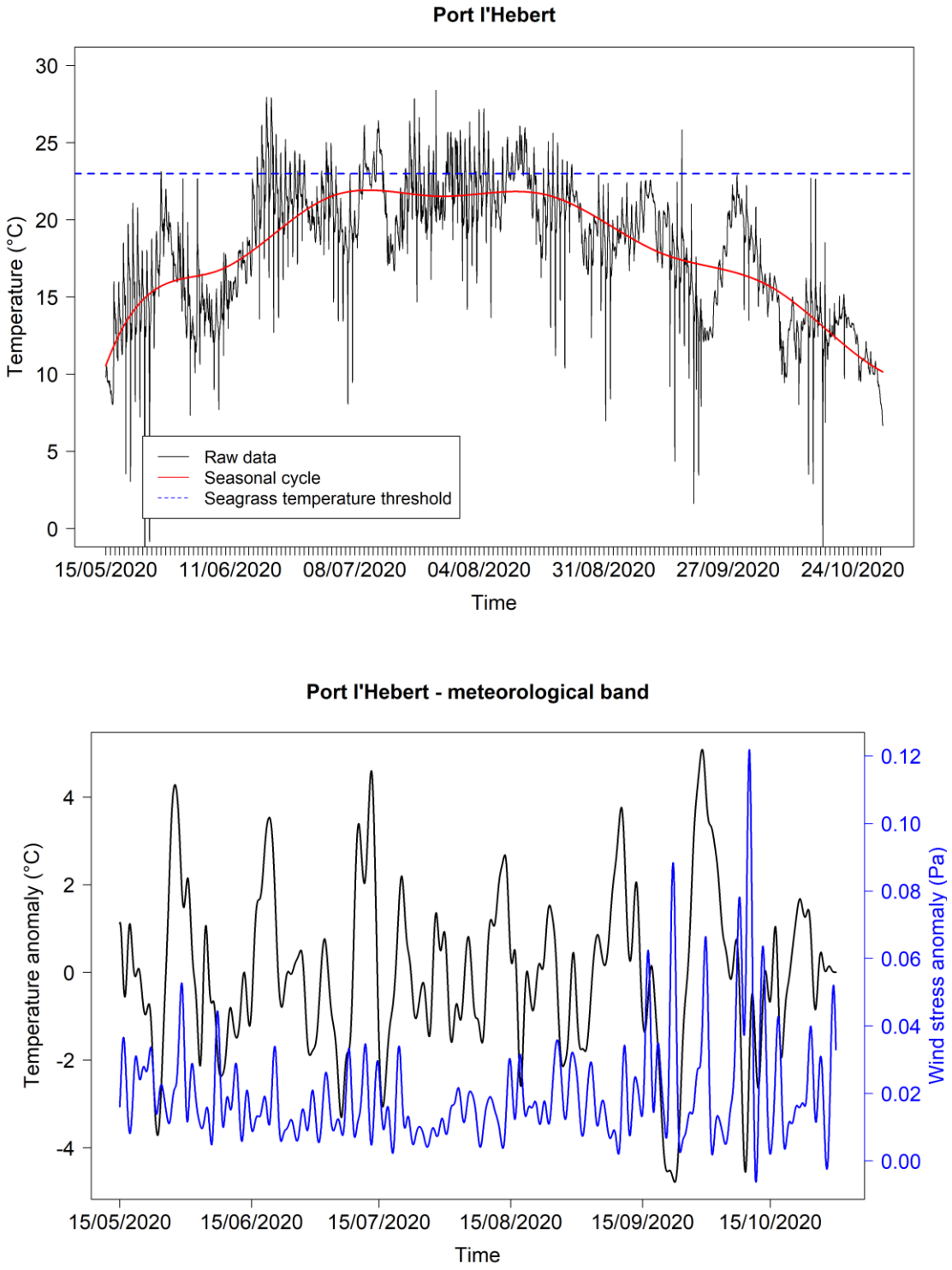

Figure 7a. Temperature record from Port l'Hebert. Raw temperature (top panel) with overlaid seasonal signal and dotted line indicating 23°C (optimal photosynthetic temperature for *Z. marina*). The meteorological band (bottom panel) is overlaid with the same band of wind stress.

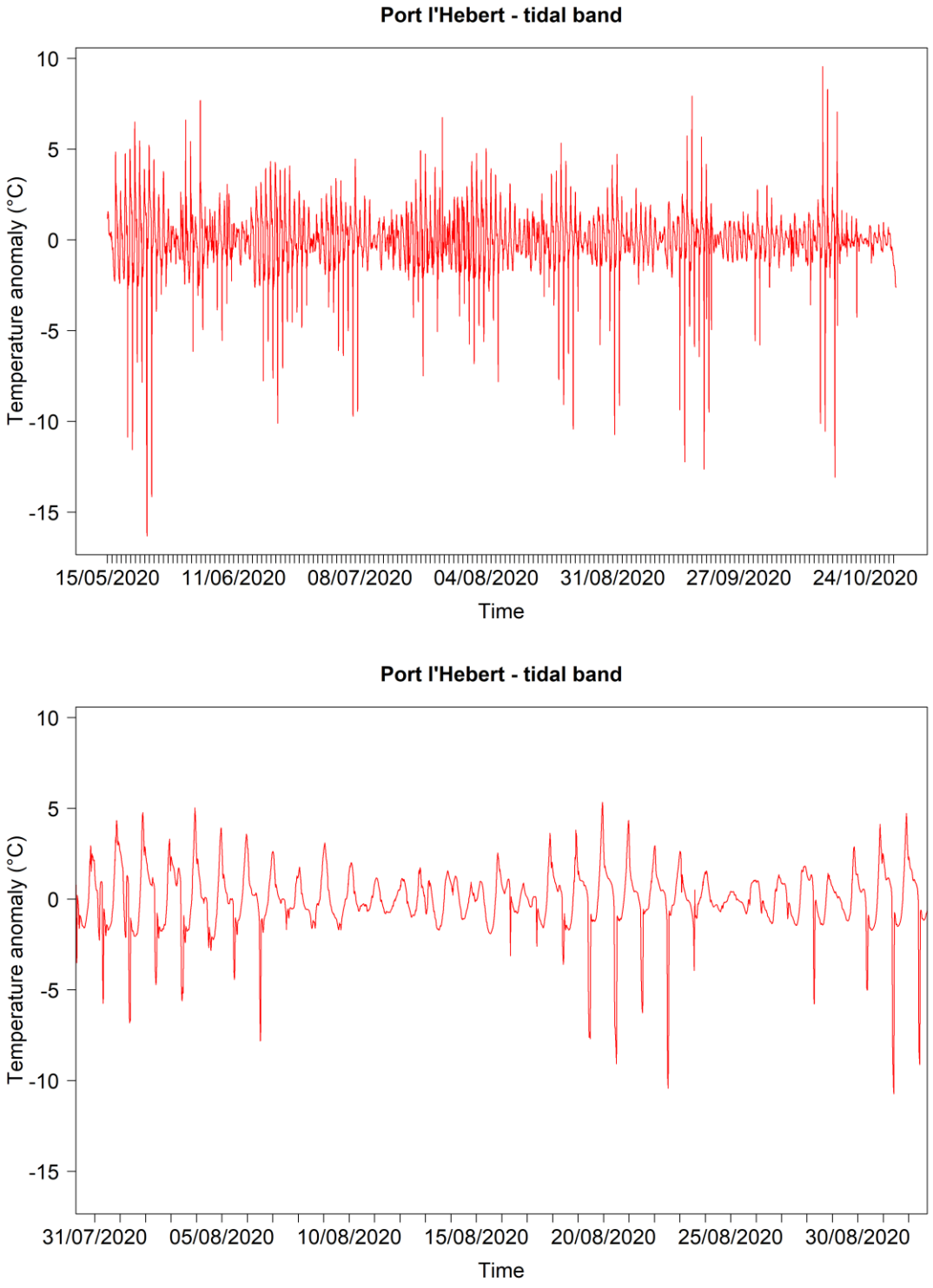

Figure 7b. Tidal band of the full temperature record (top) and an isolated period (bottom) at Port l'Hebert.

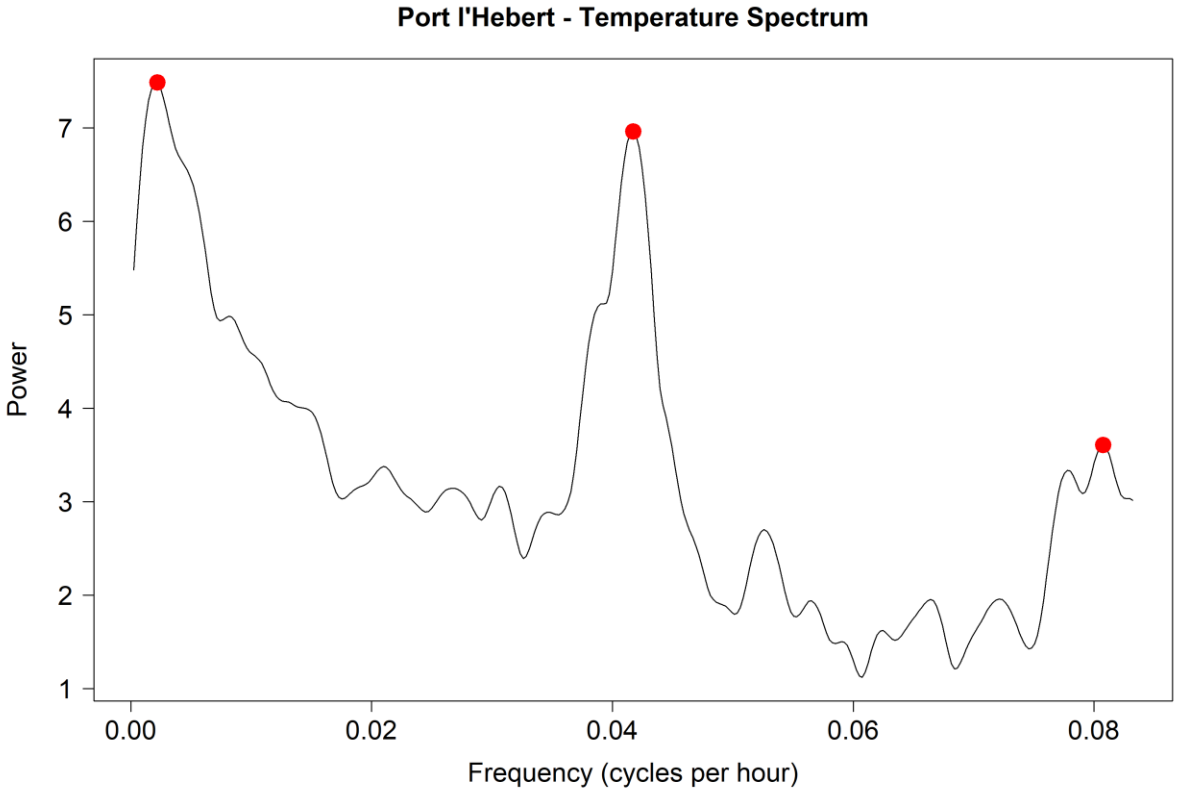

Figure 7c. Power spectrum (log) showing dominant frequencies at 18.75 days, 0.998 days (23.96h), and 0.516 days (12.39h), representing temperature variability related to coastal upwelling, daily/solar tides, and M2 twice daily tides, respectively.

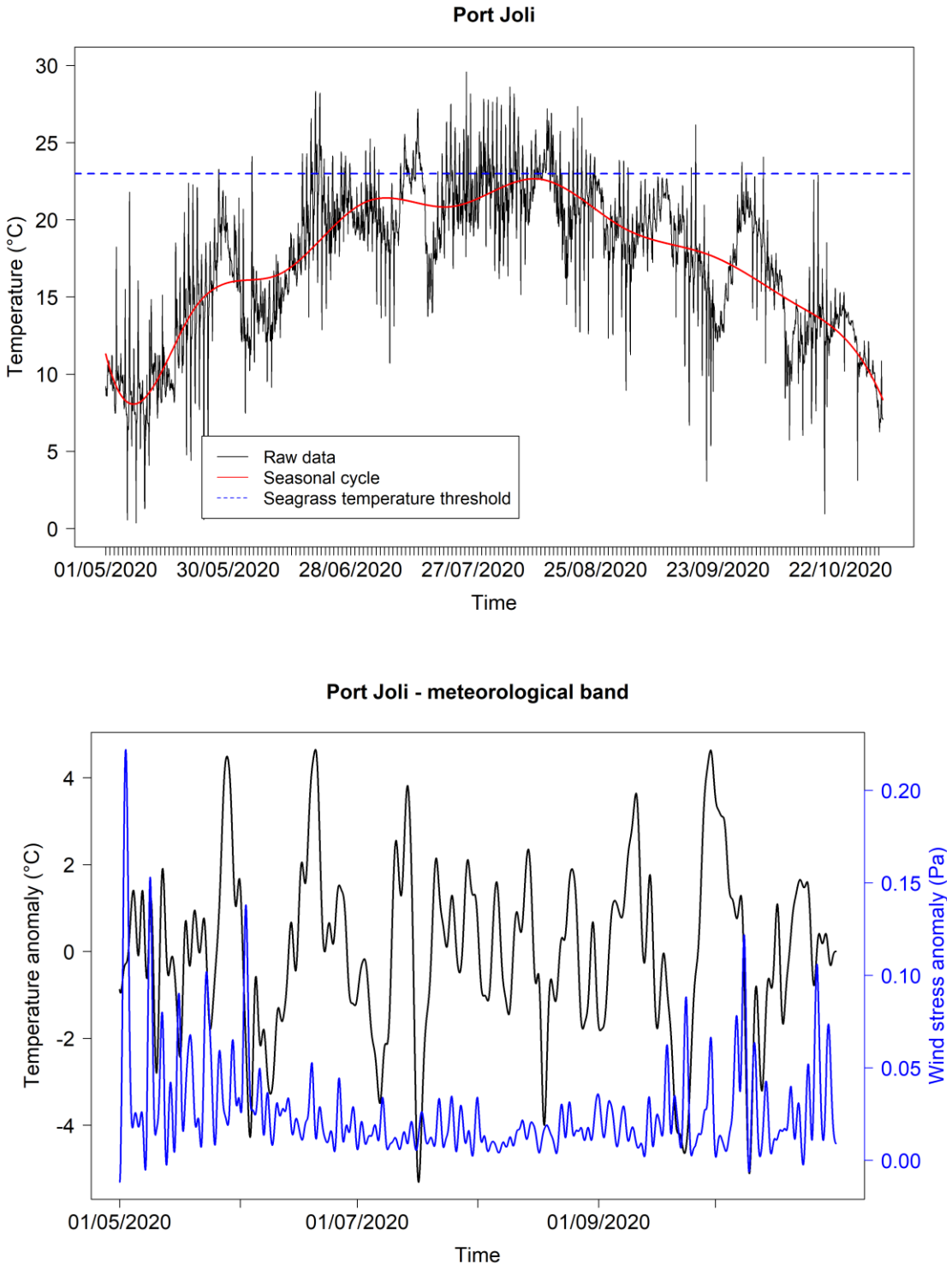

Figure 8a. Temperature record from Port Joli. Raw temperature (top panel) with overlaid seasonal signal and dotted line indicating 23°C (optimal photosynthetic temperature for *Z. marina*). The meteorological band (bottom panel) is overlaid with the same band of wind stress.

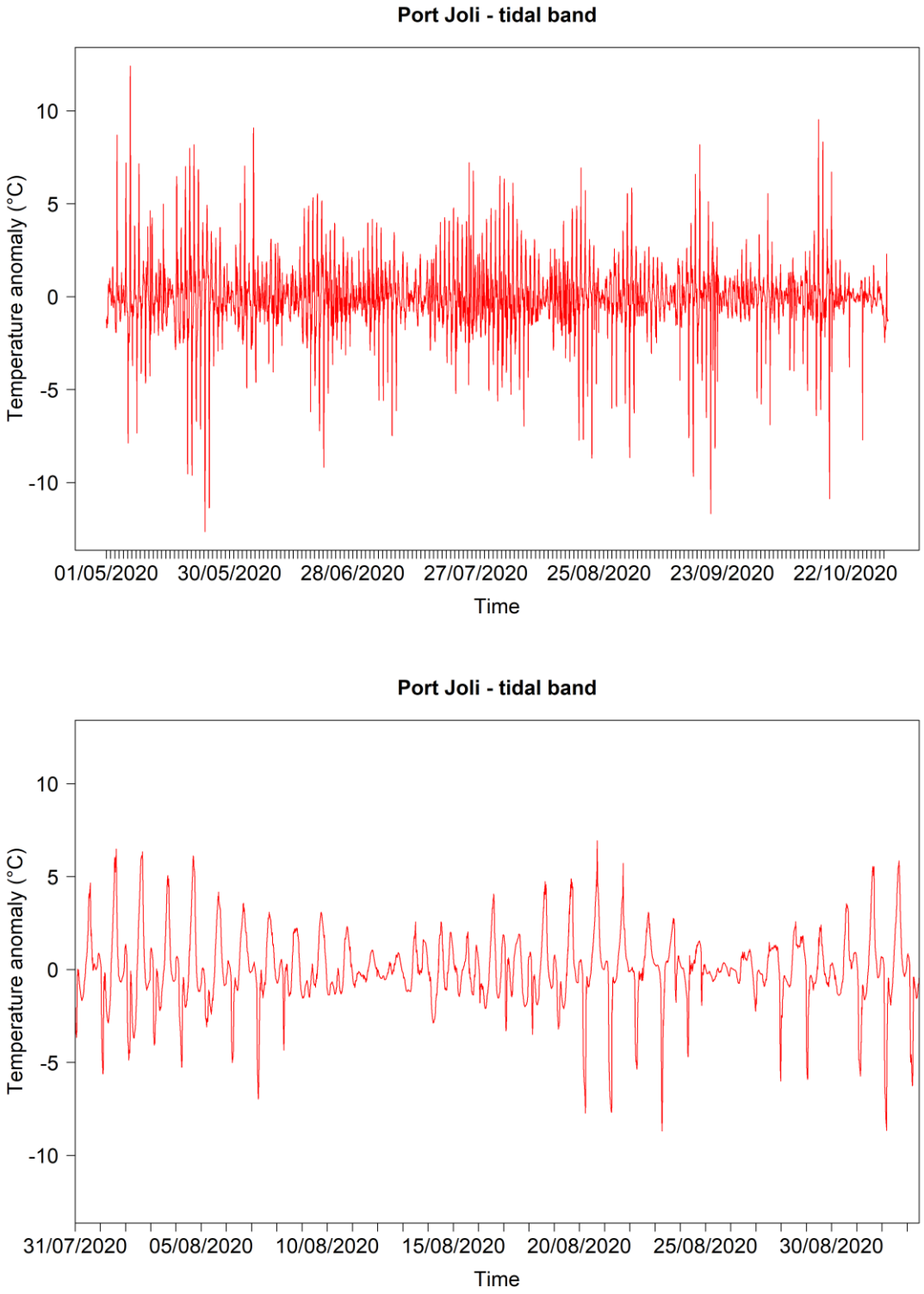

Figure 8b. Tidal band of the full temperature record (top) and an isolated period (bottom) at Port Joli.

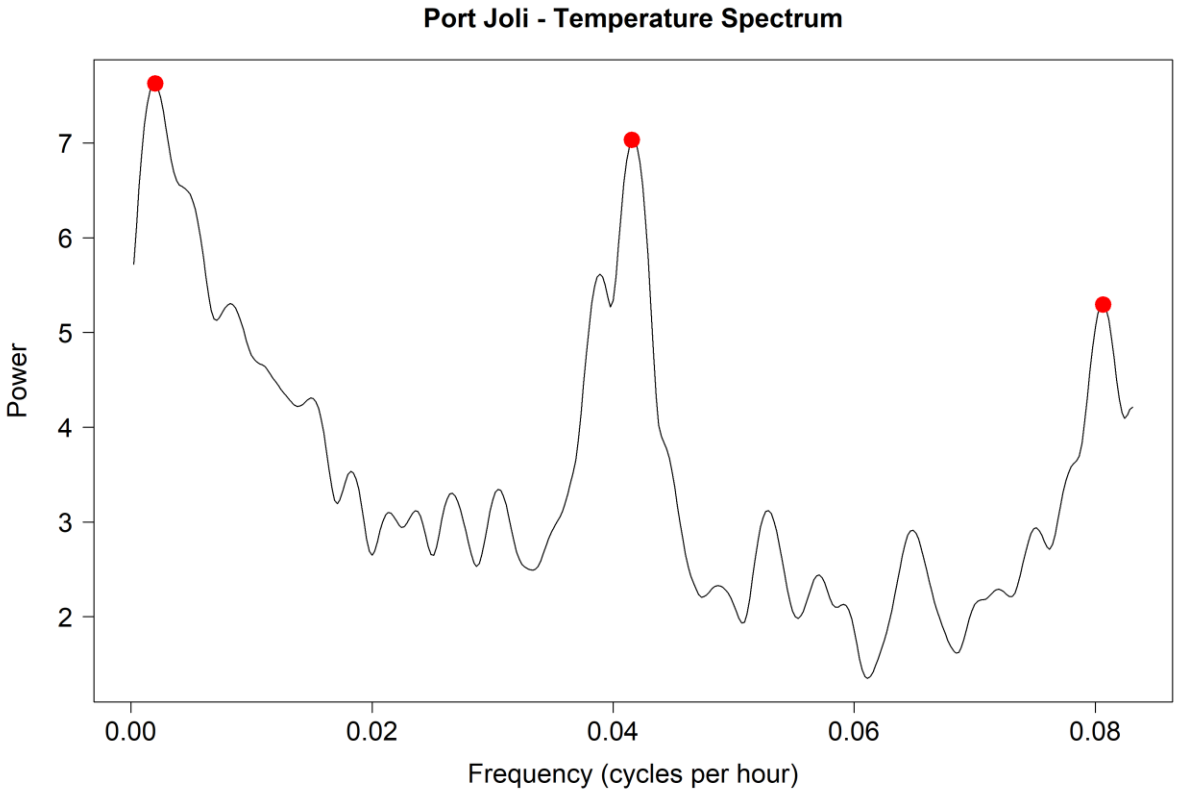

Figure 8c. Power spectrum (log) showing dominant frequencies at 20.8 days, 1 days (24h), and 0.516 days (12.39h), representing temperature variability related to coastal upwelling, daily/solar tides, and M2 twice daily tides, respectively.

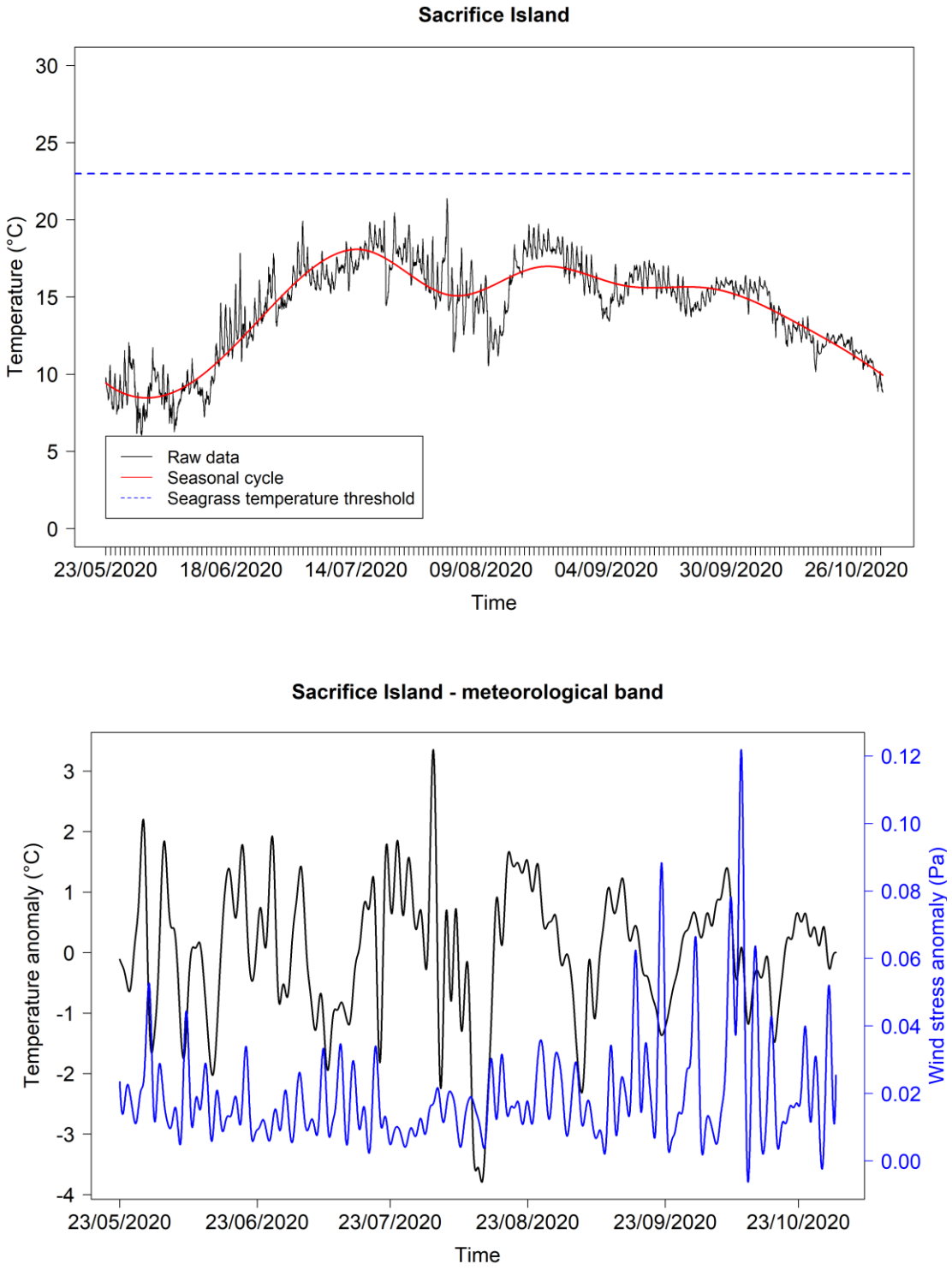

Figure 9a. Temperature record from Sacrifice Island. Raw temperature (top panel) with overlaid seasonal signal and dotted line indicating 23°C (optimal photosynthetic temperature for *Z. marina*). The meteorological band (bottom panel) is overlaid with the same band of wind stress.

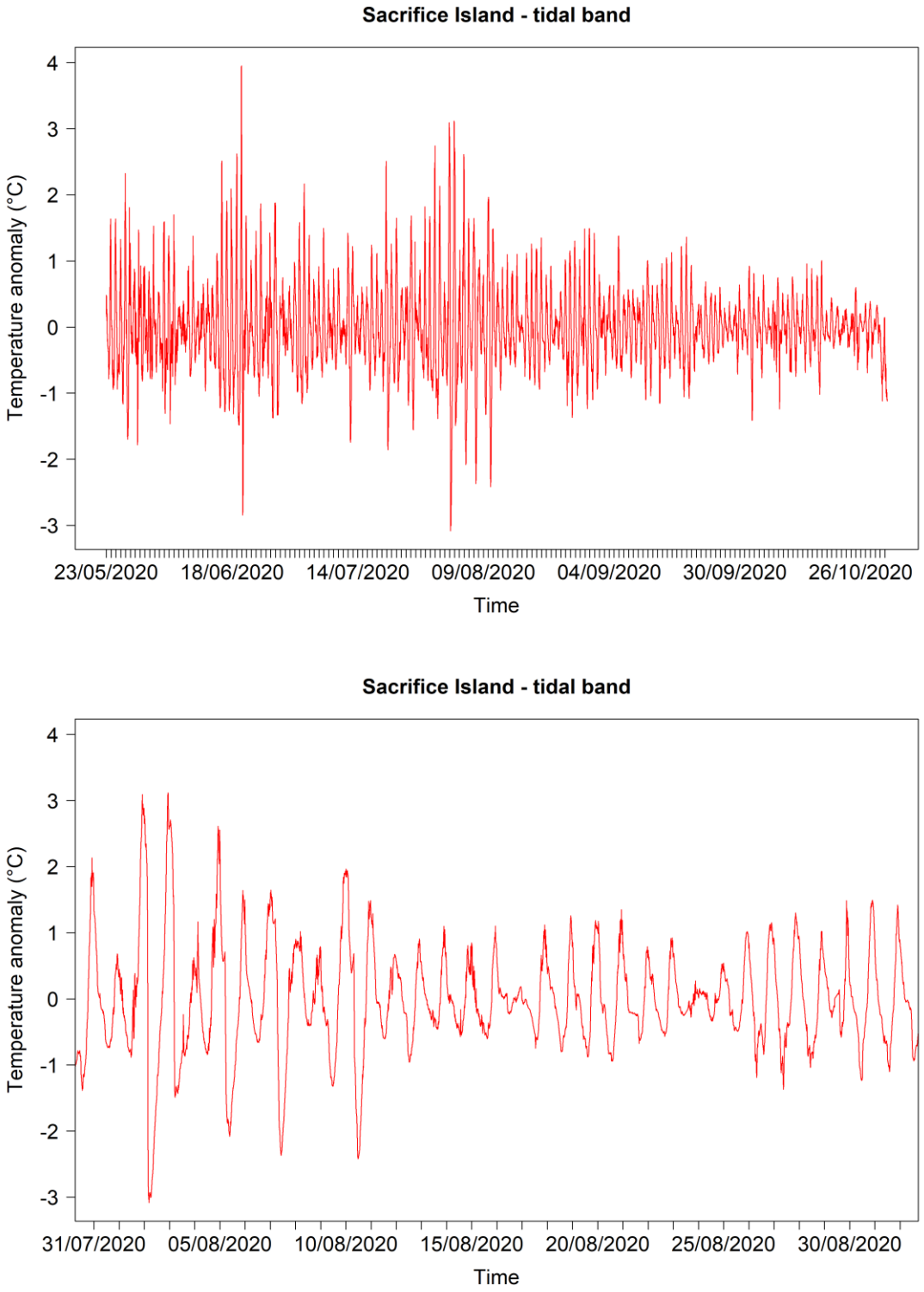

Figure 9b. Tidal band of the full temperature record (top) and an isolated period (bottom) at Sacrifice Island.

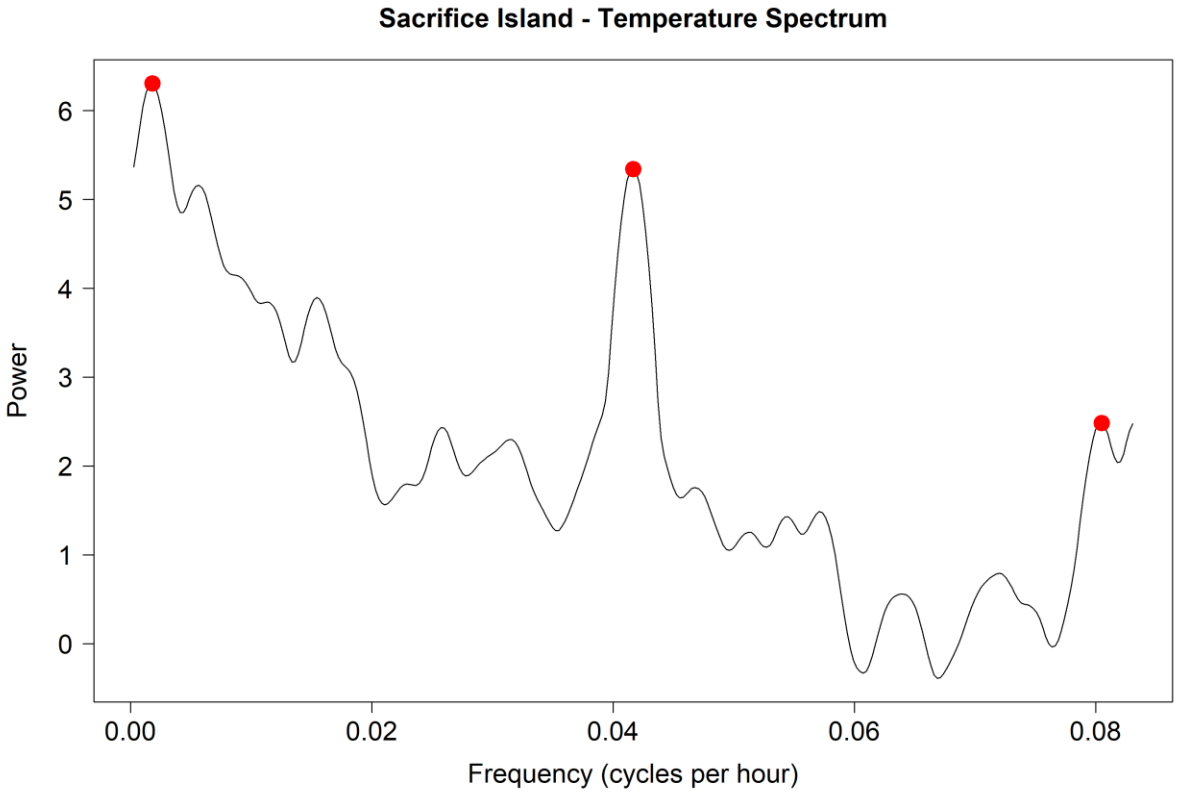

Figure 9c. Power spectrum (log) showing dominant frequencies at 23.1 days, 1 day (24h), and 0.517 days (12.42h), representing temperature variability related to coastal upwelling, daily/solar tides, and M2 twice daily tides, respectively.

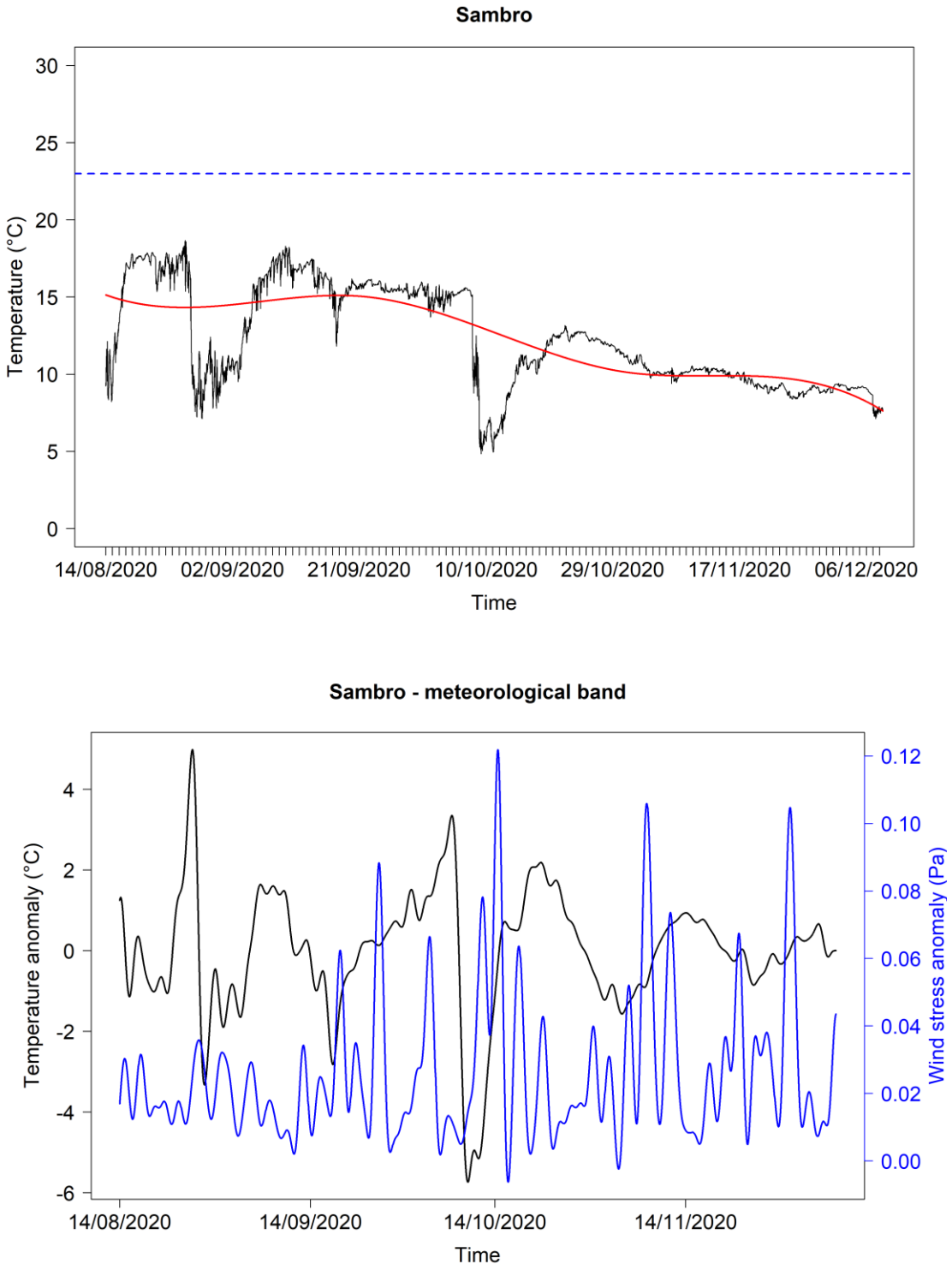

Figure 10a. Temperature record from Sambro. Raw temperature (top panel) with overlaid seasonal signal and dotted line indicating 23°C (optimal photosynthetic temperature for *Z. marina*). The meteorological band (bottom panel) is overlaid with the same band of wind stress.

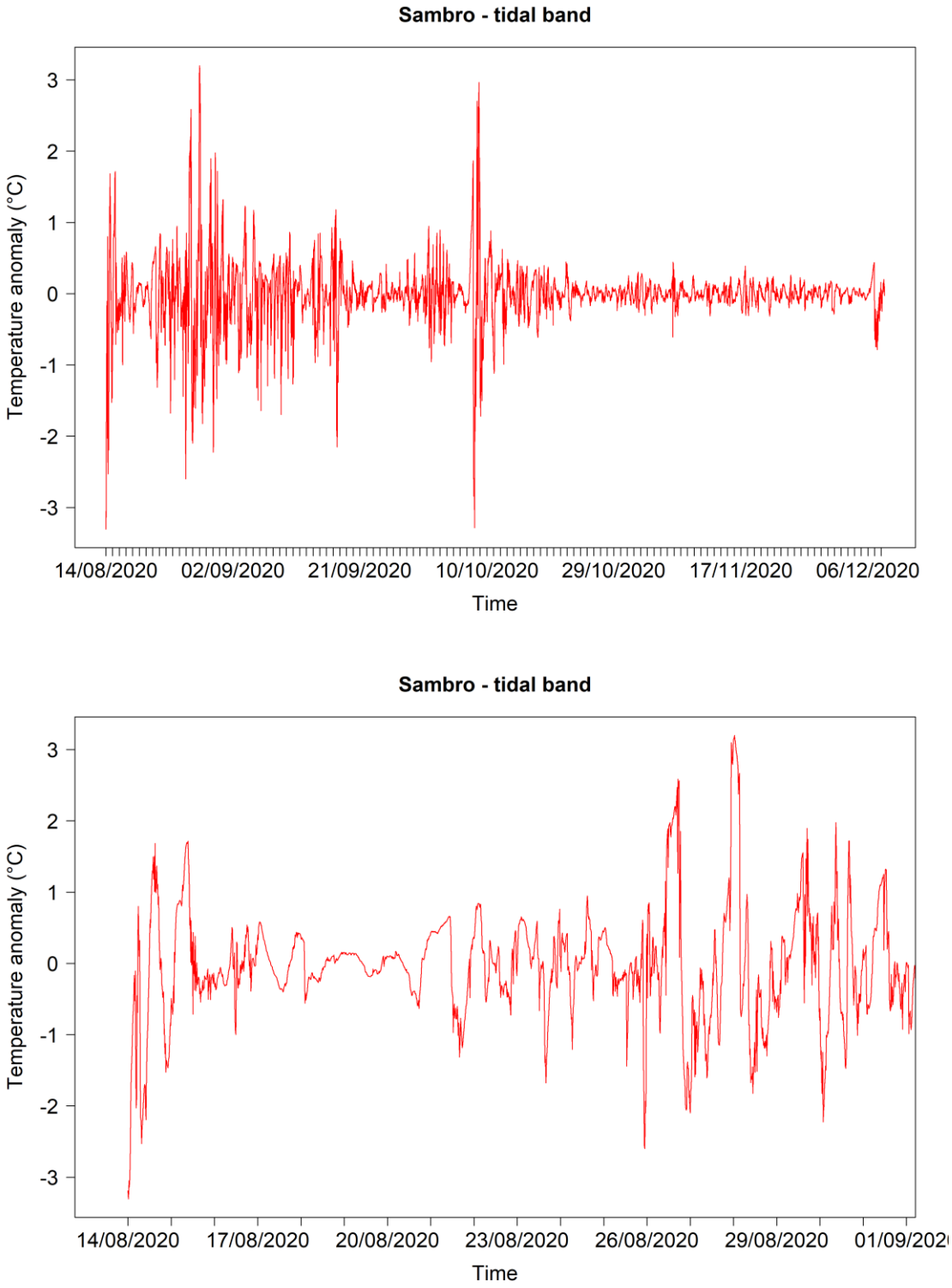

Figure 10b. Tidal band of the full temperature record (top) and an isolated period (bottom) at Sambro.

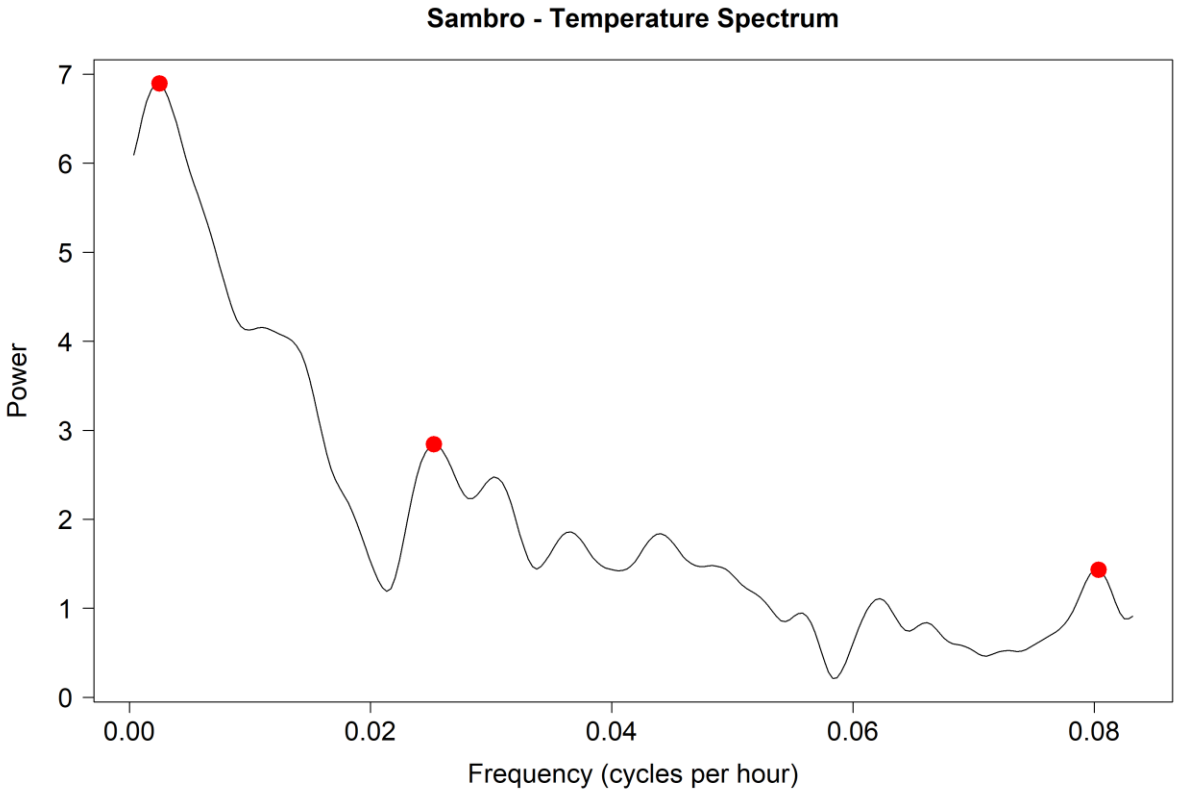

Figure 10c. Power spectrum (log) showing dominant frequencies at 16.7 days, 1.65 days (39.6h), and 0.518 days (12.44h), representing temperature variability related to coastal upwelling, daily/solar tides, and M2 twice daily tides, respectively.

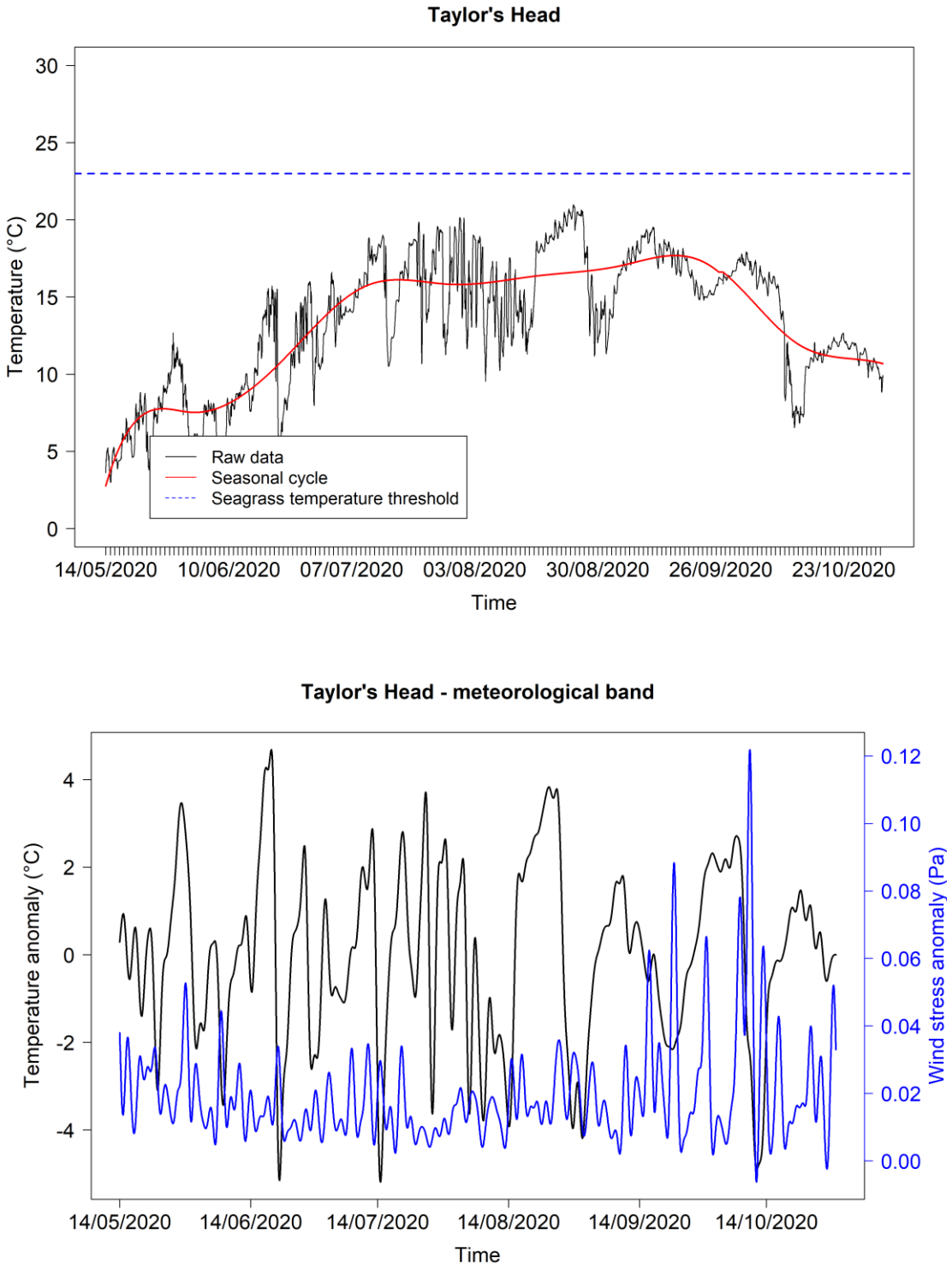

Figure 11a. Temperature record from Taylor's Head. Raw temperature (top panel) with overlaid seasonal signal and dotted line indicating 23°C (optimal photosynthetic temperature for *Z. marina*). The meteorological band (bottom panel) is overlaid with the same band of wind stress.

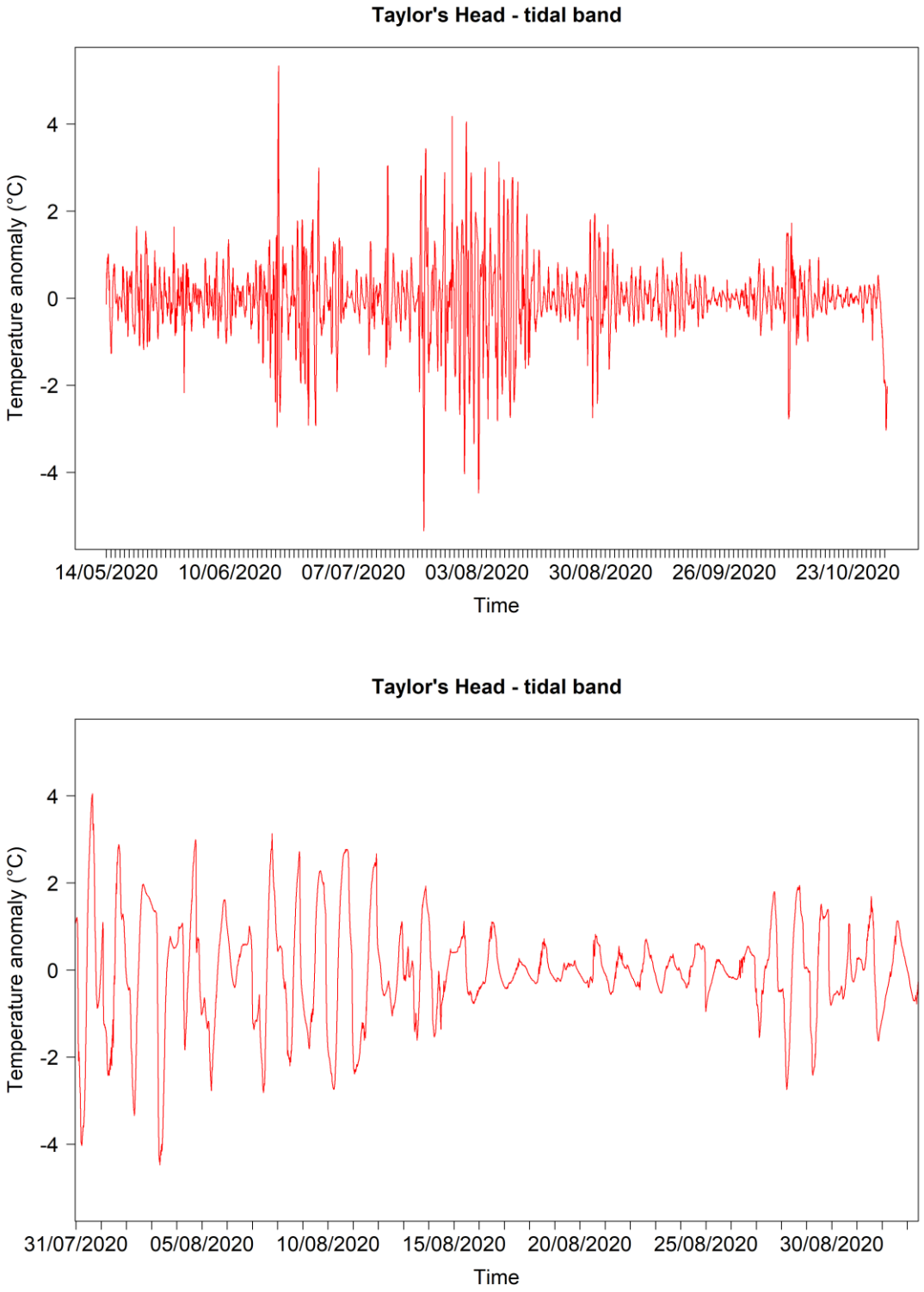

Figure 11b. Tidal band of the full temperature record (top) and an isolated period (bottom) at Taylor's Head.

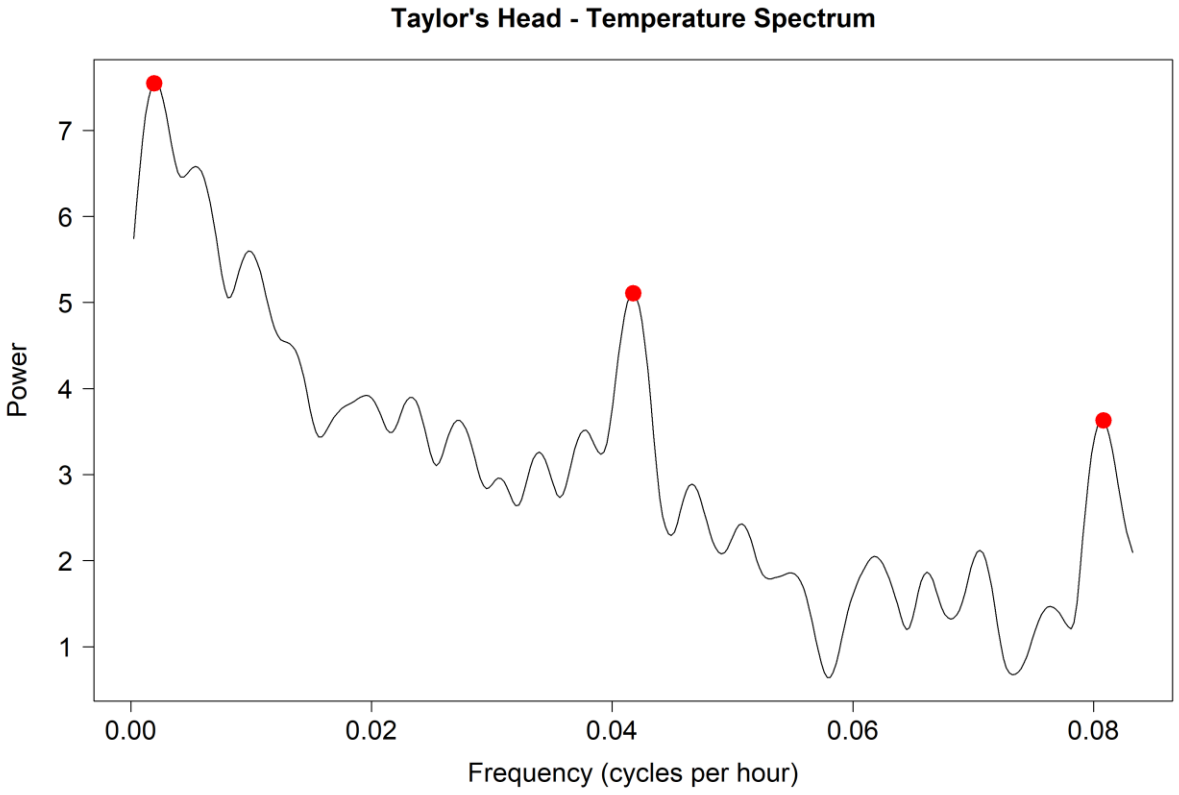

Figure 11c. Power spectrum (log) showing dominant frequencies at 21.3 days, 0.998 days (23.95h), and 0.515 days (12.37h), representing temperature variability related to coastal upwelling, daily/solar tides, and M2 twice daily tides, respectively.

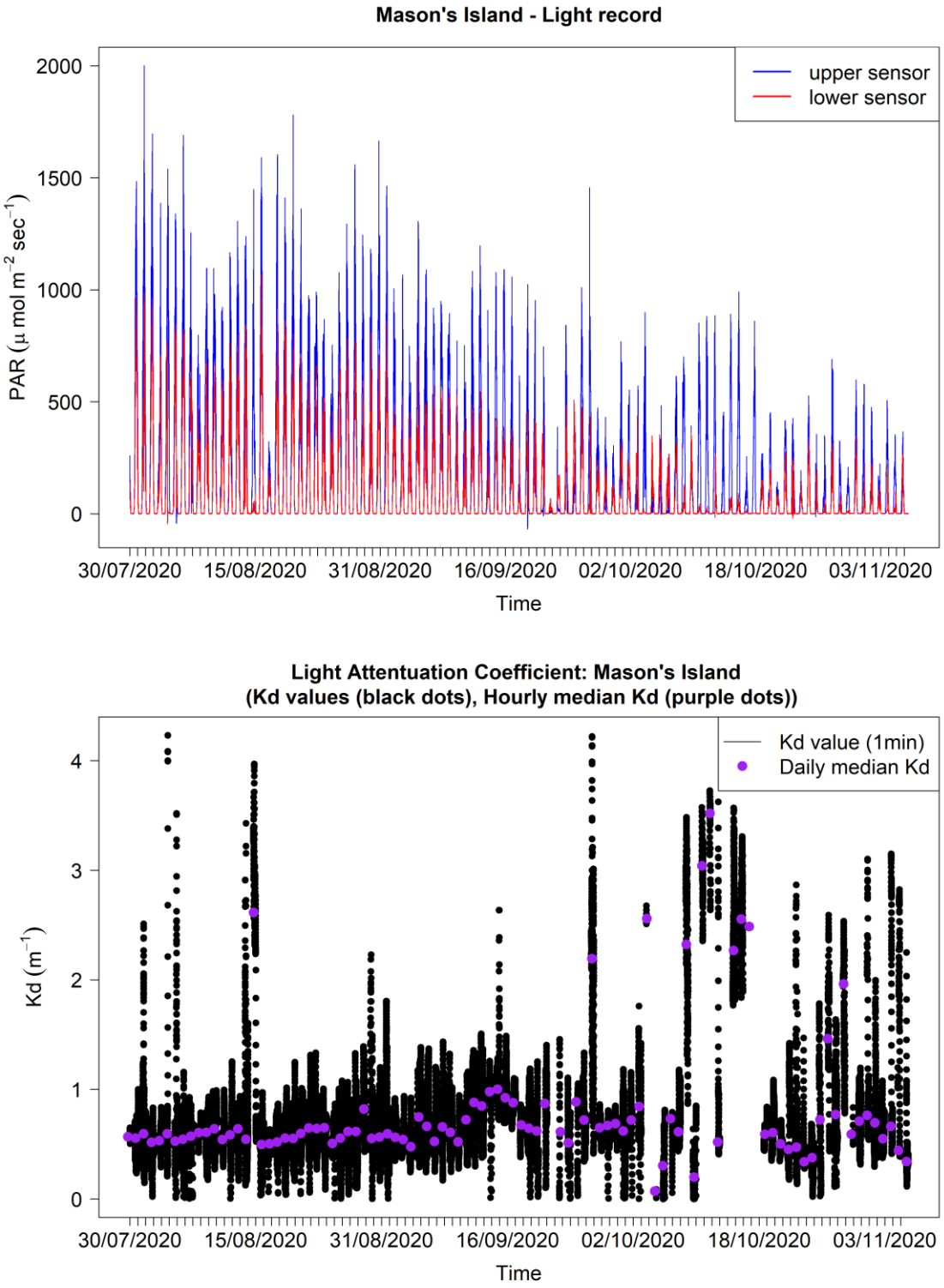

Figure 12a. Light conditions at Mason's Island. PAR data from sensors deployed in the water column (top panel) were used to calculate the light attenuation coefficient (bottom panel).

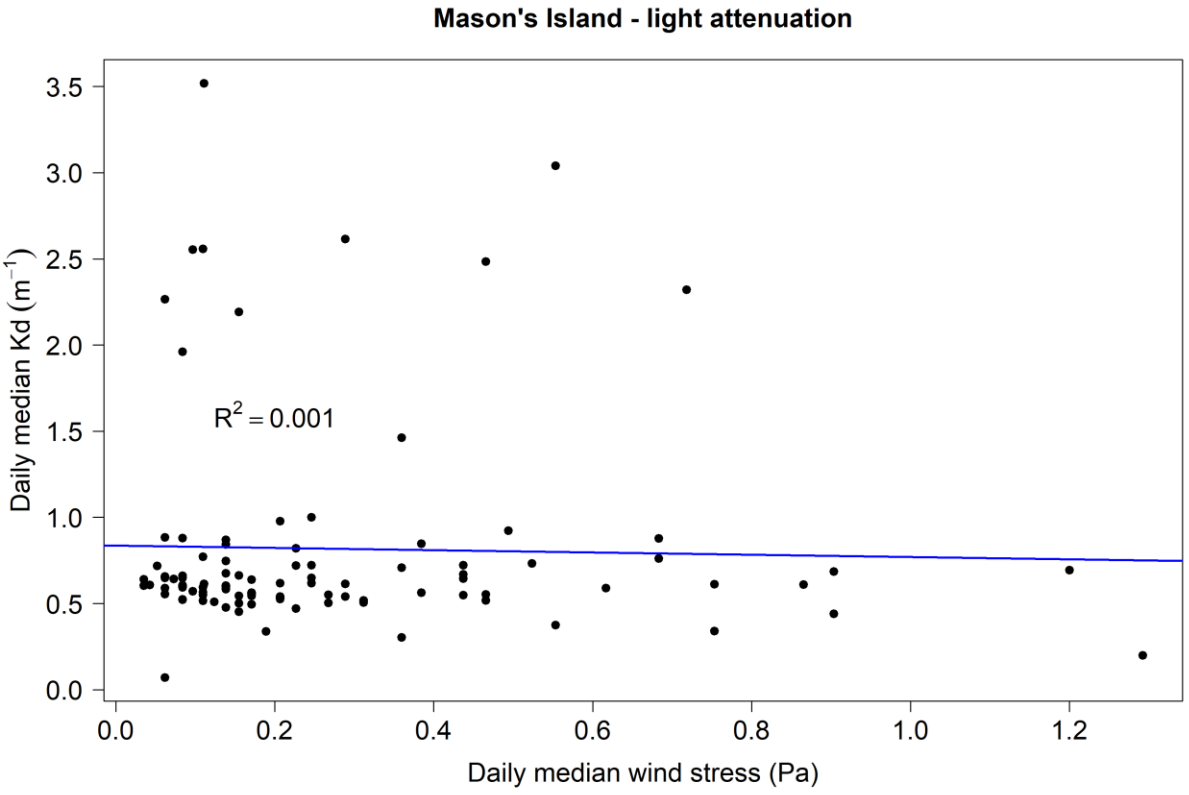

Figure 12b. Relationship between the daily median light attenuation coefficient (Kd) and daily median wind stress (Pa x 10^1).

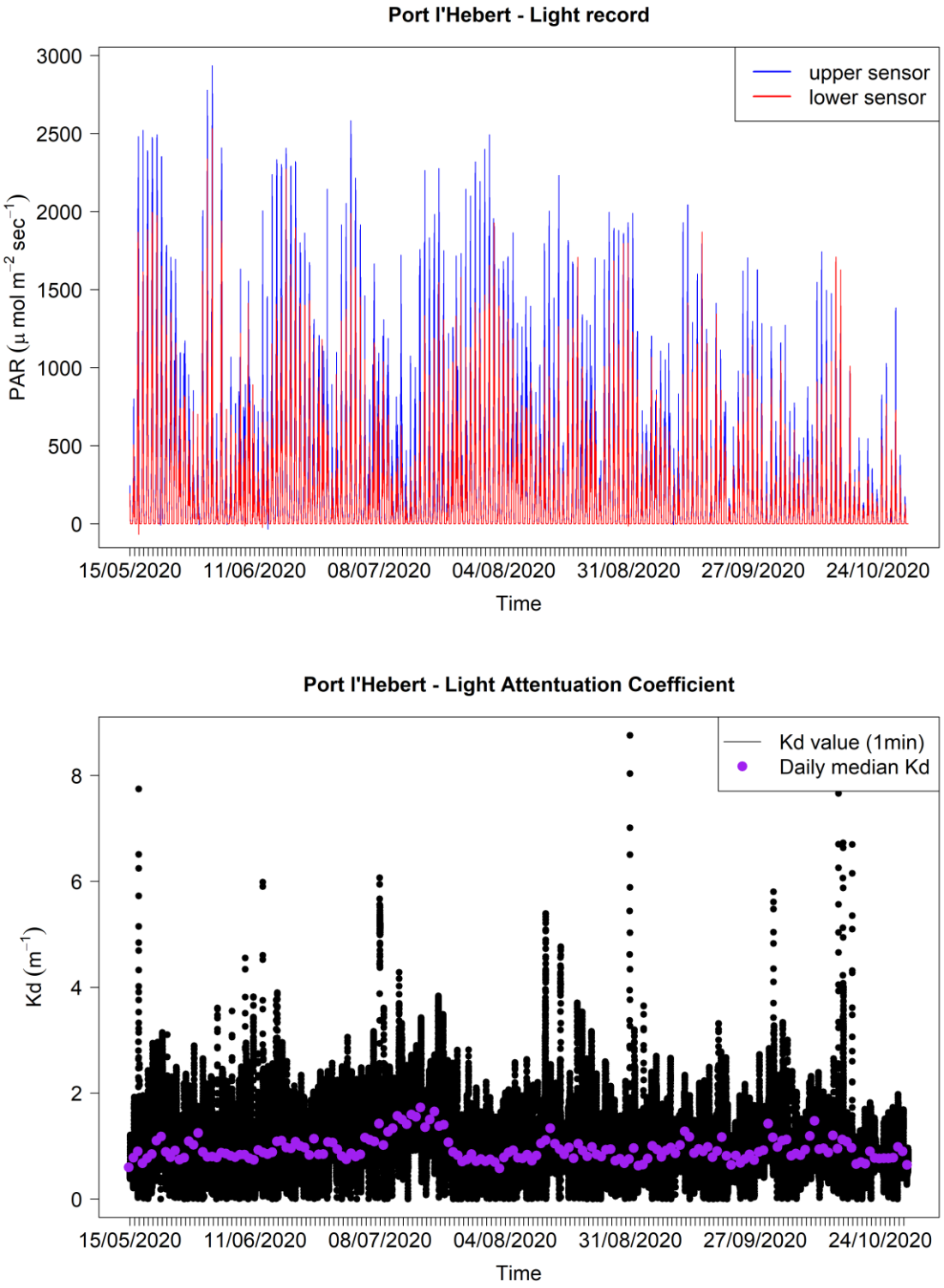

Figure 13a. Light conditions at Port l'Hebert. PAR data from sensors deployed in the water column (top panel) were used to calculate the light attenuation coefficient (bottom panel).

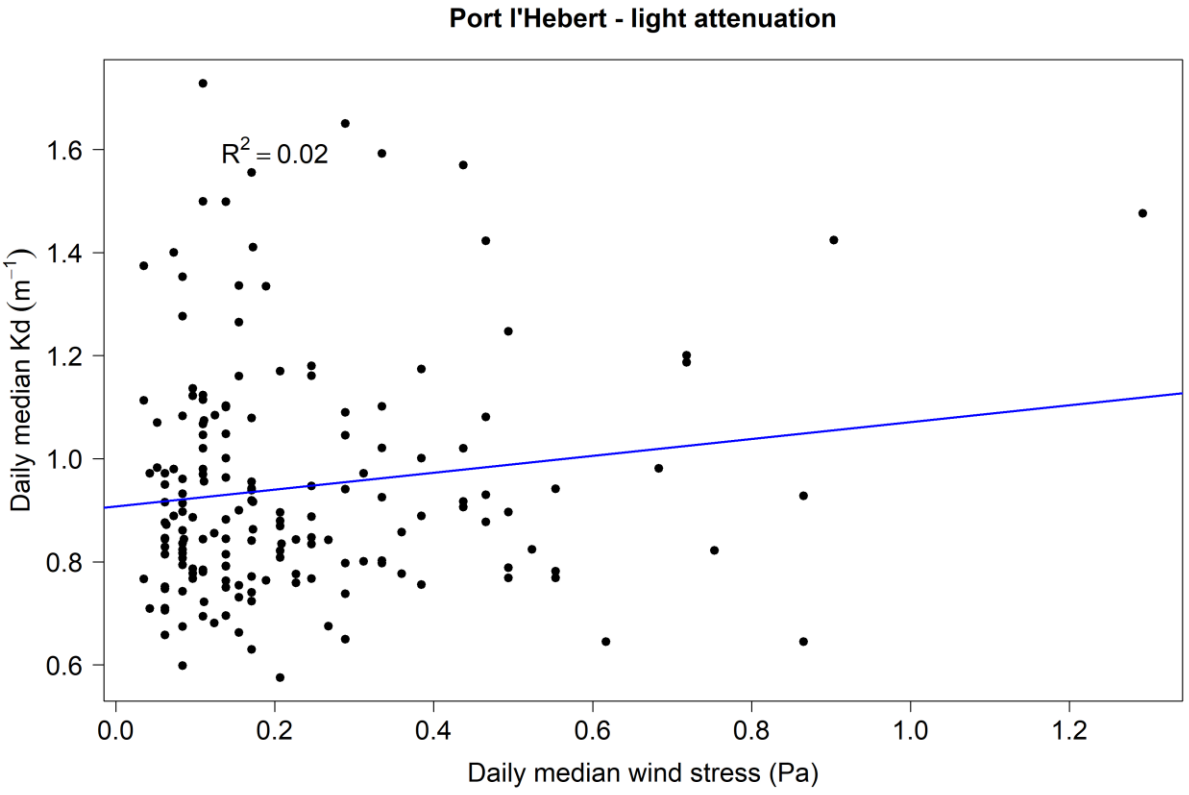

Figure 13b. Relationship between the daily median light attenuation coefficient (Kd) and daily median wind stress (Pa x 10^1).

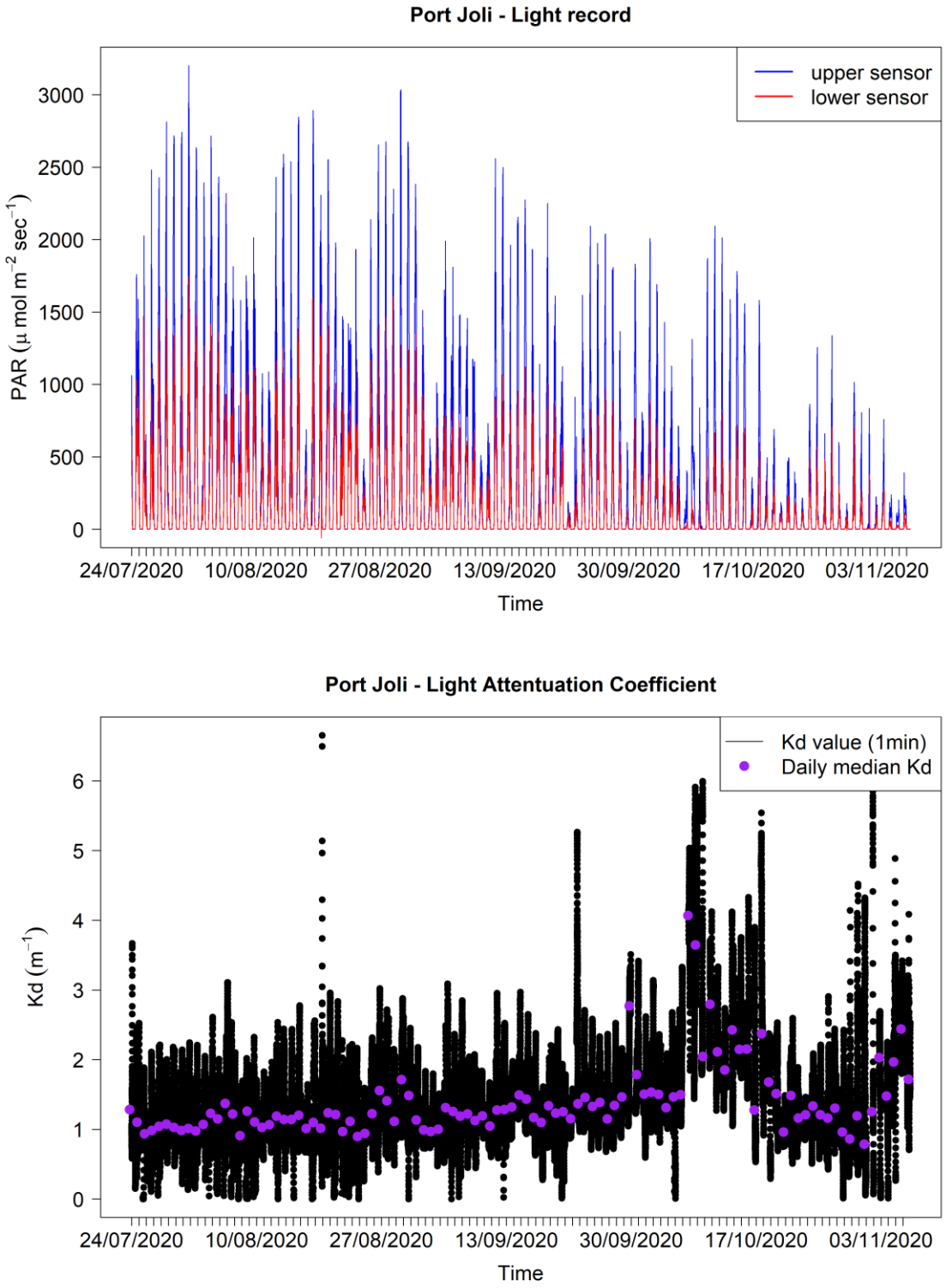

Figure 14a. Light conditions at Port Joli. PAR data from sensors deployed in the water column (top panel) were used to calculate the light attenuation coefficient (bottom panel).

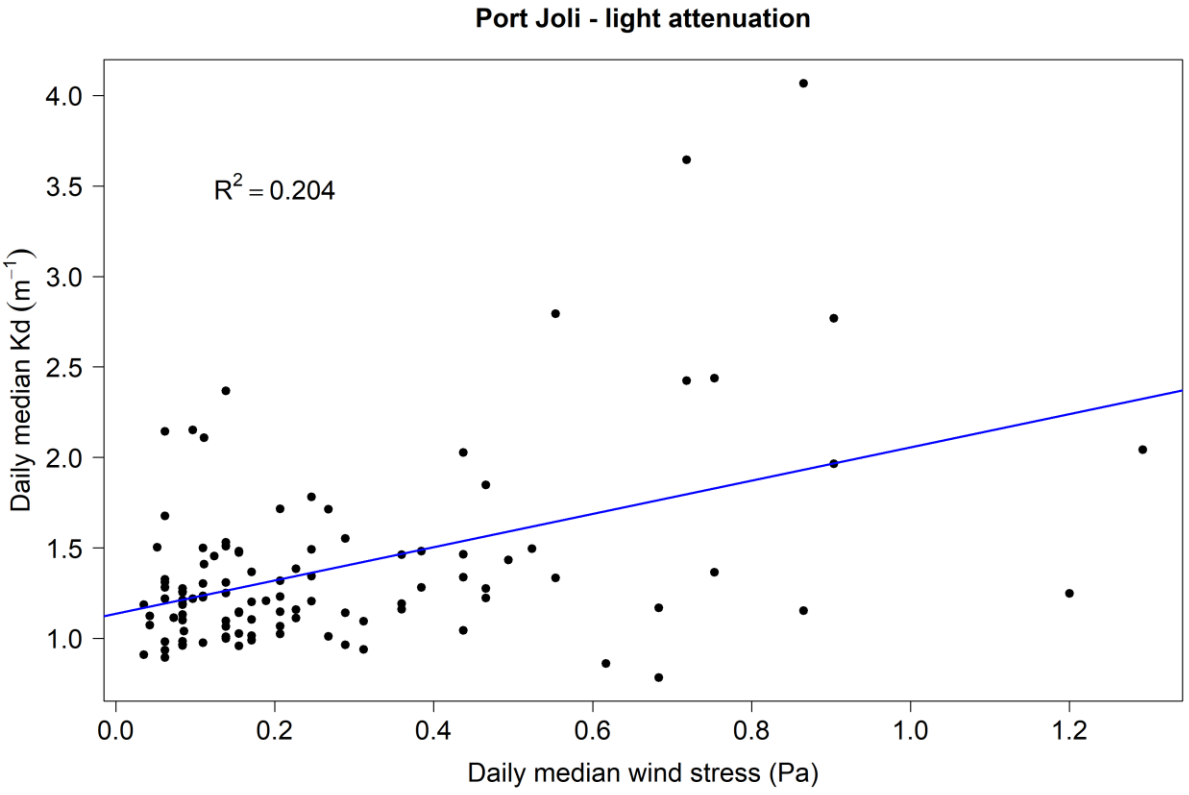

Figure 14b. Relationship between the daily median light attenuation coefficient (Kd) and daily median wind stress (Pa x 10^1).

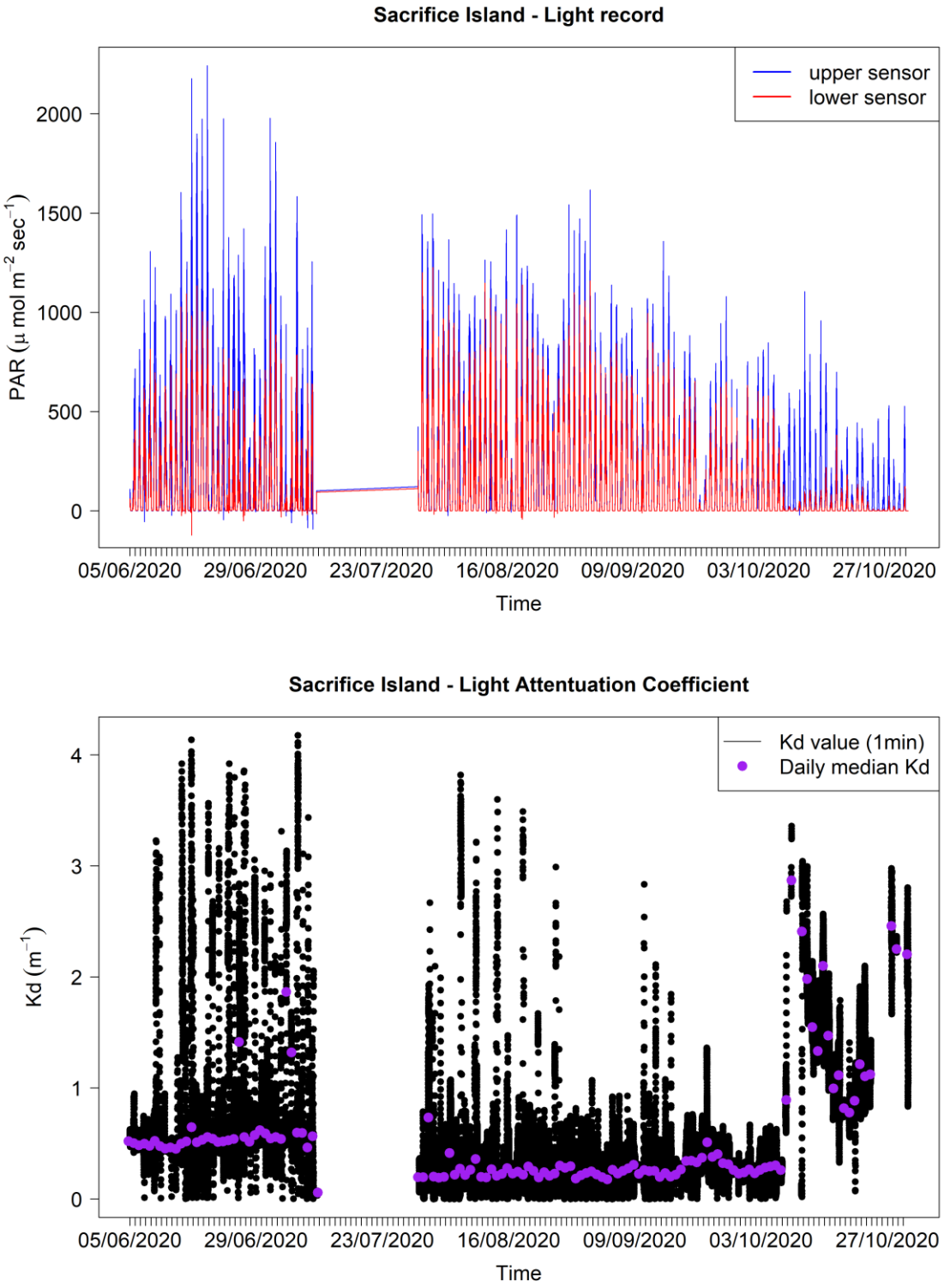

Figure 15a. Light conditions at Sacrifice Island. PAR data from sensors deployed in the water column (top panel) were used to calculate the light attenuation coefficient (bottom panel). The straight line in the top panel indicates a data gap.

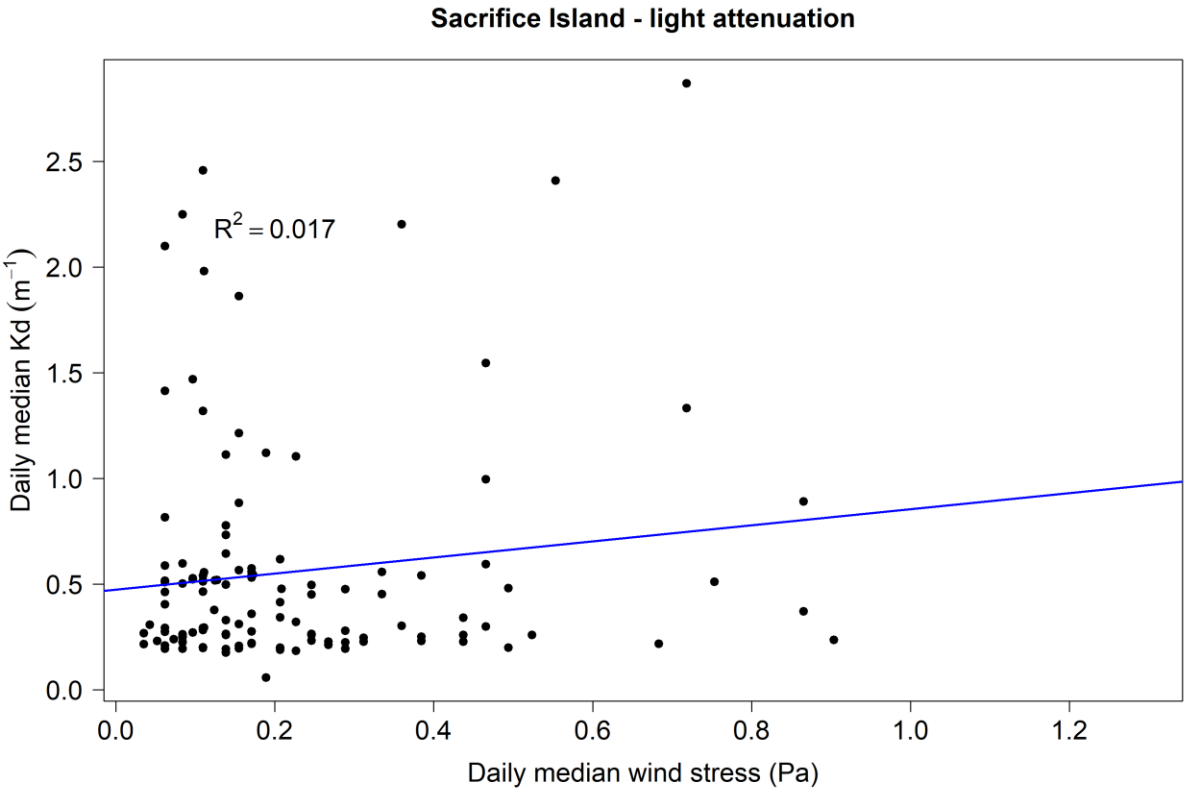

Figure 15b. Relationship between the daily median light attenuation coefficient (Kd) and daily median wind stress(Pa x 10^1).

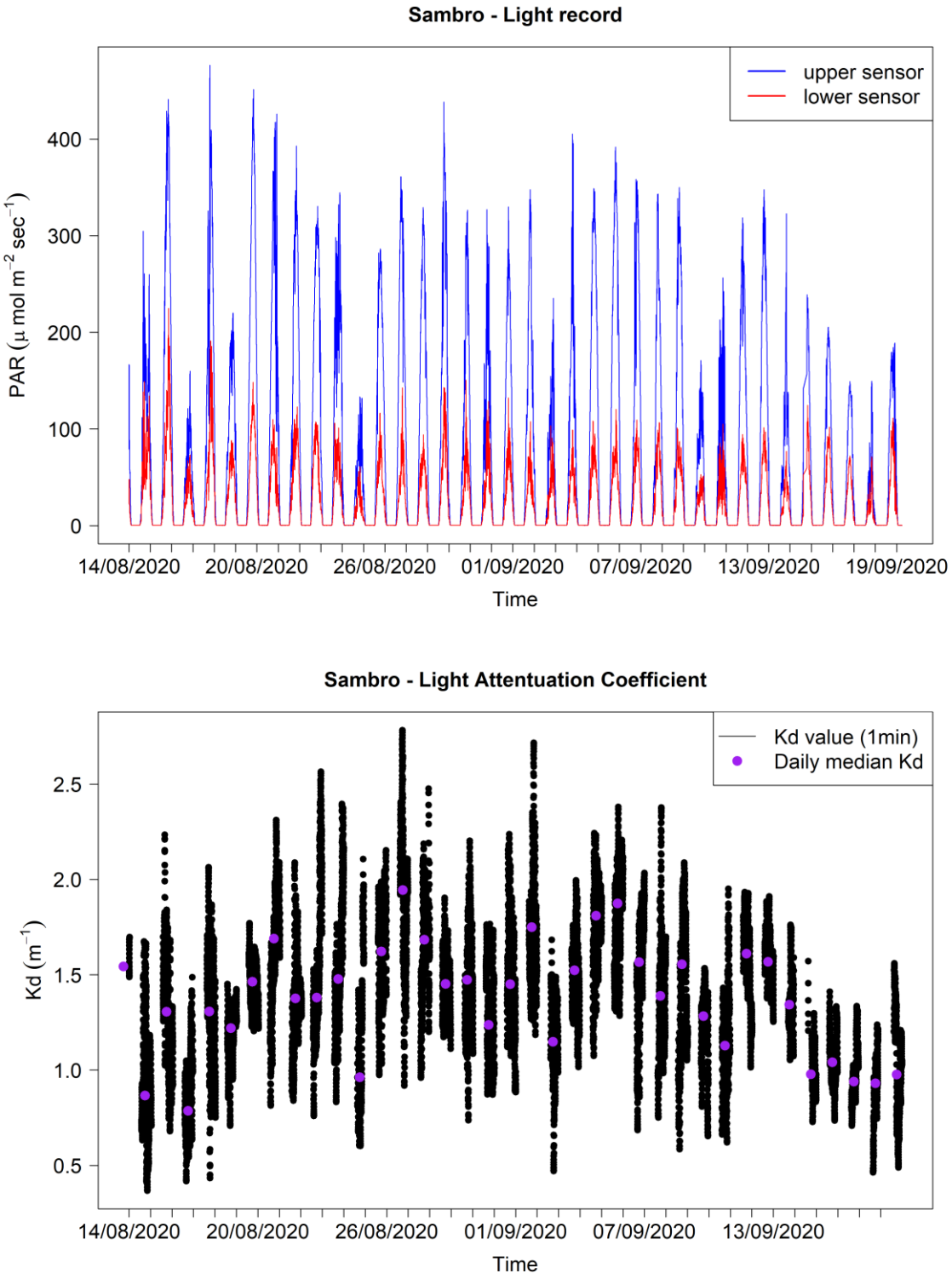

Figure 16a. Light conditions at Sambro. PAR data from sensors deployed in the water column (top panel) were used to calculate the light attenuation coefficient (bottom panel).

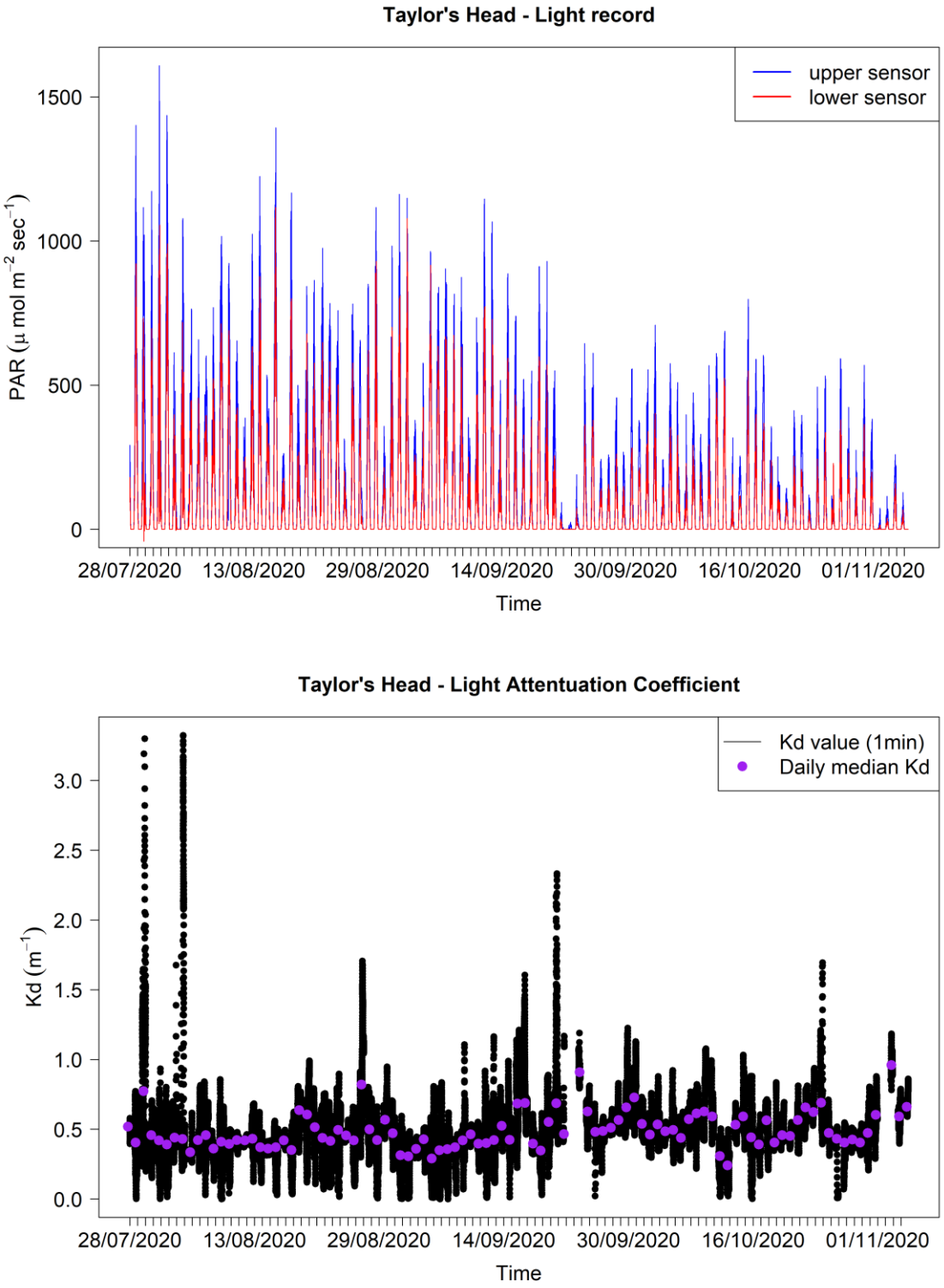

Figure 17a. Light conditions at Taylor's Head. PAR data from sensors deployed in the water column (top panel) were used to calculate the light attenuation coefficient (bottom panel).

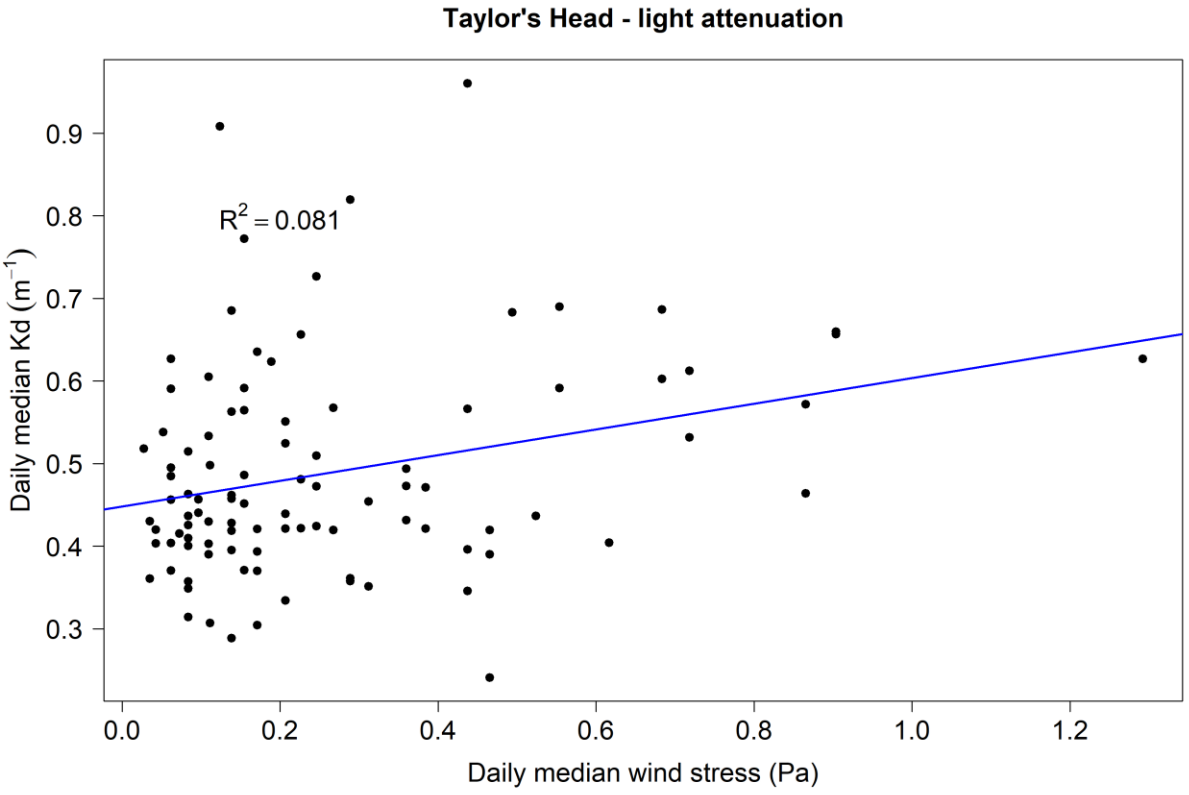

Figure 17b. Relationship between the daily median light attenuation coefficient (Kd) and daily median wind stress (Pa x 10^1).

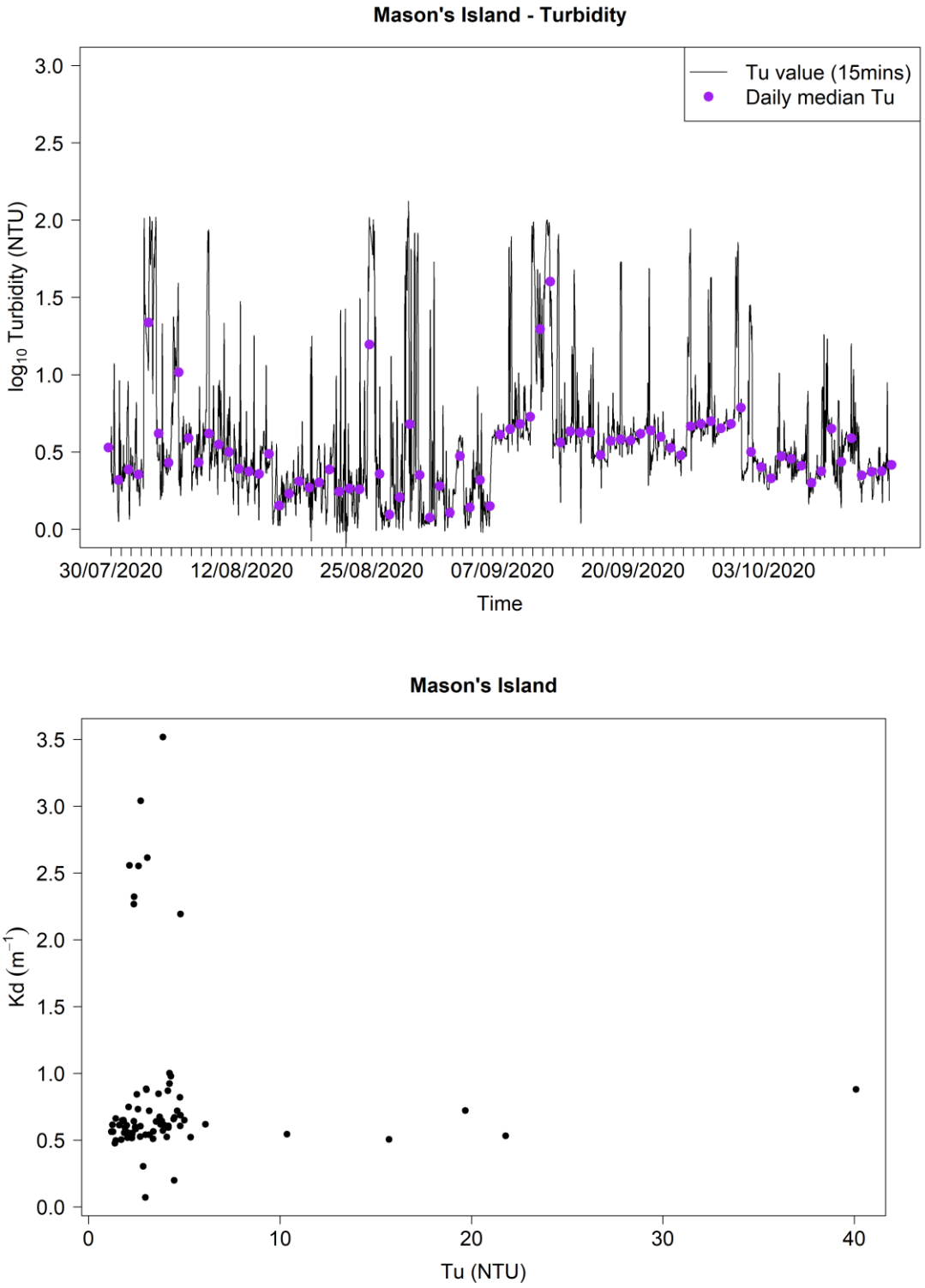

Figure 18. Turbidity (Tu) records (top panel) and daily median light attenuation vs. daily median turbidity at Mason's Island (bottom panel).

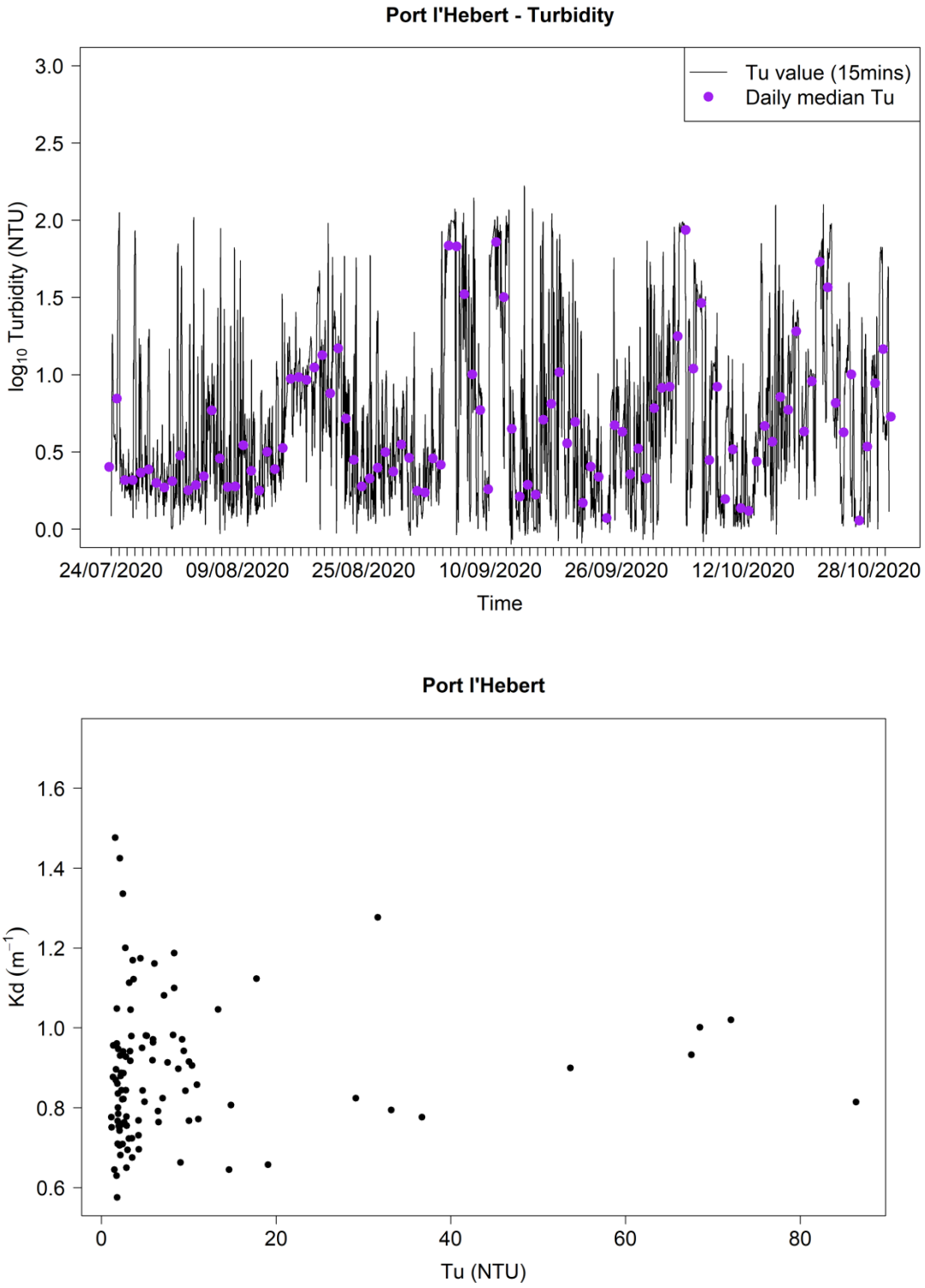

Figure 19. Turbidity (Tu) records (top panel) and daily median light attenuation vs. daily median turbidity at Port l'Hebert (bottom panel).

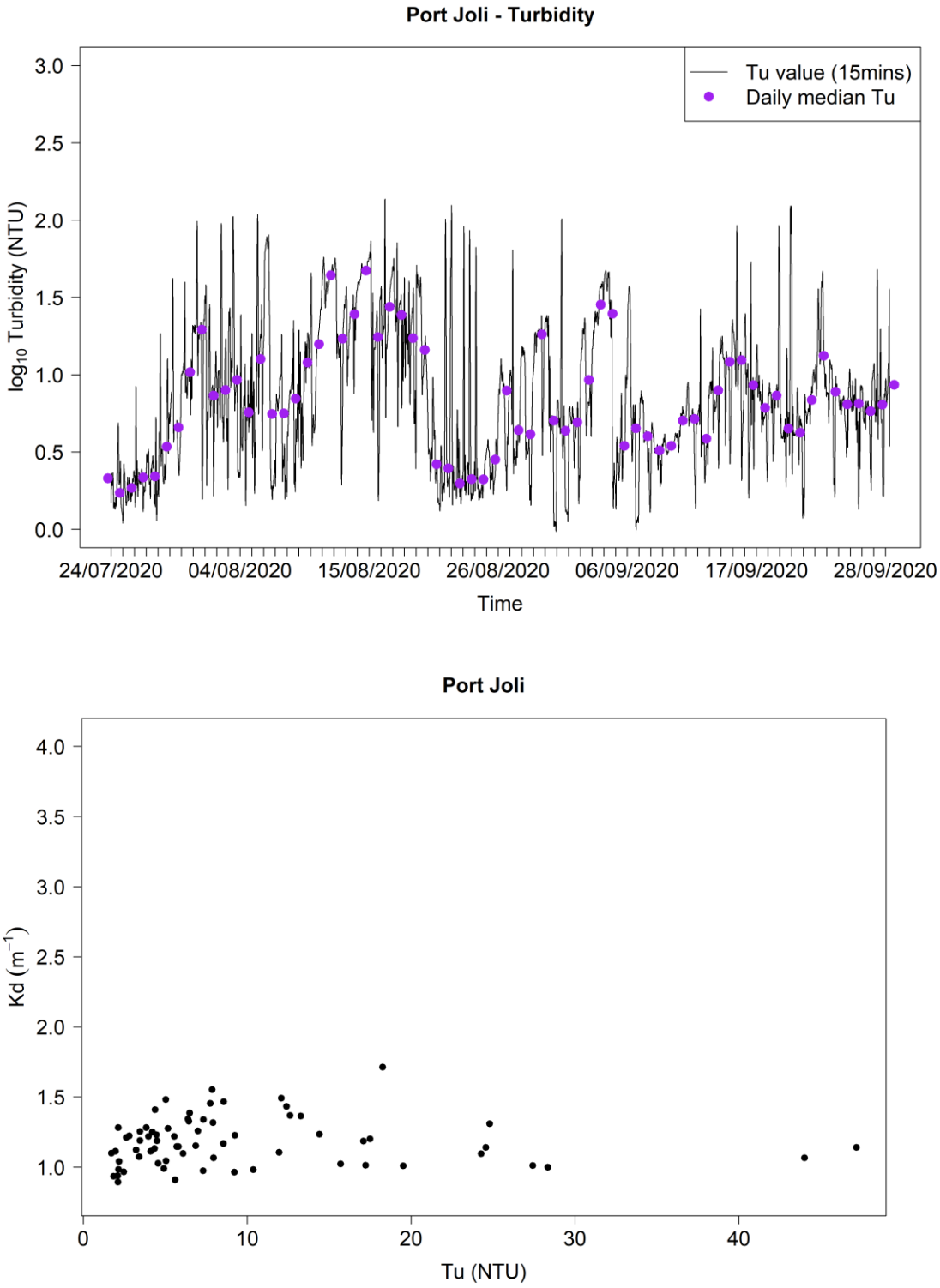

Figure 20. Turbidity (Tu) records (top panel) and daily median light attenuation vs. daily median turbidity at Port Joli (bottom panel).

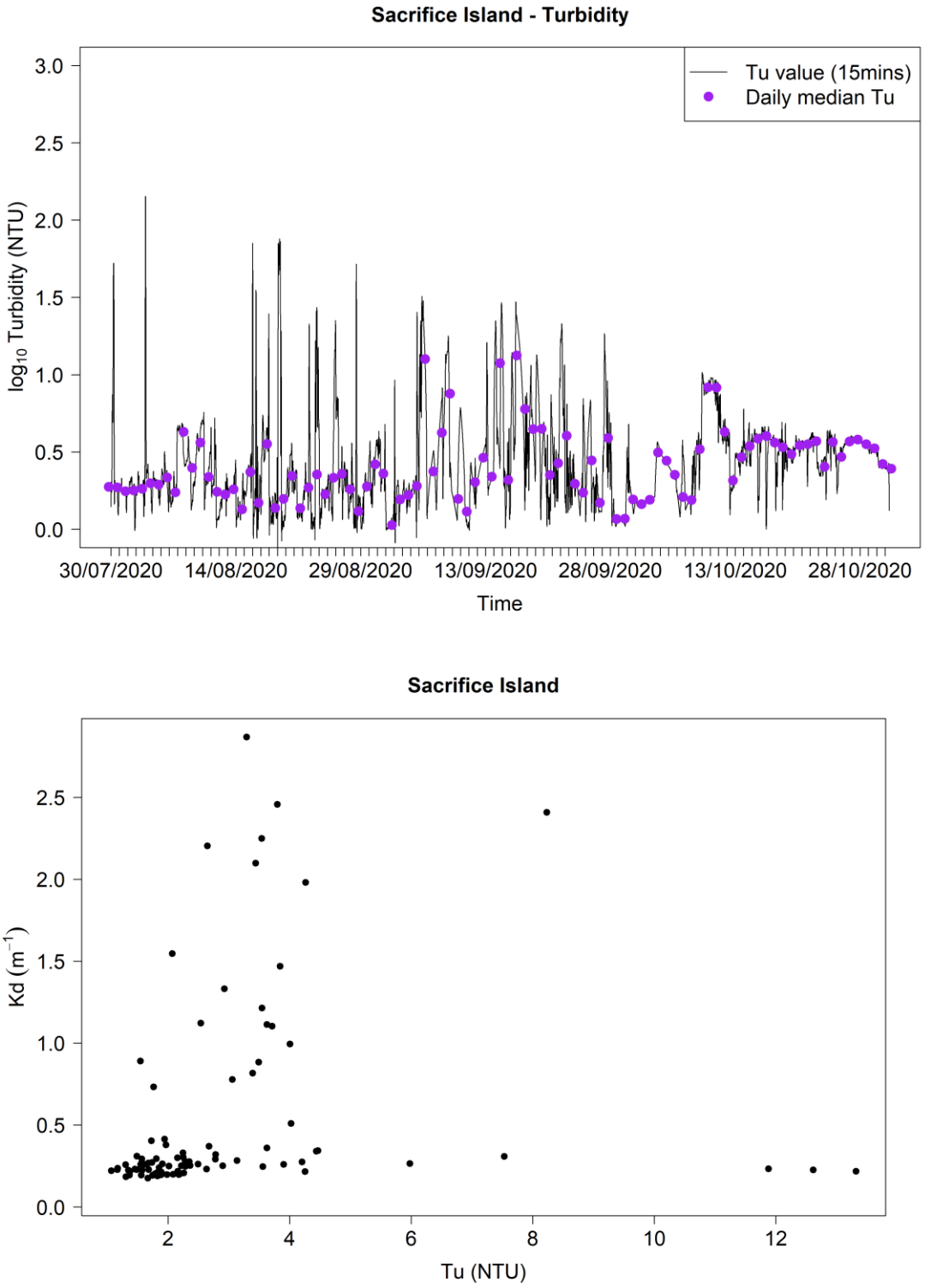

Figure 21. Turbidity (Tu) records (top panel) and daily median light attenuation vs. daily median turbidity at Sacrifice Island (bottom panel).

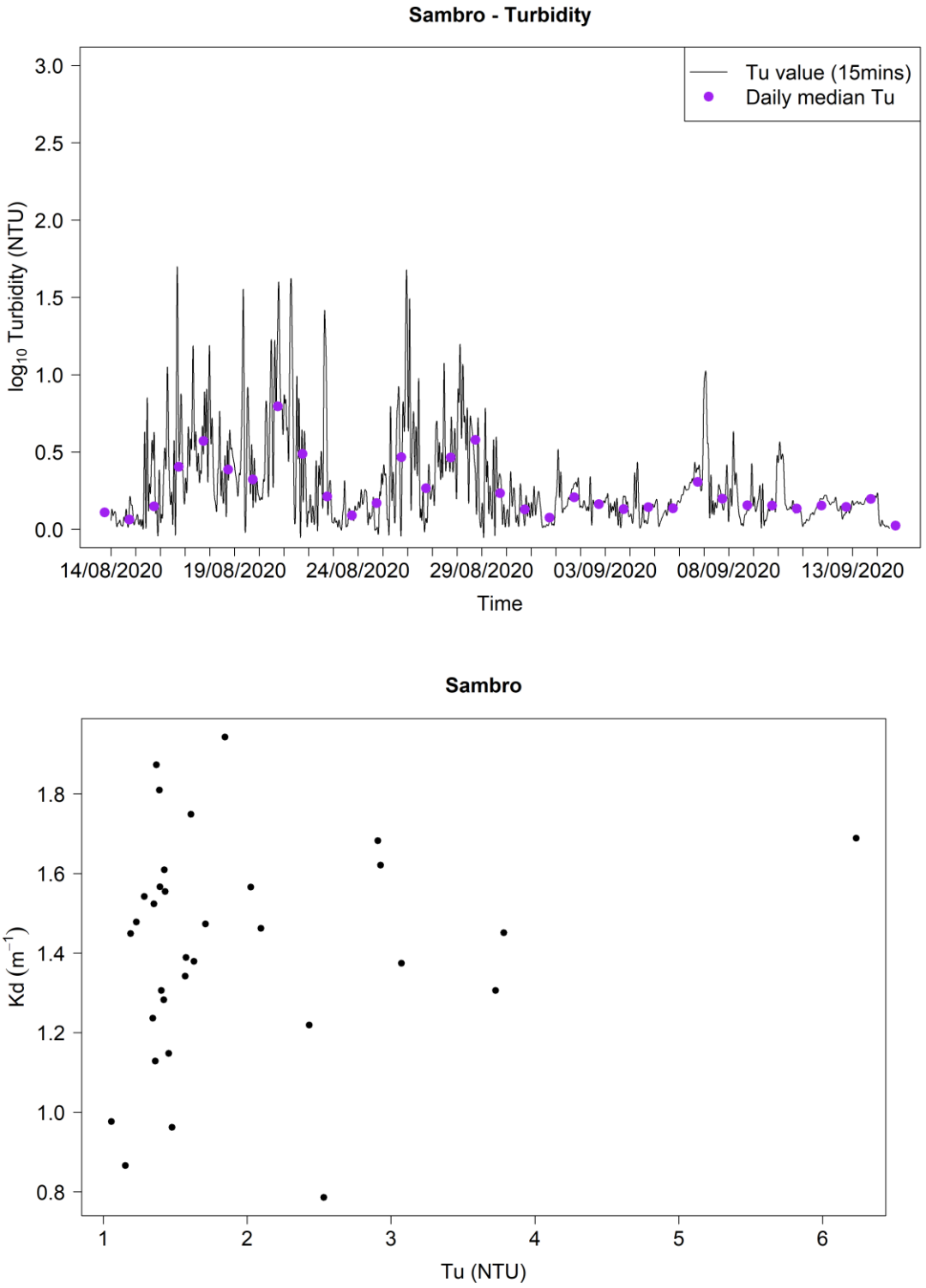

Figure 22. Turbidity (Tu) records (top panel) and daily median light attenuation vs. daily median turbidity at Sambro (bottom panel).

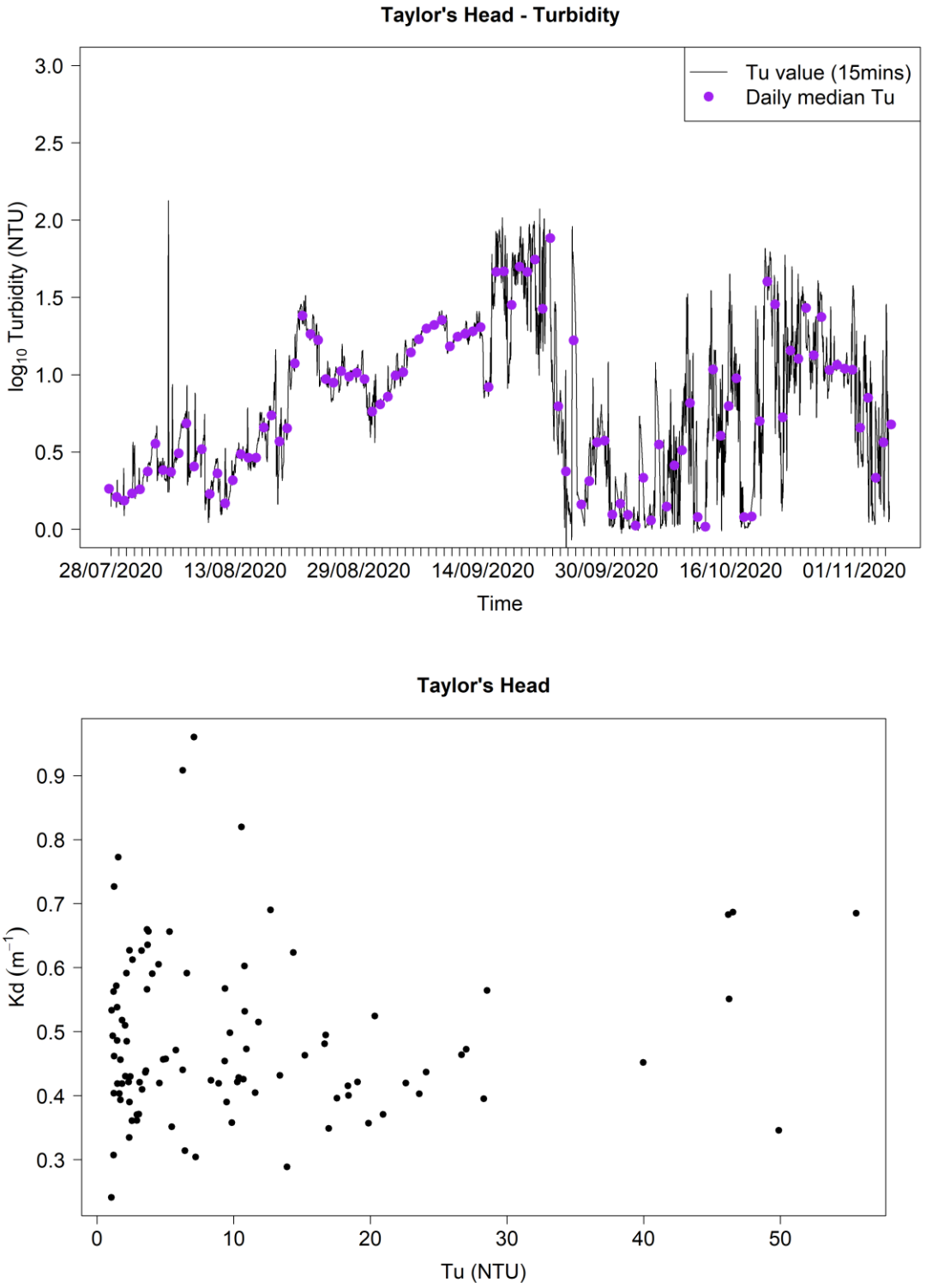

Figure 23. Turbidity (Tu) records (top panel) and daily median light attenuation vs. daily median turbidity at Taylor's Head (bottom panel).

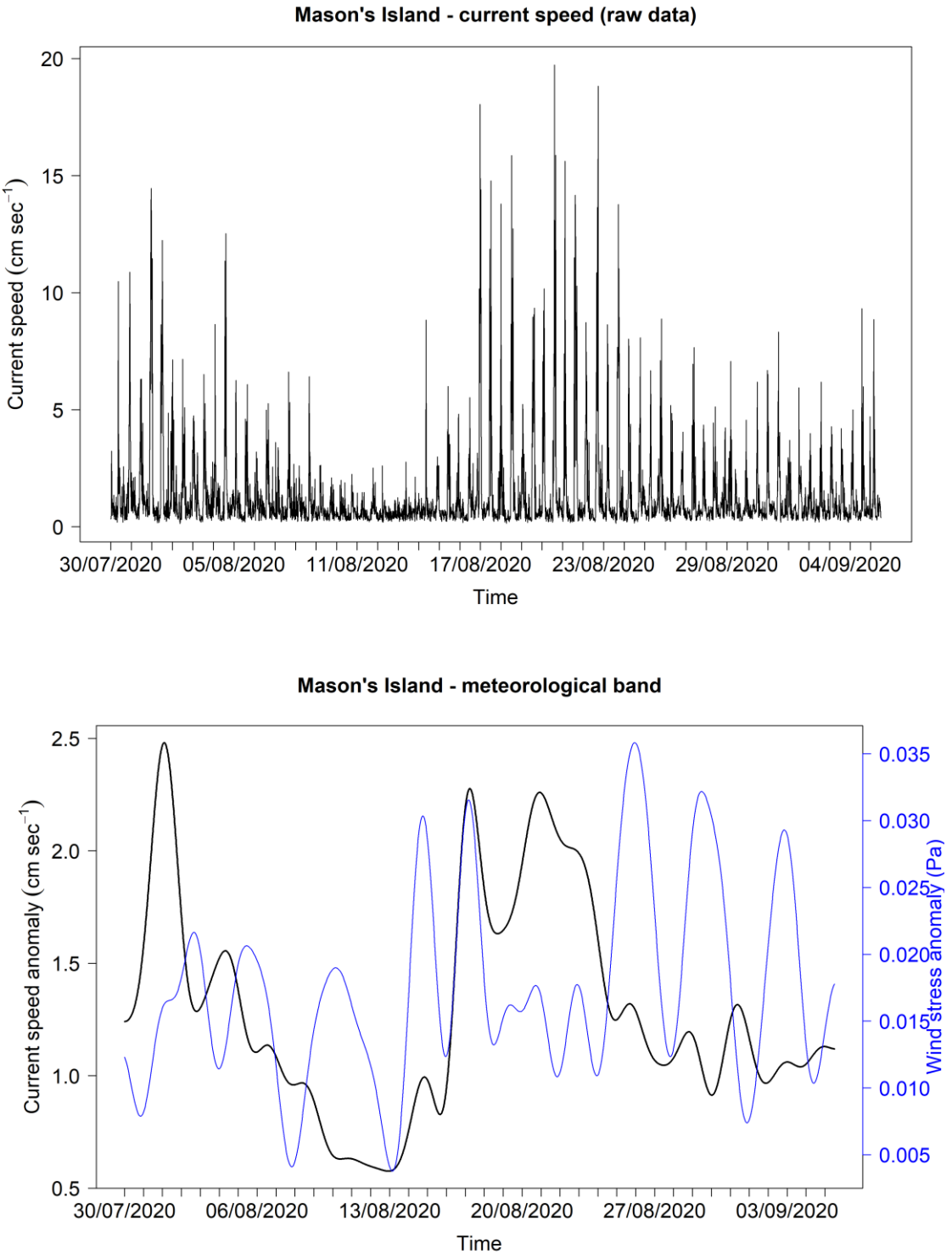

Figure 24a. Current speed (top panel) and the meteorological band overlaid with the same band of wind stress (bottom panel) at Mason's Island.

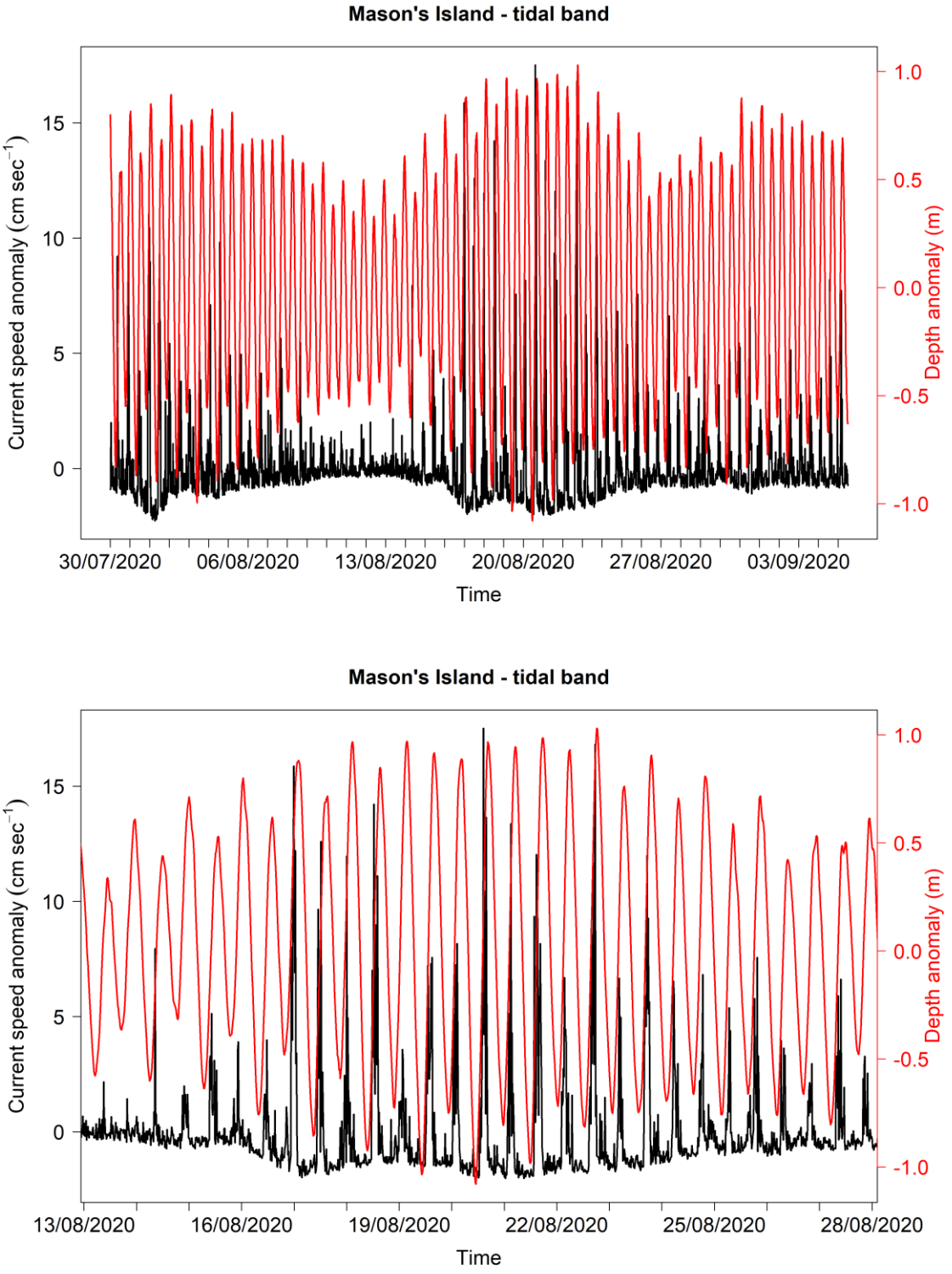

Figure 24b. Tidal band of the full current record overlaid with the depth anomaly (top panel), and an isolated period (bottom panel) at Mason's Island.

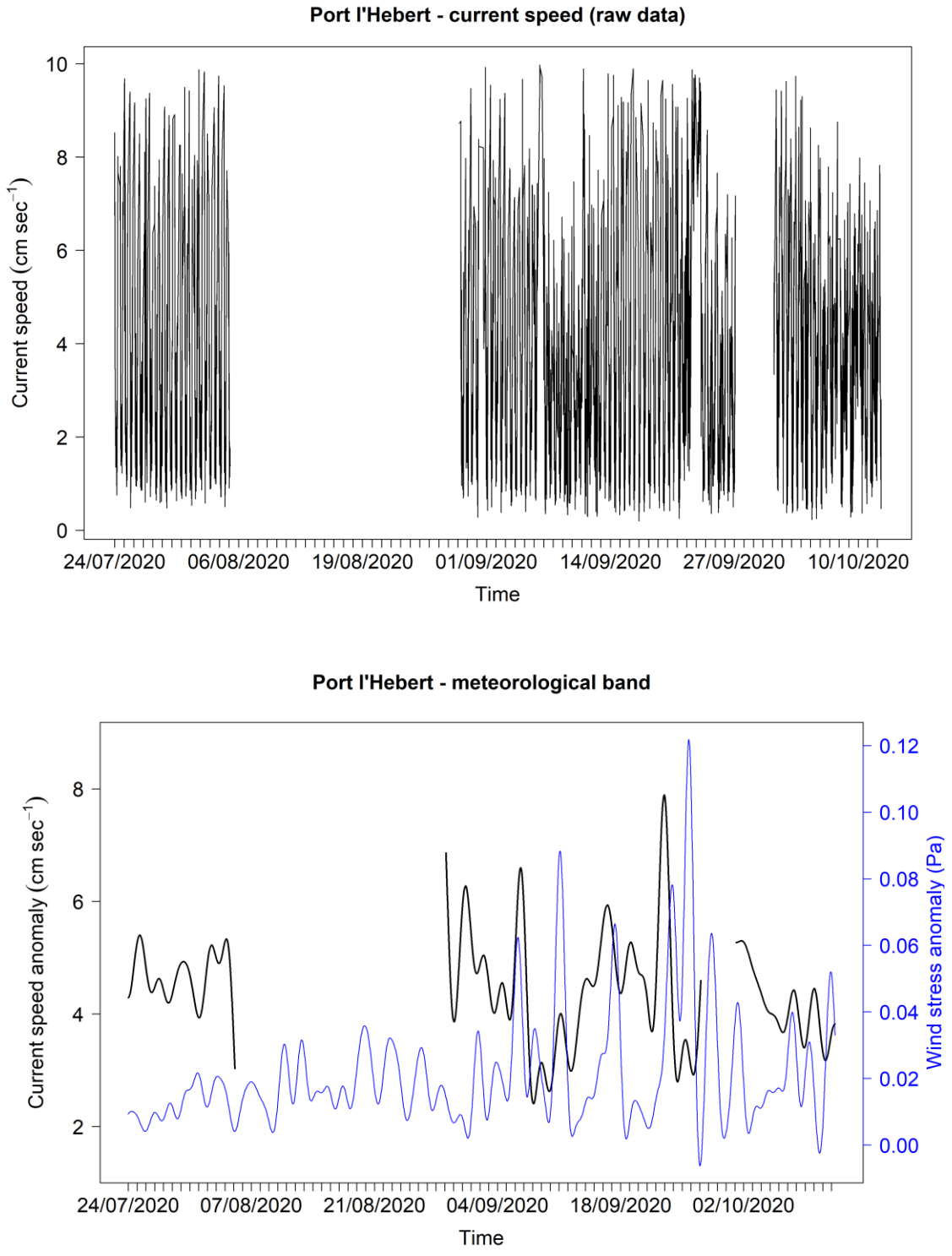

Figure 25a. Current speed (top panel) and the meteorological band overlaid with the same band of wind stress (bottom panel) at Port l/Hebert.

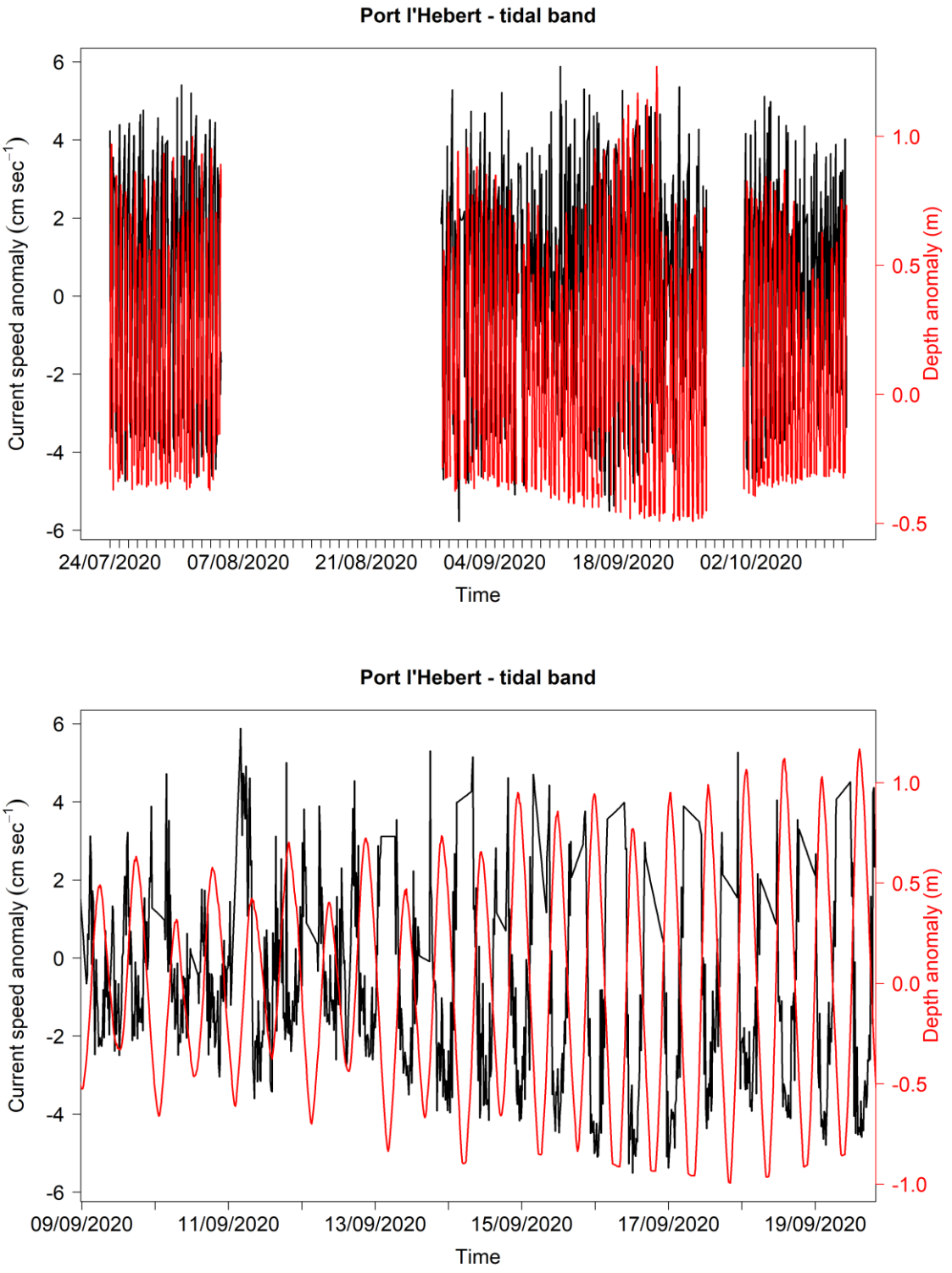

Figure 25b. Tidal band of the full current record overlaid with the depth anomaly (top panel), and an isolated period (bottom panel) at Port l'Hebert.

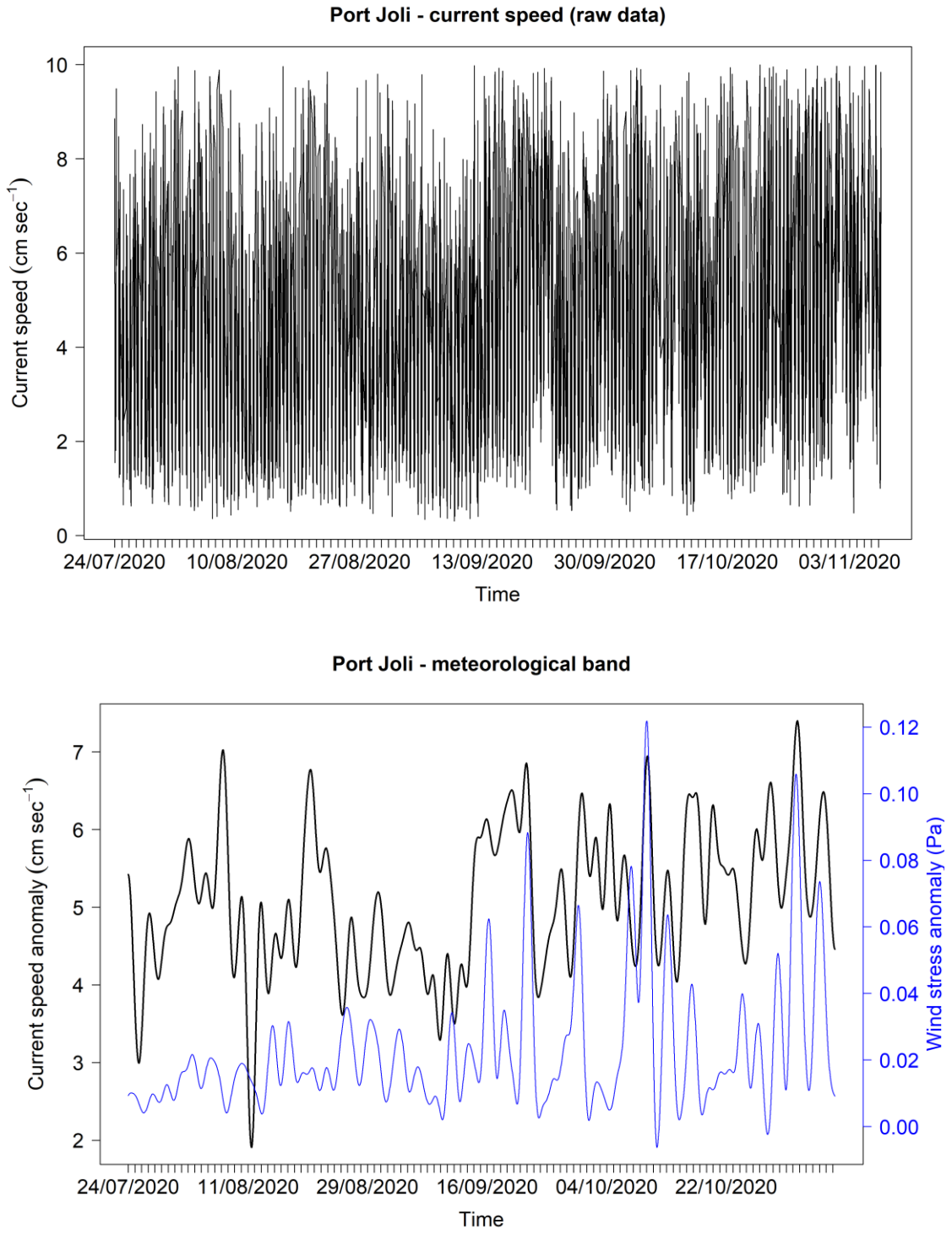

Figure 26a. Current speed (top panel) and the meteorological band overlaid with the same band of wind stress (bottom panel) at Port Joli.

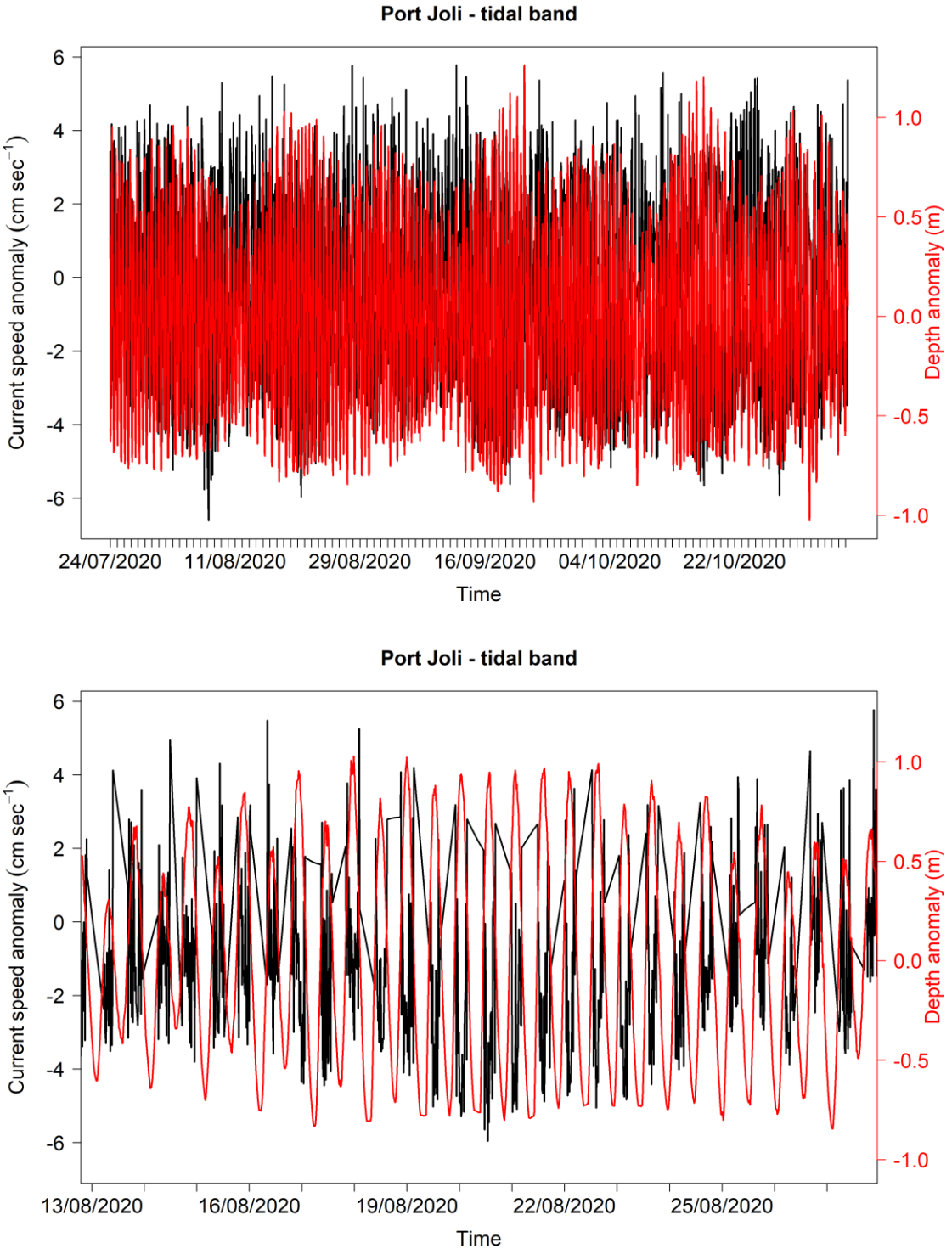

Figure 26b. Tidal band of the full current record overlaid with the depth anomaly (top panel), and an isolated period (bottom panel) at Port Joli.

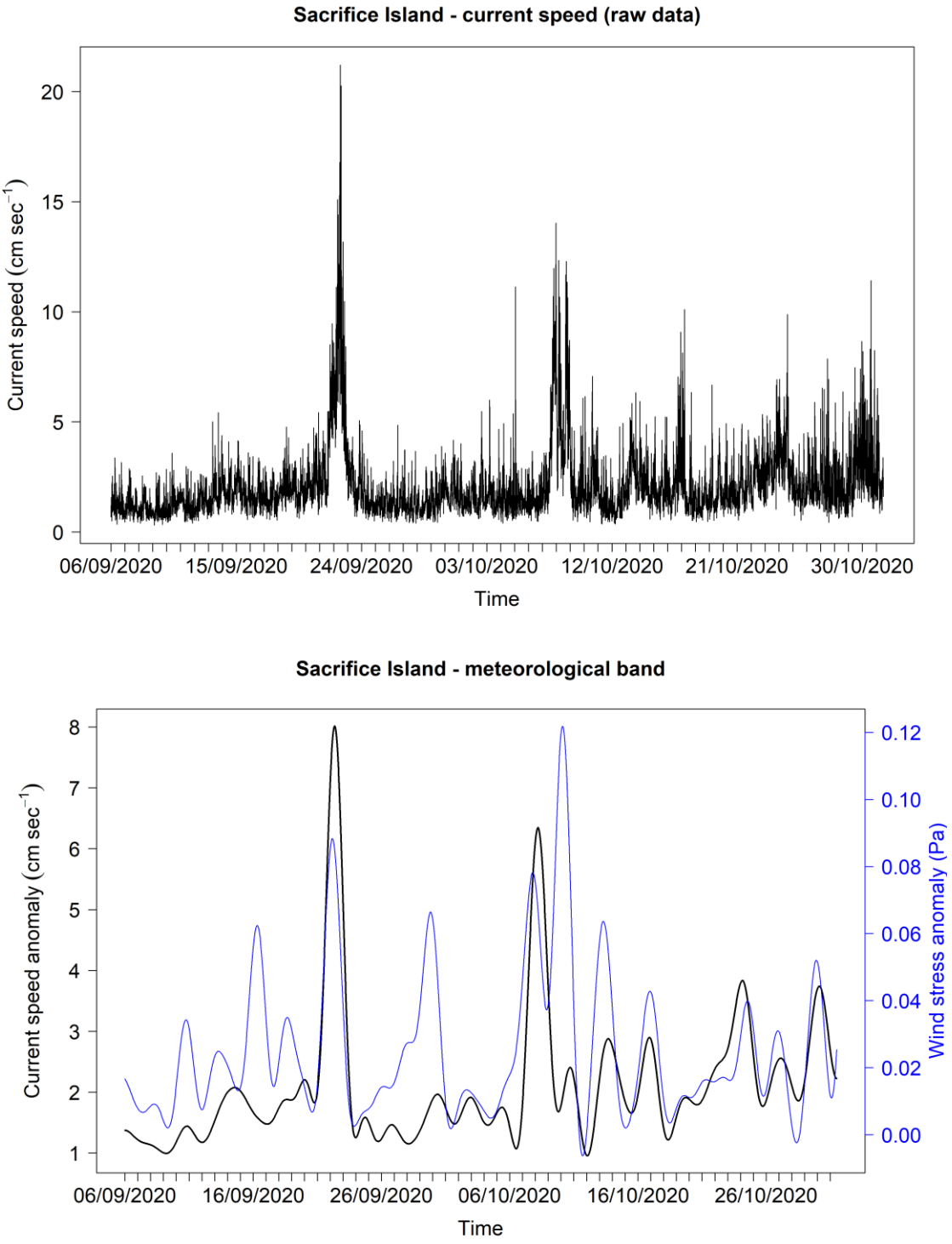

Figure 27a. Current speed (top panel) and the meteorological band overlaid with the same band of wind stress (bottom panel) at Sacrifice Island.

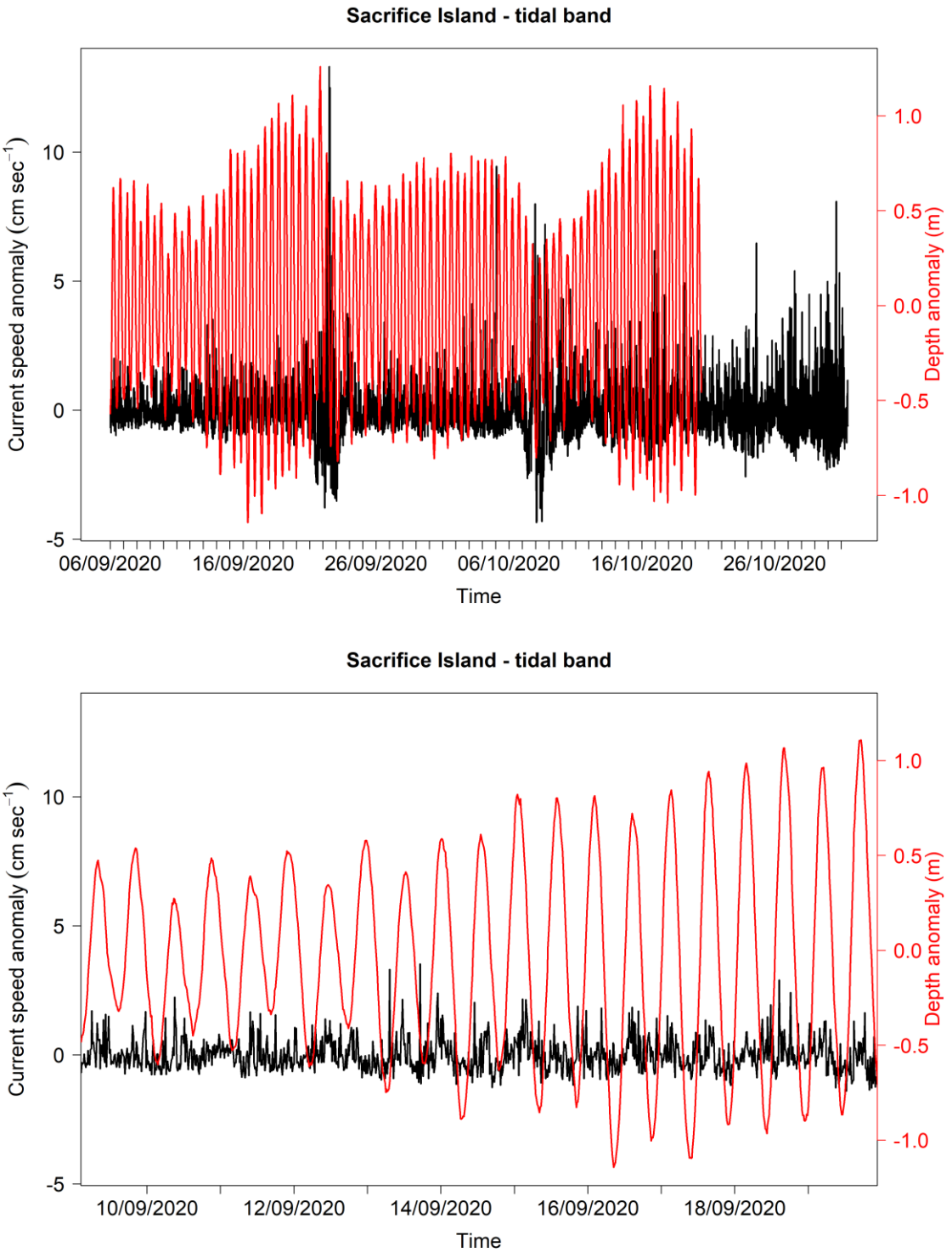

Figure 27b. Tidal band of the full current record overlaid with the depth anomaly (top panel), and an isolated period (bottom panel) at Sacrifice Island.

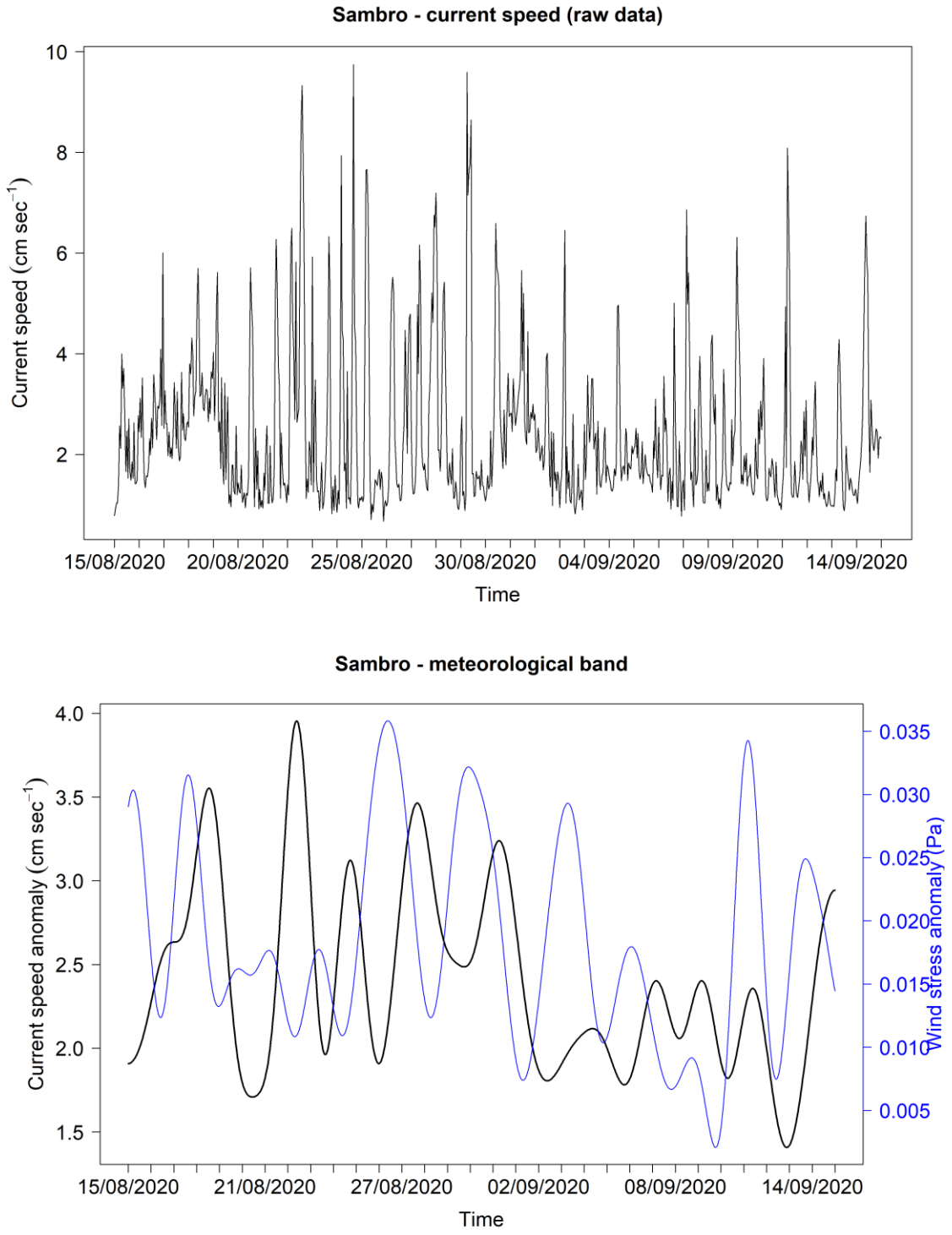

Figure 28a. Current speed (top panel) and the meteorological band overlaid with the same band of wind stress (bottom panel) at Sambro.

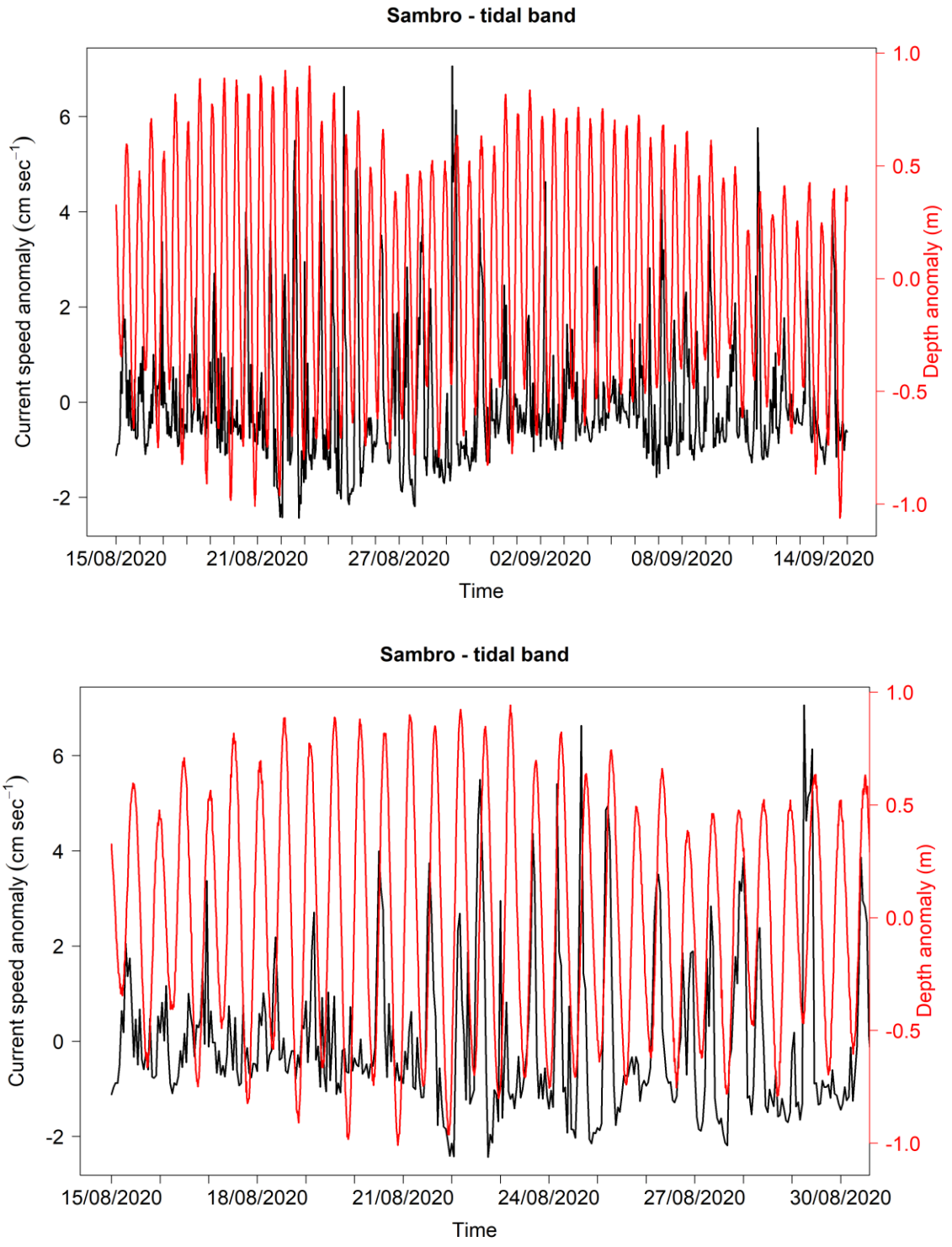

Figure 28b. Tidal band of the full current record overlaid with the depth anomaly (top panel), and an isolated period (bottom panel) at Sambro.

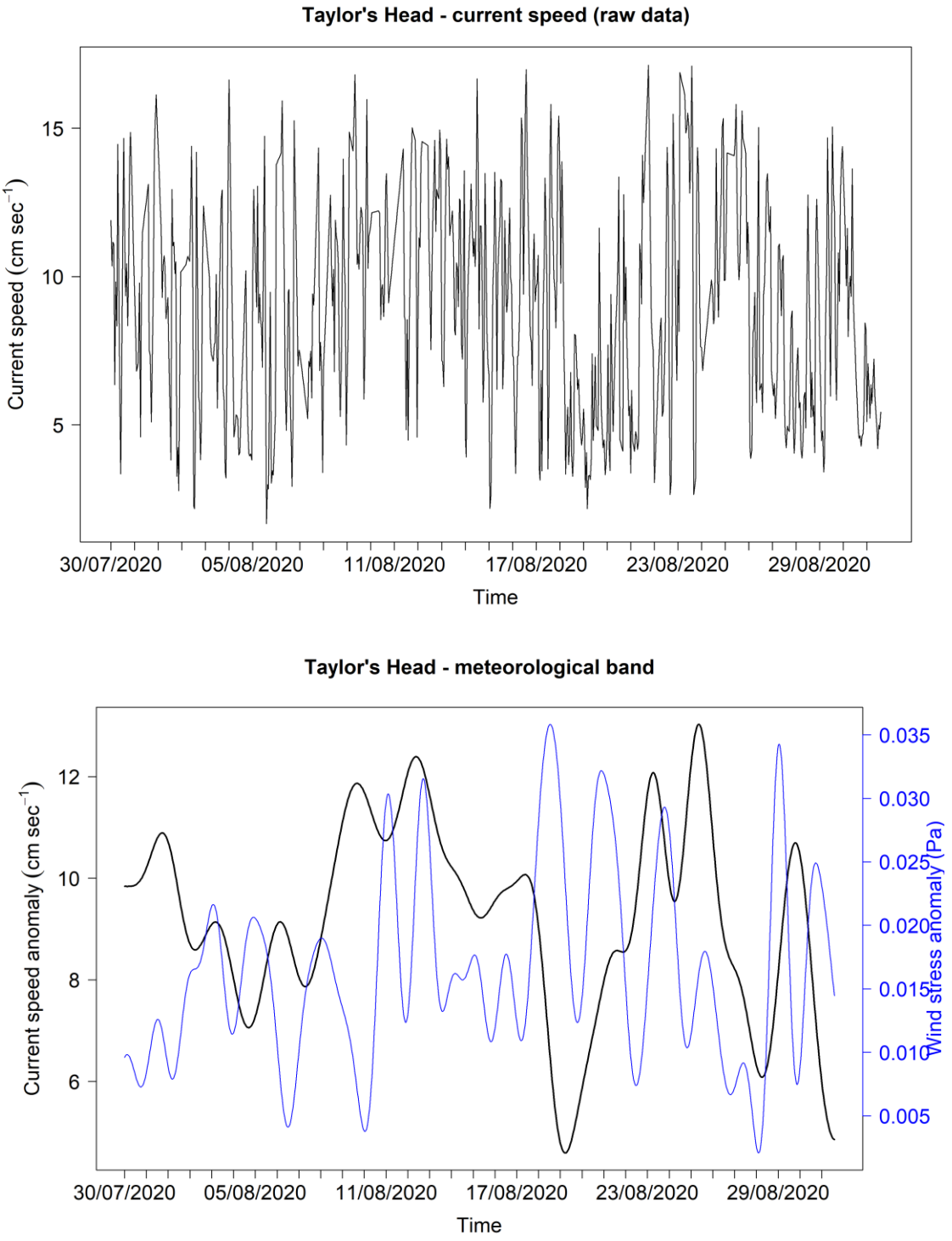

Figure 29a. Current speed (top panel) and the meteorological band overlaid with the same band of wind stress (bottom panel) at Taylor's Head.

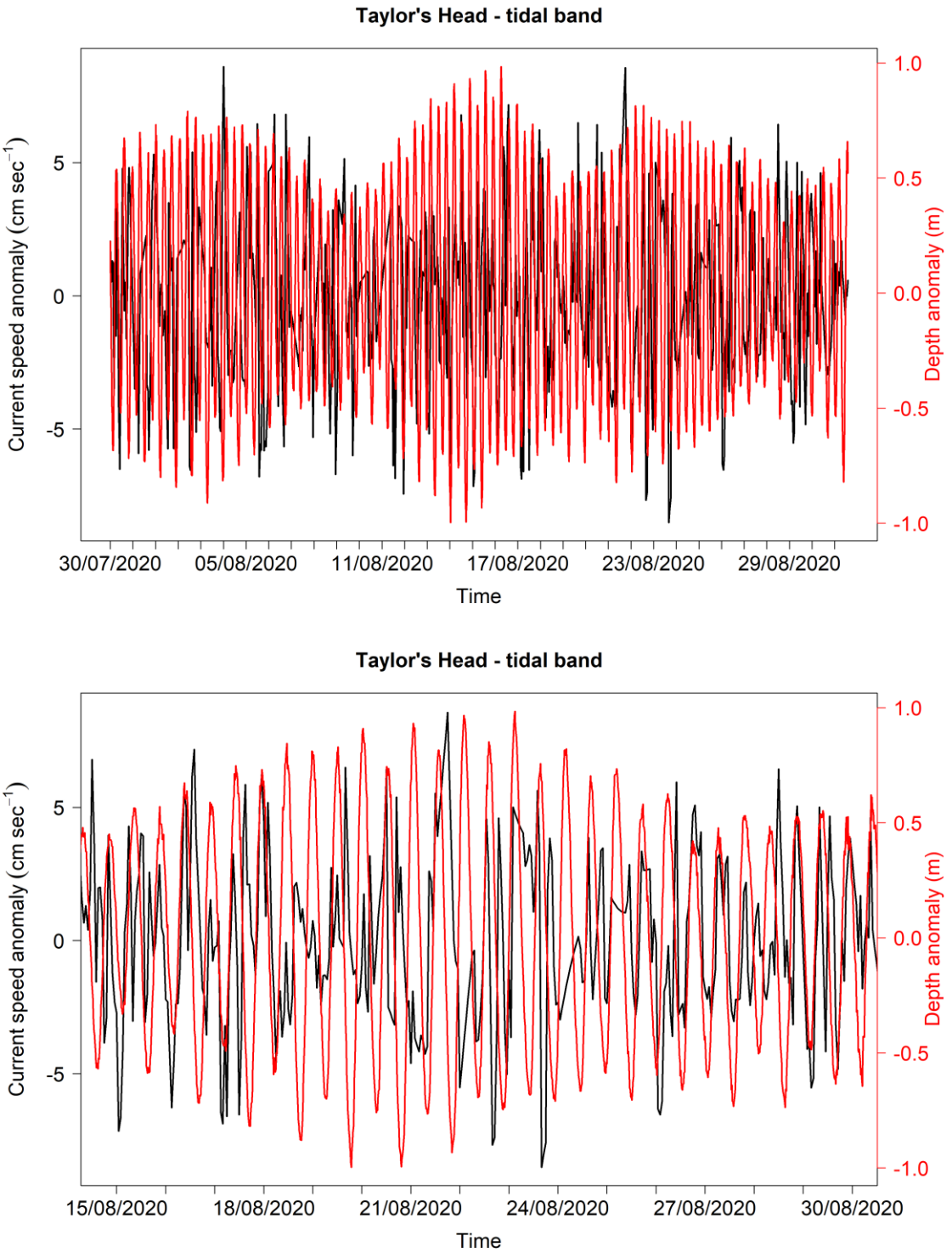

Figure 29b. Tidal band of the full current record overlaid with the depth anomaly (top panel), and an isolated period (bottom panel) at Taylor's Head.

SUPPLEMENT

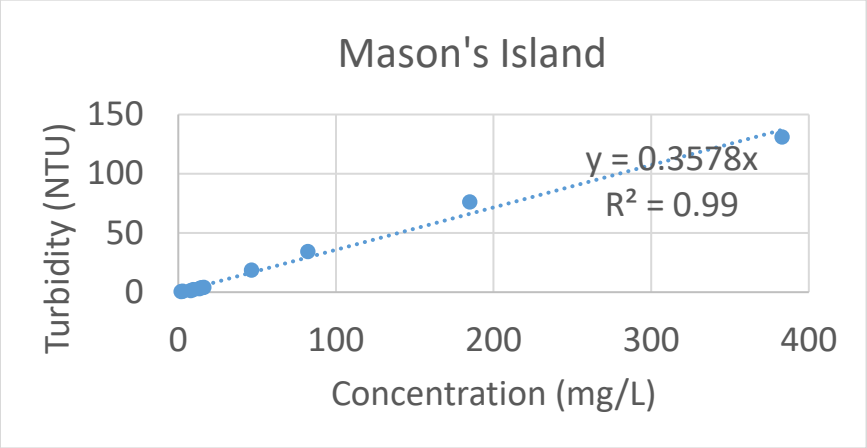
Mason's Island
Turbidity (NTU)
150
100
50
0
0
100
200
300
400
Concentration (mg/L)
y = 0.3578x
R² = 0.99

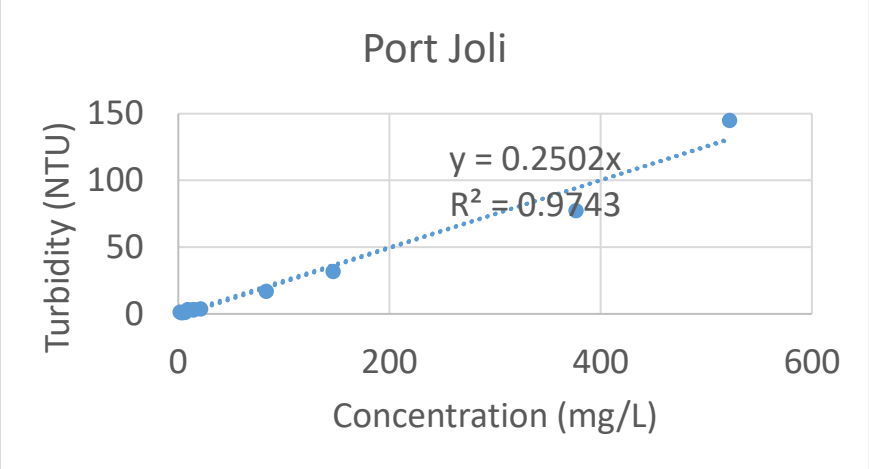
Port Joli
Turbidity (NTU)
150
100
50
0
0
200
400
600
Concentration (mg/L)
y = 0.2502x
R² = 0.9743

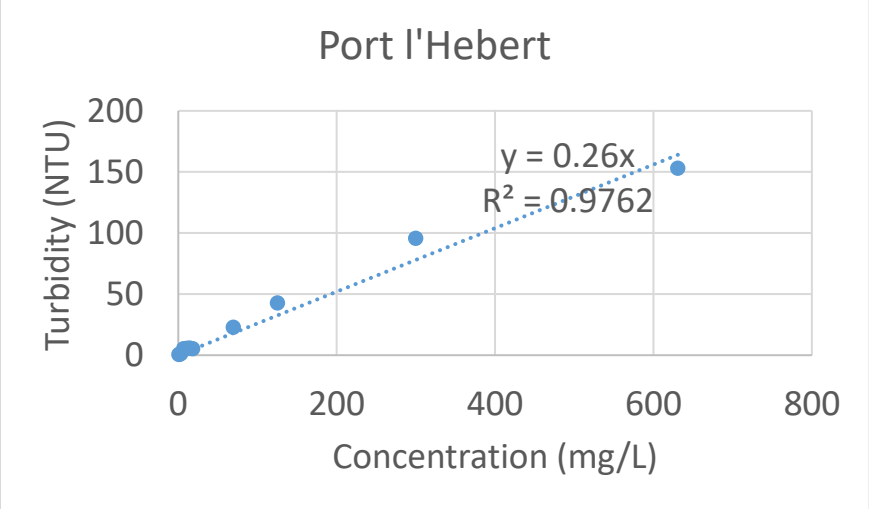
Port l'Hebert
Turbidity (NTU)
200
150
100
50
0
0
200
400
600
800
Concentration (mg/L)
y = 0.26x
R² = 0.9762

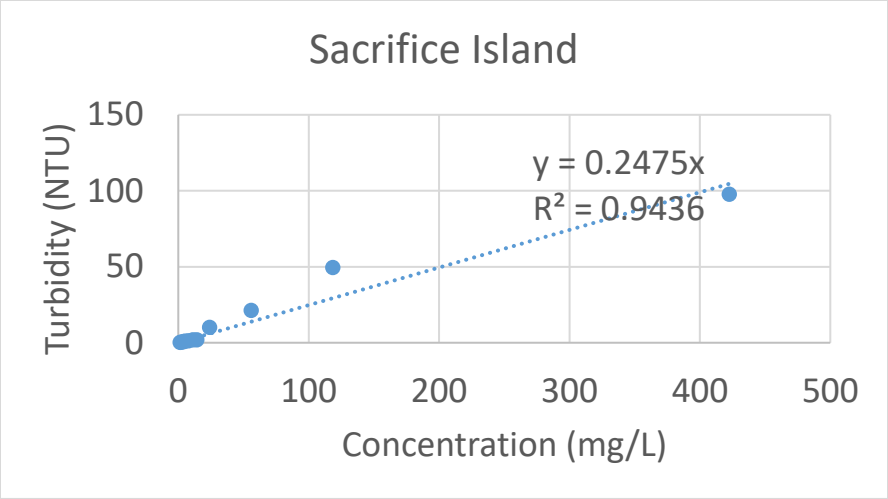

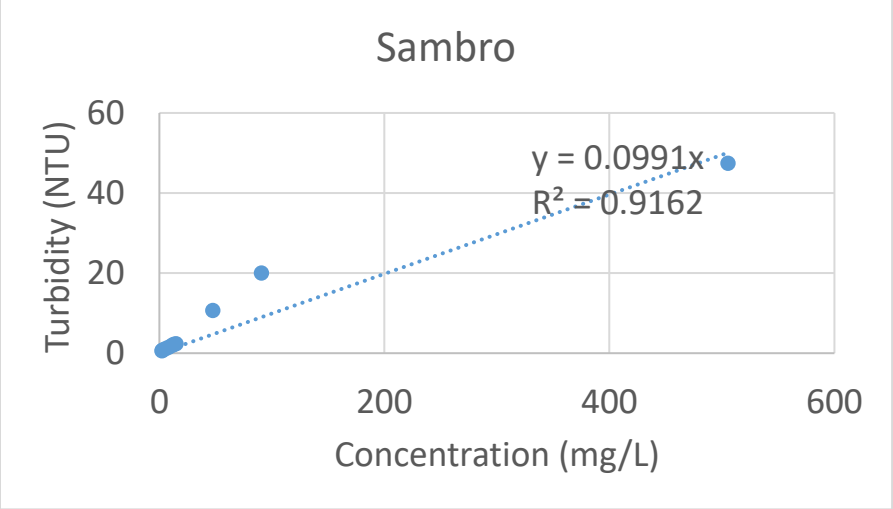

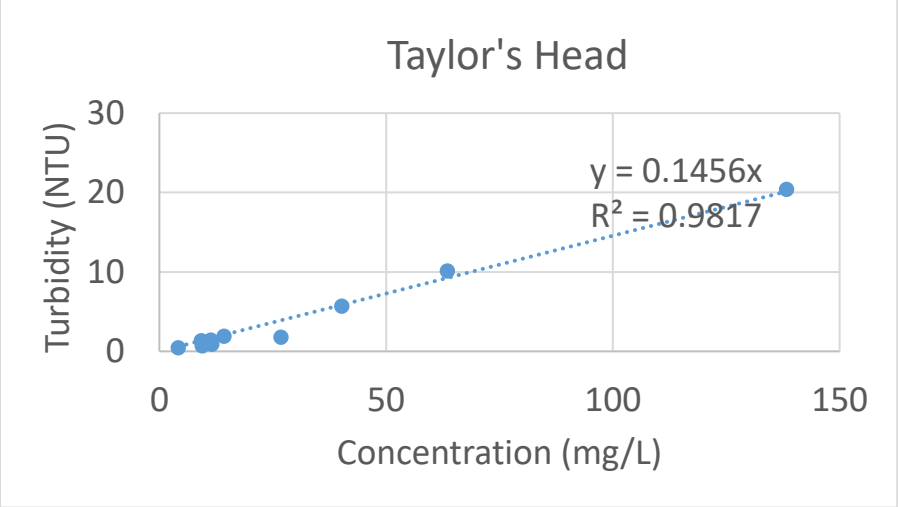

Figure S1. Relationships between turbidity (NTU) and particle concentration (mg L^{-1}) in the water column, determined from laboratory calibrations.